Abstract

VASQUEZ, DIEGO. Plate-End Debonding of Longitudinal Near-Surface Mounted Fiber Reinforced Polymer Strips on Reinforced Concrete Flexural Members. (Under the direction of Dr. Rudolf Seracino)

Adhesively bonding fiber reinforced polymers (FRP) to the faces of reinforced concrete elements has proven to be an effective strengthening technique. However it has some drawbacks that are overcome by the near-surface mounted (NSM) retrofitting technique, in which FRP is bonded into grooves cut in the concrete cover. Being a relatively recent technique, appropriate analytical models are not currently available to predict all possible forms of debonding.

In this research thesis, a comprehensive literature review showed the plate-end debonding mechanism to be the least understood of all three possible debonding mechanisms in NSM strengthened flexural elements, and hence a new rational plate-end debonding analytical model was proposed. The development of the model was aided by detailed finite element analyses and the reviewed literature.

Assessment of the proposed model against all available relevant experimental results showed that the model yields considerably more accurate results than the existing models applicable to NSM strengthening with FRP strips.

Plate-End Debonding of Longitudinal Near-Surface Mounted Fiber Reinforced Polymer Strips on Reinforced Concrete Flexural Members

by
Diego L. Vásquez Rayo

A thesis submitted to the graduate faculty of
North Carolina State University
in partial fulfillment of the
requirements for the degree of
Master of Science

Civil Engineering

Raleigh, NC

May 2008

APPROVED BY:

_____
Dr. Rudolf Seracino (Chair)

_____
Dr. Sami Rizkalla

_____
Dr. Tasnim Hassan

Biography

Diego Vasquez began his studies in Civil Engineering in August 1998 at the Universidad Javeriana in Cali, Colombia, and received his Bachelor's degree in May 2004, during which time he carried out research in durability of high performance concrete under chemical attack in sugar factories. Following his graduation he joined Mouchel Parkman Consulting in Yorkshire, UK, as graduate engineer, where he was involved in highway and structural assessment and repair projects for a period of two years. Encouraged by his experience in the structural field he decided to further his knowledge by joining the Structural Engineering and Mechanics Master of Science program at North Carolina State University in August 2006. During the course of his graduate studies he researched the behavior of concrete beams strengthened with fiber reinforced polymers.

Table of Contents

List of Tables

List of Figures

Notation

$(EA)_c$ = Axial rigidity of concrete section
$(EA)_{frp}$ = Axial rigidity of FRP plate or strip
$(EI)_{cmp}$ = Flexural rigidity of composite section
$(EI_{eff})_{cmp}$ = Flexural rigidity of composite section including effective moment of inertia
$(EI)_{frp}$ = Flexural rigidity of FRP plate or strip
$(EI)_{RC}$ = Flexural rigidity of reinforced concrete section
A_{frp} = Cross-section area of FRP plate or strip
A_r = Strip-end area resisting the axial force on an NSM FRP
A_s = Area of longitudinal steel reinforcement
b_c = Beam web breadth
b_f = Length of the IC debonding failure plane parallel to the concrete surface
b_{tfp} = Width of FRP plate
d_f = Length of the IC debonding failure plane perpendicular to the concrete surface
e = Distance from the point of CDC crack initiation to the resultant of loads applied over L_O
e = Base of the natural algorithm
E_c = Elastic modulus of concrete
E_{frp} = Modulus of elasticity of FRP plate or strip
f'_c = Concrete cylinder compressive strength
f_{ct} = Tensile strength of concrete
F_p = Axial force induced in the FRP plate due to bending
F_{ps} = Applied prestressing force
f_{tef} = Effective tensile strength of concrete
G_a = Shear modulus of epoxy adhesive
h = Beam depth
h_p = FRP plate depth
h_{pcmp} = Distance from the centroid of the composite section to the centroid of the FRP plate
h_s = FRP strip depth
$h_{s,cmp}$ = Distance from the centroid of the composite section to the centroid of the FRP strip
I_{cr} = Cracked moment of inertia of the transformed strengthened section
I_{eff} = Effective moment of inertia
I_g = Gross moment of inertia of the transformed strengthened section
J = Constant defined by the axial rigidity and geometric properties of a pull test joint
k = Fraction of the stirrup shear strength developed at CDC debonding

K_M,K_W	=	Ratios of the applied moment and load within L_O respectively, to the shear at the beam end
L_{crit}	=	Critical length to develop full IC debonding resistance
L_O	=	Distance from the point of CDC crack initiation to the nearest beam support
l_o	=	Distance from a beam support to the nearest plate end
L_{per}	=	IC debonding interface failure plane length
l_r	=	Axial shear stress resisting length
M_a	=	Applied moment
M_{cmp}	=	Moment on the composite section
M_c	=	Moment in concrete section calculated at the end of the FRP strip
M_{cr}	=	Cracking moment of concrete section
M_{cs}	=	Moment on the composite section calculated at the end of the FRP strip
M_p	=	Moment on the FRP plate
M_{RC}	=	Moment on the concrete section
M_s	=	Moment in FRP strip calculated at the end of the strip
P	=	Applied concentrated load
P_{IC}	=	IC debonding resistance
P_{plate}	=	Lesser of the IC debonding capacity of the plate and the ultimate tensile capacity of the FRP plate
t_a	=	Thickness of adhesive layer
t_b	=	Additional assumed breadth of IC debonding plane to either side of FRP
t_d	=	Additional assumed depth of IC debonding plane above FRP
t_p	=	FRP plate thickness
t_s	=	FRP strip thickness
t_{tfp}	=	Thickness of tension face FRP plate
V_c	=	Code-given shear capacity of the concrete section alone
V_{exp}	=	Experimental CDC debonding shear
V_s	=	Code-given stirrup shear strength
x	=	Distance measured along an FRP plate or strip from different points depending on the model
y_{eff}	=	Distance from FRP strip to the neutral axis of the section
α_p	=	1 for mean confidence limit
ΔV_c	=	Difference between the plated and the unplated CDC debonding shear
δ	=	Slip between the plate and the concrete on a pull test
δ_{max}	=	Maximum slip between the plate and the concrete on a pull test
ε_p	=	Strain at the centroid of FRP plate
ϕ_f	=	Aspect ratio of IC debonding failure plane

1. Introduction

1.1. Background

It is a well-known fact that maintaining aging infrastructure operational and safe while complying with economic, environmental and time constraints, currently poses a great challenge to engineers worldwide. These constraints call for more efficient solutions than the total or partial replacement of a structure.

One of such solutions has proven to be strengthening with externally bonded fiber-reinforced polymers (FRP), for either bending or shear in flexural members or as confinement in compression members. For the case of strengthening of flexural members, although the technique has been successfully used in field applications, externally bonded FRP has drawbacks that may limit its use under certain conditions, such as the tendency to debond at low strains, meaning a less efficient use of the material, lengthy preparation of the concrete surface prior to installation of the FRP, exposure of the FRP to the elements and vandalism, and possible interference with floor or pavement finishes.

The near-surface mounted (NSM) technique using FRP strips, in which thin FRP strips are bonded into narrow grooves cut in the concrete cover, overcomes these drawbacks, as NSM FRP debonds at higher strains than externally bonded FRP, the required surface preparation prior to installing the FRP is minimal, and as the FRP is installed into the concrete section, it is better protected and does not interfere with floor or pavement finishes.

However, as the NSM is a relatively recent strengthening technique, its behavior under certain failure conditions is not yet fully understood, and the existing analytical models to predict the debonding resistance of NSM strengthened sections do not cover all the possible retrofitting configurations and loading conditions that can be encountered in field applications.

Considering the many advantages and superior performance that the NSM technique has proven to have, completing the theoretical foundation to enable its safe and efficient application in the field would be of great benefit to the civil engineering industry.

1.2. Objectives

The objectives of the research presented in this thesis are:

1. Evaluate the performance of the theoretical models applicable to the debonding resistance of NSM FRP strips currently available in the literature, and identify the most outstanding gaps in knowledge.
2. Based on the findings of the previous objective, formulate a rational model for the plate-end debonding resistance of concrete flexural members strengthened with NSM FRP strips.

1.3. Scope

In order to meet the objectives outlined above, the research presented in this thesis comprised the following tasks:

1. A comprehensive literature review to identify all the currently available analytical debonding models and experimental results relevant to strengthening with NSM FRP strips.
2. Assessment of the performance of the analytical debonding models against experimental results, to identify the most outstanding gaps in knowledge.
3. Based on the findings of the previous tasks, a detailed finite element analysis to achieve a better understanding of the plate-end debonding mechanism.
4. Formulation of a rational analytical plate-end debonding model for flexural elements strengthened with NSM FRP strips, based on the findings of the literature review and the finite element analysis.

1.4. Thesis Layout

In addition to this introduction, this thesis comprises the following Chapters:

Chapter 2 presents the findings of the literature review and of the assessment of the different debonding models against experimental results.

Chapter 3 describes the finite element models developed with the aim of studying the stress distribution around the plate-ends of NSM FRP strips.

Chapter 4 provides the details of the derivation of a new analytical model to predict the plate-end debonding strength of NSM FRP strips, and compares its performance with that of the existing theoretical models.

Chapter 5 summarizes the results and conclusions reached in this research thesis, and highlights aspects that were identified as important areas for further development.

2. Literature Review

2.1. Introduction

This chapter presents basic information regarding beam retrofitting with fiber reinforced polymers (FRP) and describes the most broadly used techniques for strengthening of reinforced concrete beams using these materials. The fundamental modes of failure of beams retrofitted with FRP are also presented and the existing theoretical models developed to predict the different types of failure are described. Finally, the most relevant experimental results currently available in the literature are presented, followed by a thorough analysis of their results using the available theoretical models with the aim to evaluate their adequacy.

2.2. Beam Retrofitting with Fiber Reinforced Polymers

It is a reality that the demand for strengthening schemes on structures is constantly increasing due to aging infrastructure throughout the world and the necessity of solutions more economical and environmentally friendly than the partial or total demolition and reconstruction of a structure. Bridges are particularly vulnerable structures due to the severe environmental conditions to which they are subjected during service, which include continuous presence of moisture, freeze-thaw cycles and chloride exposure from either seawater or deicing compounds; all of which contributes to corrosion of the reinforcement, undoubtedly the prime cause of deterioration in concrete bridges. In the United States, it is estimated that nearly one-third of the concrete bridges are in need of repair or replacement; in the United

Kingdom, 10,000 concrete bridges need structural attention; in Europe, it is estimated that the repair of reinforced concrete structures due to corrosion of reinforcement costs over $600 million annually; and in Canada, the required repair costs for parking structures alone are estimated in the range of $6 billion (Hassan, 2002).

During the mid 1960's the technique of adhesively or mechanically bonding steel plates to the faces of structural elements became very popular due to its relative low cost in comparison to the other then available retrofitting methods (Hassan 2002). Although the method performed well, and even though structures retrofitted over 30 years ago have been reported to still be performing adequately (Beber et al., 2001), the method has some drawbacks, including susceptibility of the steel plates to corrosion, costly installation due to the high weight of the plates and difficult application to curved surfaces. For these reasons, during the last twenty years, interest has grown in research and field applications of FRP as a material for strengthening structures, as its high tensile capacity and stiffness, light weight and corrosion resistance help overcome the drawbacks of strengthening with steel plates.

FRP composites have been used in other areas such as the aerospace industry for many years, where their superior properties in comparison to metallic materials are well-known. In recent years however, fiber reinforced polymers have become available for its economically feasible use in the construction industry, being particularly advantageous for strengthening schemes, where the greatest cost arises from labor and interruption of services. The lightweight of FRP allows for their quick

installation on the structure without the need for heavy equipment or extensive labor, while having much higher corrosion resistance than steel plates. Some durability issues regarding the application of FRP for civil structures are yet to be further investigated, including the degradation of the FRP itself and loss of bond strength due to exposure to ultraviolet radiation, moisture, high temperatures and high pH environments (Chin et al., 1997; Hassan, 2002).

FRP composites are formed by fibers embedded in a resin matrix which binds the fibers together. Typically two types of fibers are used for retrofitting, glass fiber (GFRP) and carbon fiber (CFRP). Polymeric resins are used as both the matrix of the FRP and as the adhesive for bonding FRP to concrete (Teng et al., 2001). The tensile strength of these resins is much higher than that of concrete, such that in properly retrofitted structures failure invariably occurs in the concrete adjacent to the bonded surface. As shown in Figure 2.1, both GFRP and CFRP generally fracture at strains well below the fracture strain of steel but at much higher stresses. However the tensile strength and elastic modulus of CFRP are much higher than those of GFRP, so for the same tensile capacity, a CFRP laminate has a smaller cross sectional area than a GFRP laminate (De Lorenzis and Teng, 2007).

FRP composites are available either in prefabricated laminated sheets (pultruded) or as a system known as wet lay-up in which carbon or glass fiber fabrics are impregnated with the epoxy resin that constitutes the matrix of the material at the moment of its installation. The later method is convenient when application around corners or curved surfaces is necessary, while prefabricated pultruded plates allow for better quality control in the forming of the composite.

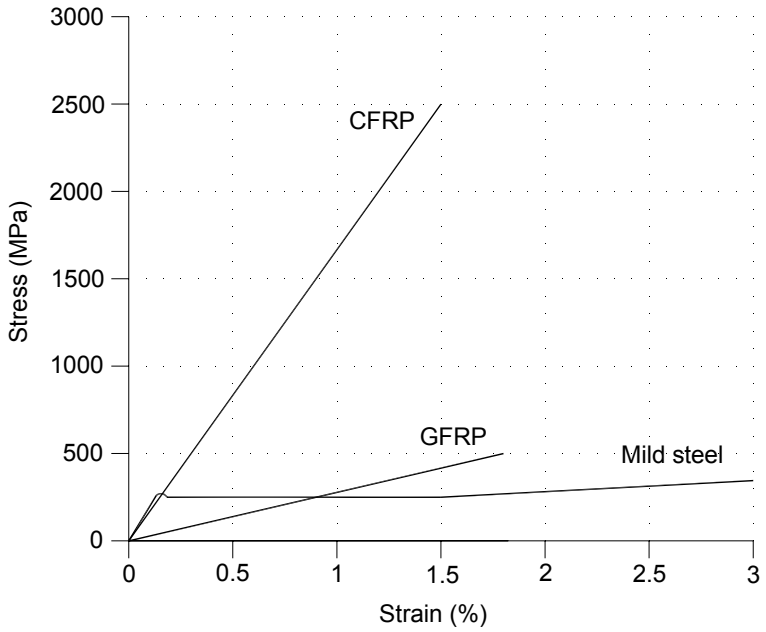

Figure 2.1. Typical FRP and mild steel stress-strain curves (Teng et al. 2001)

2.3. Retrofitting Techniques

Figure 2.2 illustrates two different techniques for strengthening concrete beams; the externally bonded (EB) technique, that consists of attaching plates either adhesively or mechanically to the outer faces of a beam or slab, and the near-surface mounted (NSM) technique, in which bars or strips are adhesively bonded in grooves cut in the concrete cover. Typically the strengthening is applied to the tension face of the element, but depending on the type of strengthening required the FRP can also be attached to the compression face or to the sides of a beam for shear strengthening.

The EB technique has proven to be an effective method of retrofitting and it has been widely used in practice and extensive research has been carried out on its different applications to the point that the behavior of the strengthened elements is considered to be well understood and guidelines are being developed worldwide,

including the ACI Committee 440, the FIB (Féderation Internationale du Béton) Bulletin 14, among others. However the technique has some drawbacks that deter designers from its use under certain conditions, considerable preparation of the concrete surface prior to installing the plate is required, and as the plate is attached to the surface of the beam it makes it prone to deterioration due to weather and vandalism. It can also interfere with floor finishes or pavement construction when installed in negative moment regions. Finally, research has shown that externally bonded plates debond early at low strains, which leads to unsafe brittle failures and does not allow for the full capacity of the material to be developed. An example of this is found in El-Hacha and Rizkalla (2005), where concrete beams strengthened in flexure using EB CFRP strips with an ultimate tensile strain of 1.1% anchored at the ends with CFRP jackets, failed by debonding of the strips at an average strain in the CFRP of 0.46%.

For these reasons in recent years interest has grown on the NSM technique as it overcomes some of the limitations associated with EB retrofitting. The NSM concept was first used in the 1940s to reinforce structures by installing steel rebar in grooves cut into the concrete cover using cement mortar as the bonding agent, today however steel rebar has been replaced by FRP composites and cement mortar has been replaced by epoxy adhesives (Sena Cruz et al., 2006). Due to the FRP being installed into the concrete and embedded in epoxy adhesive, it is better protected from the elements and vandalism, in addition to not interfering with floor finishings or pavement construction when strengthening in negative moment regions is necessary. Additionally the necessity for concrete surface preparation is minimized,

as only dust needs to be removed from the groove prior to installing the FRP. Tests have also shown that NSM reinforcement debonds at higher strains than EB reinforcement. El-Hacha and Rizkalla (2004) tested several beams strengthened with either EB or NSM FRP plates of equivalent axial stiffness, finding that for plates of equal length EB FRP reached on average a maximum strain of 0.51%, while NSM FRP reached on average a maximum strain at failure of 1.24%.

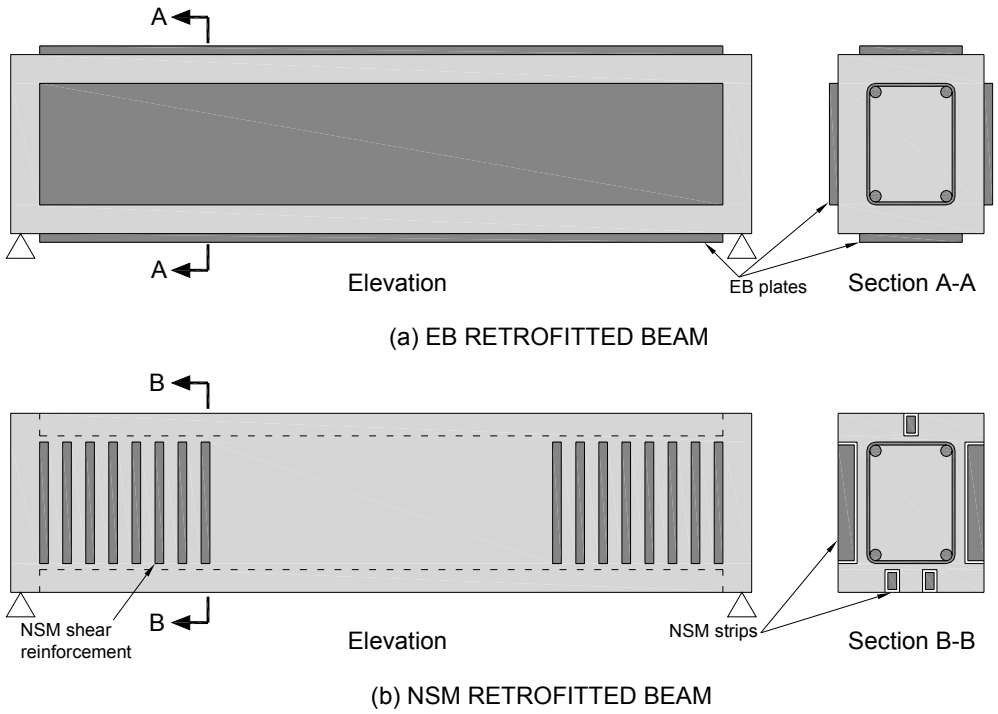

Figure 2.2. Typical beam retrofitting techniques

A factor that must be considered for NSM strengthening is that the concrete cover of the element to strengthen must be sound and deep enough to enable the effective installation of the FRP laminate, although laminates as narrow as 10 mm have shown to provide effective strengthening.

Although field applications of NSM FRP strengthening are not as common compared to EB retrofitting, the technique has already been applied with satisfactory results. In 1999 a construction error led to the necessity of strengthening a joint between a precast concrete element and a cast in situ concrete structure on a bridge. As the zone that required strengthening was to lie directly below an asphalt pavement, FRP was considered as an alternative to steel due to its corrosion resistance, and the NSM technique over EB retrofitting for simplicity of installation and for providing a safer location for the FRP to resist the expected periodical pavement resurfacing and deck sealing works, including high temperatures when pouring asphalt. The client, The Swedish Road Authority, considered the strengthening work successful and today accepts the technique as a method of strengthening concrete bridges (Taljsten et al., 2003).

Pultruded FRP composites for NSM applications are available in the form of round, square or oval bars, which can have a smooth surface or be deformed to improve the mechanical bond with the epoxy adhesive, or in the form of thin strips of different widths. In practical applications, the choice of FRP cross-sectional shape depends on the constraints imposed by the member to strengthen, such as the cover depth, and on the availability and cost of a specific shape (De Lorenzis and Teng, 2007).

The cross-sectional shape of the FRP used has a profound effect in the debonding resistance of the strengthened element, as different shapes exhibit different failure mechanisms. Strips have shown to be the least prone to debonding, as the ratio of bonded surface to cross-sectional area of the FRP is maximized,

hence minimizing the bond stresses for a given tensile force. Additionally the normal stresses induced by the longitudinal bond stresses act in the case of strips mainly towards the thick lateral concrete as shown in Figure 2.3, while in round bars the radial component of the bond stresses is resisted by circumferential tensile stresses in the epoxy cover, which may lead to the formation of longitudinal splitting cracks in the adhesive and the surrounding surface layer of concrete (De Lorenzis and Teng, 2007). As a result, the higher strains that can be achieved in the FRP using strips mean increased ultimate capacity of the strengthened beam as well as increased ductility and moment redistribution capacity (El-Hacha and Rizkalla 2004; Hassan and Rizkalla 2003). For these reasons this research focuses on the behavior of NSM strips or “plates”, as they have shown to have in general superior performance than NSM round or square bars.

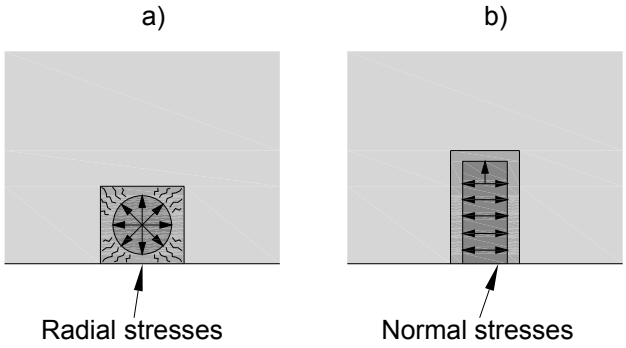

Figure 2.3. Normal bond stresses induced by a) circular bar, b) strip

Although some important conclusions about the behavior of NSM FRP retrofitted beams have been reached in recent studies, the current understanding of this strengthening method is very limited, as reflected by the absence of guidelines for

this type of reinforcement in design codes (De Lorenzis and Teng, 2007), and so extensive research is still required.

Field applications and research has shown that beams strengthened with adhesively bonded plates exhibit distinctive failure modes that depend on the beam's geometry and on the characteristics of the reinforcement used. Identifying these debonding mechanisms is essential in order to quantify the resistance of adhesively bonded plates and ultimately to design safe and reliable strengthening solutions.

2.4. Debonding Mechanisms

Three major debonding modes of failure have been identified through research and practical applications of beam and slab retrofitting with bonded plates of different materials, and will be referred to in this document as intermediate crack (IC) debonding, critical diagonal crack (CDC) debonding and plate end (PE) debonding. Different authors refer to these debonding mechanisms by different names; however they all constitute in essence the same modes of failure. Although these mechanisms were initially identified for EB plates, recent research (Smith and Teng, 2002, 2003; Teng et al., 2003) has shown that NSM FRP strips in general exhibit similar failure modes.

IC debonding initiates when a flexural or flexural-shear crack on the beam or slab intercepts the FRP plate and then starts propagating along the plate-to-concrete interface towards the plate ends to relieve the stress concentration at the intercept, as illustrated in Figure 2.4. This cracking invariably occurs in the concrete substrate

as the tensile strength of the adhesive used to bond the plate is much greater than that of concrete. When these cracks join and reach the plate ends, causing the strain in the plate to decrease, IC debonding is said to have taken place (Oehlers and Seracino, 2004).

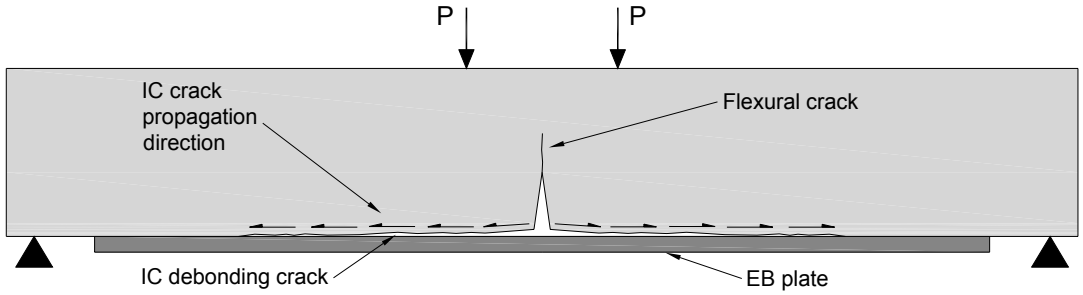

Figure 2.4. IC debonding mechanism

CDC debonding is related to a single diagonal crack that forms on a shear span of a beam, and for EB plates has been found to be mainly dependent on the shear capacity of the concrete alone. As illustrated in Figure 2.5, when shear displacement takes place along this diagonal crack, stresses are induced in the plate-to-concrete interface, causing a CDC debonding crack that starts at the diagonal crack and propagates towards the end of the plate, and can eventually cause the complete detachment of the plate in a brittle manner (Oehlers and Seracino, 2004). Stirrups are not taken into account for this type of failure as EB plates (for which models have been developed) typically debond at very low strains, hence not allowing the steel stirrups to develop any strain nor resistance. Therefore, longitudinal flexural strengthening FRP plates have the tendency to increase the shear strength and hence the CDC debonding strength of a beam, just as internal longitudinal steel reinforcement does. The IC debonding resistance of the plate also plays an

important role in the CDC debonding capacity of a section, as once a CDC has formed, further displacement along the crack will effectively pull on the plate spanning the crack, inducing tension and cracking on the plate-to-concrete interface, much like a flexural crack induces tension on the bonded interface when IC debonding occurs. This tension induced by a diagonal crack must be resisted by the bonded length between the plate end and the diagonal crack, and therefore this length has great influence on how much resistance to CDC debonding a plate can have.

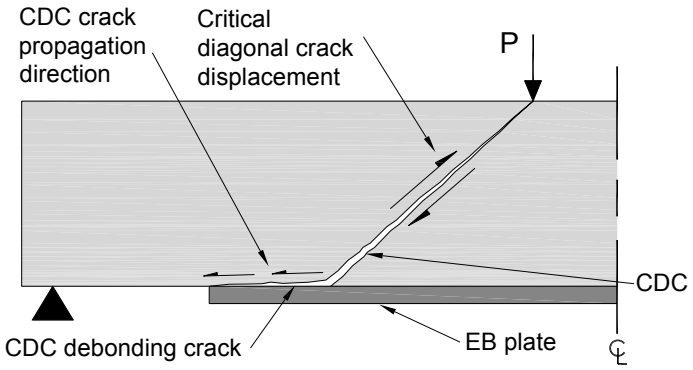

Figure 2.5. CDC debonding mechanism

PE debonding occurs when applied curvature on a beam or slab induces axial and normal stresses at the plate ends, as it tries to remain straight while the element deforms. These axial and normal stresses have to be resisted by the plate-to-concrete interface, and hence cracks can develop at the plate ends and propagate towards midspan as illustrated in Figure 2.6, which can cause the plate to debond. This type of failure is then likely to occur in shorter plates, which have their ends located in regions of high moment (Oehlers and Seracino, 2004).

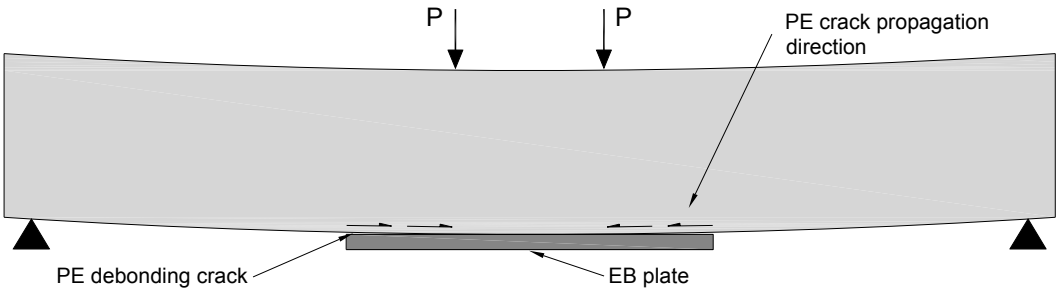

Figure 2.6. PE debonding mechanism

These three different failure modes have been observed experimentally and characterized separately to allow for their study and analytical quantification. As EB FRP typically debonds at low strains, interaction between different debonding mechanisms does not occur on members strengthened with this technique. However under certain load and support conditions on NSM retrofitted elements it is possible to have more than one failure mode acting at the same time on an element, as higher debonding strains mean cracking can develop at more than one location along the plate. Hence, care must be taken in the analysis of NSM strengthened elements, to establish whether one particular failure mode is dominating the behavior or the capacity of the structure is being affected by a combination of failure mechanisms.

The understanding of the different failure mechanisms has allowed the formulation of mathematical models to calculate the debonding resistance of adhesively bonded plates. However most of these models have been developed for EB plates, but as EB and NSM plates exhibit similar debonding mechanisms, some EB models may provide approximations of the NSM debonding behavior.

2.5. Existing Design Models Applicable to NSM Strengthening

As opposed to the externally bonded retrofitting technique, for which extensive research has been carried out for over a decade now, the existing knowledge on near-surface mounted strengthening is much more limited, and hence models to predict failure on elements retrofitted with this technique are currently not available for all the identified failure mechanisms. This section presents the models currently available in the literature applicable to NSM strengthened beams for each of the three main debonding mechanisms presented in Section 2.4.

2.5.1. IC Debonding

Seracino et al. (2006) developed a unified model to predict the IC debonding resistance of beams or slabs retrofitted with any type of adhesively bonded FRP plate (EB or NSM). The model is based on experimental results of push-pull tests (which are known to provide a lower bound to the IC debonding resistance of strengthened reinforced concrete members (Oehlers and Seracino 2004)) and equilibrium and compatibility of plate-to-concrete joints of the type shown in Figure 2.7.

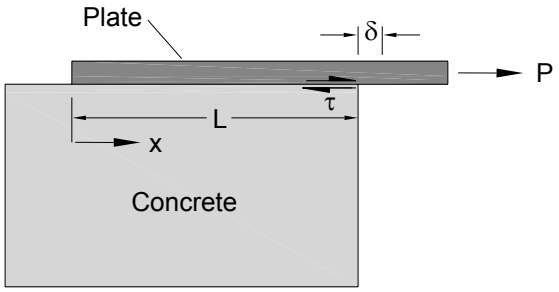

Figure 2.7. Model of push-pull test specimen

It has been shown (Yuan et al. 2004) that the differential equation defining the behavior of this type of joint is given by

$$\frac{d^2\delta}{dx^2} - Jf(\delta) = 0 \qquad (2.1)$$

where δ is the slip between the plate and the concrete, *x* is the distance from the unloaded end of the plate, *f(δ)* is a function defining the local interface shear stress-slip relationship, and *J* is a constant defined by the material and geometric properties of the joint. Mohamed Ali et al. (2006) and Chen et al. (2005) showed that although the typical shear stress-slip relationship *f(δ)* is bilinear as shown by the solid line in Figure 2.8, it can be idealized by a single softening branch as given by the dashed line in the same figure, without decrease of accuracy in the predicted debonding resistance, as δ_1 is typically an order of magnitude less than δ_{max} and the area under the two curves (which represents the fracture energy) is the same.

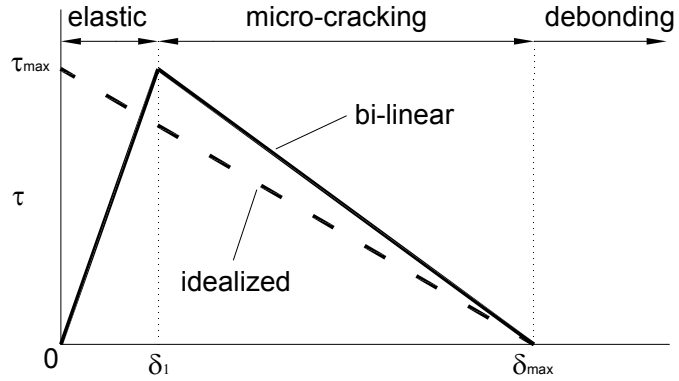

Figure 2.8. Shear stress-slip models of plate-to-concrete joints

For the idealized model in Figure 2.8, *f(δ)* is given by

$$f(\delta) = \frac{\tau_{\max}}{\delta_{\max}}(\delta_{\max} - \delta) \tag{2.2}$$

where τ_{max} and δ_{max} are the maximum shear stress and the maximum slip in the shear stress-slip model respectively.

The key difference in the development of the unified model that would allow it to be applicable for both EB and NSM retrofitting is introduced in the derivation of the constant *J*, which, as opposed to the original EB model where only the geometry of the plate is considered, takes into account the geometry of the interface debonding failure plane

$$J = L_{per}\left[\frac{1}{(EA)_{frp}} + \frac{1}{(EA)_c}\right] \tag{2.3}$$

where L_{per} is the interface debonding failure plane length as shown in Figure 2.9, and $(EA)_{frp}$ and $(EA)_c$ are the axial rigidities of the plate and the concrete components respectively. In Figure 2.9 t_b and t_d allow for the fact that debonding typically occurs in the concrete adjacent to the adhesive-concrete interface, and is taken as 1 mm.

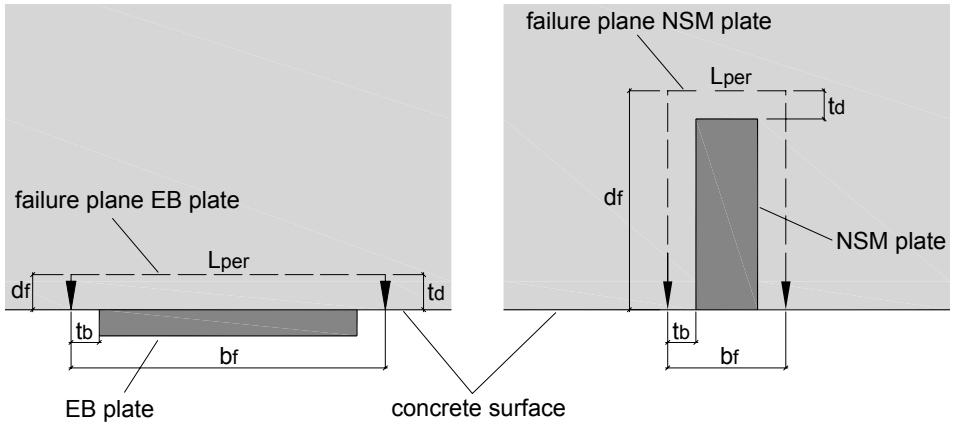

Figure 2.9. Definition of IC debonding failure plane

Substituting Equations 2.2 and 2.3 into Equation 2.1 and solving the differential equation, and simplifying taking into account that $(EA)_c$ is far greater than $(EA)_{frp}$, a closed form solution for the IC debonding resistance P_{IC} is produced

$$P_{IC} = \sqrt{\tau_{\max}\delta_{\max}}\sqrt{L_{per}(EA)_{frp}} \tag{2.4}$$

This debonding resistance will develop provided the bonded length (L in Figure 2.7) is equal or greater to the critical length L_{crit} given by

$$L_{crit} = \frac{\pi}{2\lambda} \tag{2.5}$$

where

$$\lambda^2 = \frac{\tau_{\max}L_{per}}{\delta_{\max}(EA)_{frp}} \tag{2.6}$$

This solution for P_{IC} is unique in that it is applicable to either EB plates or NSM strips. Furthermore, it was proposed that $\tau_{max}\delta_{max}$, which is twice the area under the bond stress-slip curve in Figure 2.8 and hence twice the fracture energy, is a function of the concrete cylinder compressive strength f'_c and the aspect ratio of the interface failure plane defined as

$$\varphi_f = \frac{d_f}{b_f} \tag{2.7}$$

where d_f is the length of the failure plane perpendicular to the concrete surface (depth into the concrete) and b_f is the length of the failure plane parallel to the concrete surface, as shown in Figure 2.9. φ_f is an important factor in the debonding model, as it is a measure of the confinement provided by the concrete cover, and the primary reason for improved effectiveness of NSM over EB retrofitting.

Using a function in the form

$$\tau_{\max}\delta_{\max} = C\varphi_f^m f_c'^n \tag{2.8}$$

a statistical analysis was undertaken using push-pull tests results to determine the constants C, m and n. The resultant optimized expression for design is given by

$$P_{IC} = \alpha_p 0.85\varphi_f^{0.25} f_c'^{0.33}\sqrt{L_{per}(EA)_{frp}} \tag{2.9}$$

where units are Newtons and millimeters, and α_p=1 for mean predictions, allows the prediction of the IC debonding resistance as a function only of material and geometric properties.

2.5.2. CDC Debonding

A method for calculating the CDC debonding resistance of reinforced concrete beams strengthened with EB plates is given in Oehlers and Seracino (2004). The method is based on a model developed by Zhang (1997) to determine the concrete vertical shear capacity of a beam or slab without stirrups, and incorporates the

contribution of adhesively bonded tension face plates in the CDC cracking resistance of the section. Stirrups are not taken into account for this type of failure as EB plates typically debond at very low strains, hence not allowing the steel stirrups to develop any strain.

In this method, the shear required to form the critical diagonal shear crack is first calculated as

$$((V_{dat})_{cr-plate}) = \frac{\left((x^2 + h^2)\left(\frac{b_c f_{tef}}{2} + \frac{m_p f_{ct} b_{tfp} (h + 0.5t_{tfp})}{h^2}\right)\right)}{L_O + K_M - K_W e} \qquad (2.10)$$

where, as shown in Figure 2.10, x is the horizontal distance from the point where the CDC crack is expected to initiate (the point of load application for the case of a point load) to a point where the crack intercepts the plate, h is the beam depth, b_c is the web width of the beam, m_p is the modular ratio of the plate material stiffness to that of the concrete E_{frp}/E_c, f_{ct} is the tensile strength of the concrete, b_{tfp} and t_{tfp} are the width and thickness of the plate respectively, $(h+0.5t_{tfp})$ is the vertical distance from the plate centroid to the point of applied load, L_O is the distance from the point of CDC crack initiation to the nearest beam support (for the case of a point load), K_M and K_W are ratios of the applied moment and load within L_O respectively, to the shear at the beam end, e is any distance from the point of CDC crack initiation to the resultant of loads applied over L_O (zero in the case of a point load) only in a shear span and f_{tef} is the effective tensile strength of the concrete given by

$$f_{tef} = 0.156 f_c^{'2/3} \left(\frac{h}{100} \right)^{-0.3} \qquad \text{[N and mm]} \qquad (2.11)$$

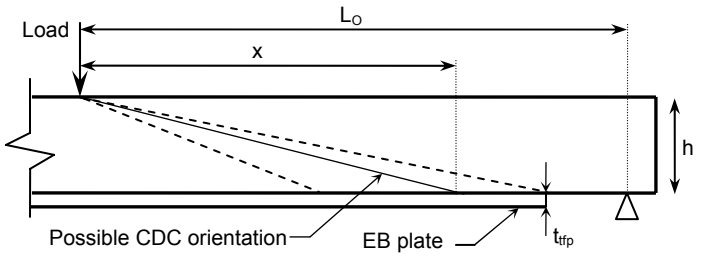

Figure 2.10. CDC debonding model for point load in simply supported beam

Once a CDC crack has formed, the shear force required to cause sliding along the crack for concentrated applied loads is given by

$$((V_{dat})_{u-pres}) = \frac{0.4 \left(f_1(f_c) f_2(h) f_3(\rho) f_4 \left(\frac{\sigma_{ps}}{f_c^{'}} \right)_{plate} \right) f_c^{'} b_c h \left(\sqrt{1 + \left(\frac{x}{h} \right)^2} - \frac{x}{h} \right)}{1 - K_W} \qquad (2.12)$$

where

$$f_1(f_c^{'}) = \frac{3.5}{\sqrt{f_c^{'}}} \quad \text{for } 5 < f'_c < 60 \text{ MPa} \quad \text{[N and mm]} \qquad (2.13)$$

$$f_2(h) = 0.27 \left(1 + \frac{1}{\sqrt{h}} \right) \quad \text{for } 0.08 < h < 0.7 \quad \text{[m]} \qquad (2.14)$$

$$f_3(\rho) = 0.15\rho + 0.58 \;, \quad \rho = \frac{A_s}{b_c h} \times 100 \quad \text{for } \rho < 4.5 \qquad (2.15)$$

$$f_4\left(\frac{\sigma_{ps}}{f_c'}\right)_{plate} = 1 + 2\frac{F_{ps}}{f_c' b_c h} + 4\frac{P_{plate}}{f_c' b_c h} \quad , \quad \sigma_{ps} = \frac{F_{ps}}{b_c h} \tag{2.16}$$

where A_s is the total area of longitudinal reinforcement crossing the CDC, F_{ps} is any applied prestressing force and P_{plate} is the lesser of the IC debonding capacity of the plate and the ultimate tensile capacity of an FRP plate or yield load of a metallic plate.

Plotting Equations 2.10 and 2.12 for values of x between the point of CDC initiation and the beam support for both the plated and the unplated beam yields a graphic as shown in Figure 2.11. The curves for unplated sections are calculated simply by using zero as plate dimensions and P_{plate} equal to zero. It can be noted that the plating of the beam has the effect of increasing both the cracking and the sliding shear resistances of the section.

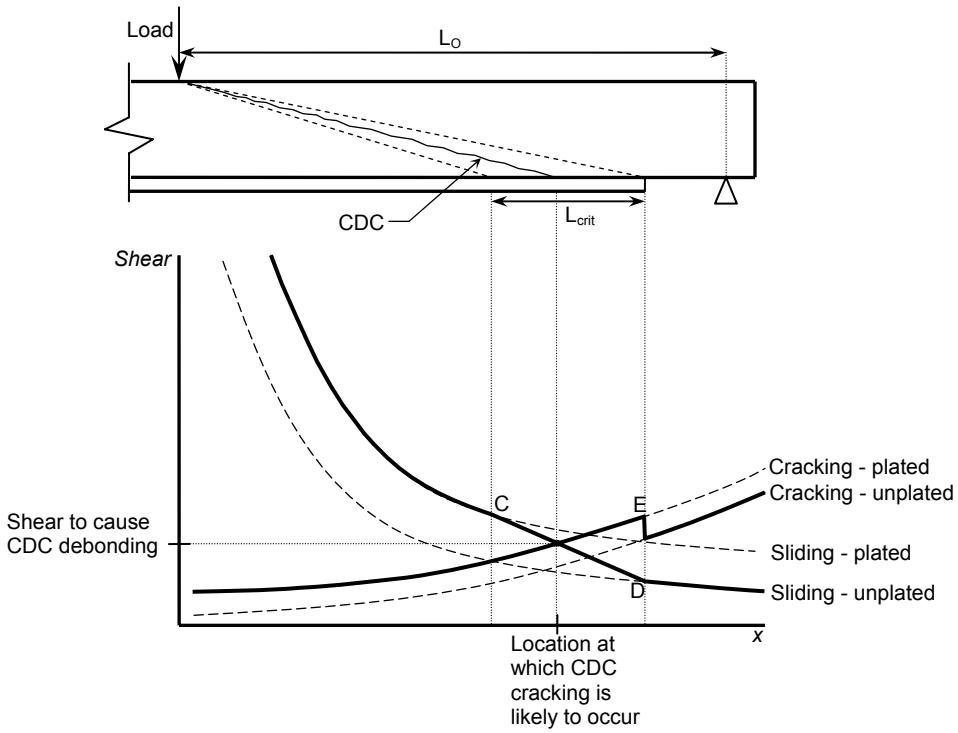

Figure 2.11. CDC debonding resistance of tension plated beams

The dashed in Figure 2.11 lines indicate the section's cracking and sliding capacities along the shear span. These capacities are affected by the location of the plate end, as P_{plate} in the sliding equation can only be developed fully beyond a distance from the plate end equal to the IC debonding development length L_{crit}, and because the cracking shear drops to that of an unplated section beyond the plate end (point E in Figure 2.11). Hence there will be a transition zone in which the sliding shear will drop gradually from that of a plated to that of an unplated section along the development length of the plate (segment C-D in Figure 2.11). The point at which the cracking and the sliding shear capacities intersect indicates the point at which CDC debonding is predicted to form and the load at which it would occur. It must be noted that this CDC debonding capacity is affected by the previously described IC debonding capacity, which can be calculated by different methods.

Although this method was developed for EB plates, minor alterations can be made to it that reflect the different geometry of a NSM plate, in an attempt to predict the CDC debonding capacity of members strengthened using this technique. By replacing the term $(h+0.5t_{tfp})$ in Equation 2.10 for $(h-0.5b_{tfp})$, the fact that the plate is installed into the concrete cover is taken into account. Additionally, to make P_{plate} and L_{crit} consistent with NSM behavior, both terms can be calculated using the method given in Section 2.5.1. Using this approach may be overly conservative, as NSM plates typically debond at higher loads and strains than EB plates, which may allow for some strength to be developed in the stirrups that is not taken into account in the EB model derivation.

2.5.3. PE Debonding

Review of all currently available literature indicated that two models for predicting PE debonding can be applicable to NSM retrofitted elements. They are presented in this section.

2.5.3.1. Oehlers and Nguyen

Oehlers and Nguyen (2000) formulated a PE debonding capacity model for plates bonded to the side faces of beams in bending. Although intended for EB plates, the debonding mechanism in which the model is based suggests that with minor modifications to account for an NSM type of geometry it may be applicable to plates bonded to the tension face of beams in bending.

Using mechanics principles the forces acting in a plate adhesively bonded to the sides of a beam in bending are first quantified, after which expressions are developed for the way those forces are transmitted from the concrete to the plates and for how they interact with each other. Using these expressions a model to calculate the moment capacity of the retrofitted beam is formulated and calibrated using experimental results to account for the complexities of the debonding mechanism.

Assuming the plate ends are far away from the high moment region of the beam and hence linear elastic behavior is applicable, and considering the plates are bonded to the concrete so the curvature in the concrete section, the plates and the composite section are the same

$$\phi = \frac{M_{RC}}{(EI)_{RC}} = \frac{M_p}{(EI)_{frp}} = \frac{M_{cmp}}{(EI)_{cmp}} \tag{2.17}$$

where M_{RC}, M_p and M_{cmp} are the moments in the concrete section, the plates and the composite section respectively, and $(EI)_{RC}$, $(EI)_{frp}$ and $(EI)_{cmp}$ are the flexural rigidities of the concrete section, the plates and the composite section respectively, the moment to cause debonding of a plate can be expressed as

$$M_p = M_{cmp} \frac{(EI)_{frp}}{(EI)_{cmp}} \tag{2.18}$$

From Figure 2.12, the strain at the centroid of a plate ε_p is given by

$$\varepsilon_p = h_{p,cmp}\phi \tag{2.19}$$

where $h_{p,cmp}$ is the distance from the centroid of the composite section to the centroid of the plate.

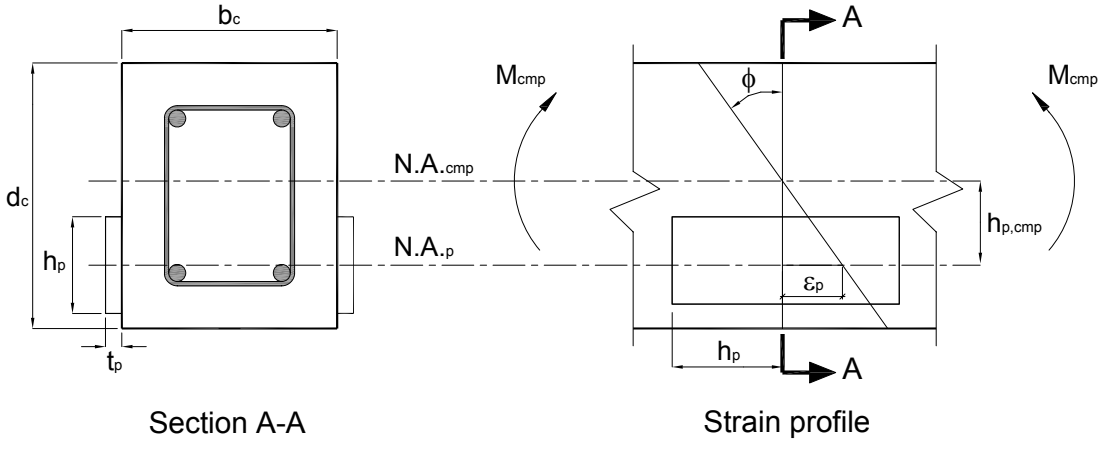

Figure 2.12. Strain profile of a side plated beam

The axial force induced in the plate due to bending F_p can then be expressed as

$$F_p = A_{frp} E_{frp} \varepsilon_p = (EA)_{frp} h_{p,cmp} \phi \tag{2.20}$$

where A_{frp} and E_{frp} are the cross sectional area and the elastic modulus of the plate, respectively. Substituting Φ from Equation 2.17 gives

$$F_p = \frac{(EA)_{frp} h_{p,cmp} M_{cmp}}{(EI)_{cmp}} \tag{2.21}$$

Now that the forces acting on the plate have been quantified, the transmission of those forces from the concrete to the plate is studied, assuming again linear elastic behavior at the ends of the plate, which are expected to be away from the high moment region of the beam. Assuming that although initially the moment on the plate is transmitted over the area h_pxh_p in Figure 2.13 (a), premature debonding is likely to occur at the corners of the plate and hence M_p will eventually be transmitted on the circular area of diameter h_p as shown in Figure 2.13 (b).

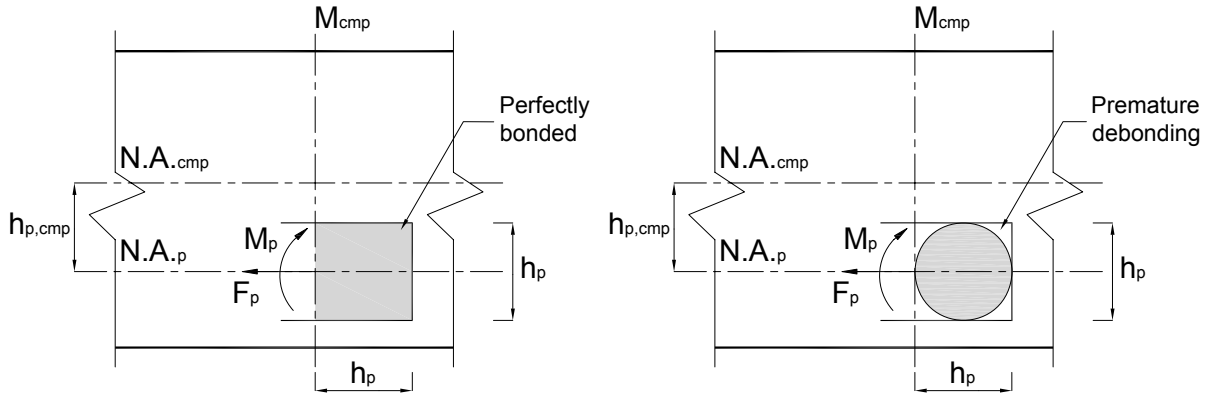

a) Perfectly bonded b) Allowing for debonding

Figure 2.13. Bending moment transmission model on a side plate

From Figure 2.14, the shear stress τ_h at a distance *h* from the center of the transmission zone varies linearly according to

$$\tau_h = \frac{2h\tau_{\max}}{h_p} \tag{2.22}$$

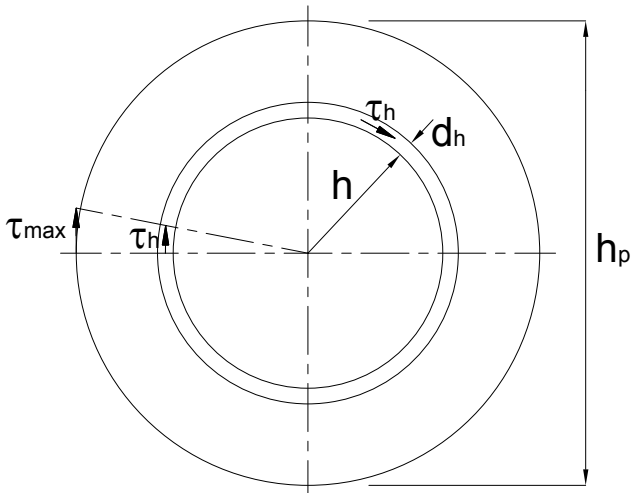

Figure 2.14. Distribution of bond stress resisting M_p

The differential increment in moment due to τ_h is then given by

$$dM = 2\pi h\tau_h hdh = \frac{4\pi h^3\tau_{\max}dh}{h_p} \tag{2.23}$$

Integrating over the circular stress transmission area and substituting for M_p in Equation 2.18 yields the expression for maximum shear in the plate to concrete interface induced by the plate bending

$$\tau_{\max} = \frac{16 M_{cmp} (EI)_{frp}}{\pi h_p^{\,3} (EI)_{cmp}} \tag{2.24}$$

Considering now the transmission of the stresses on the interface induced by axial force on the plate, it can be seen from Figure 2.15 that the axial force F_p acts at a distance $t_p/2$ from the plate to concrete interface; this eccentricity induces forces F_a normal to the interface to balance the couple $F_p t_p/2$. The couple formed by the F_a forces must then be proportional to the plate thickness, as indicated by the distance $k_1 t_p$ in Figure 2.15.

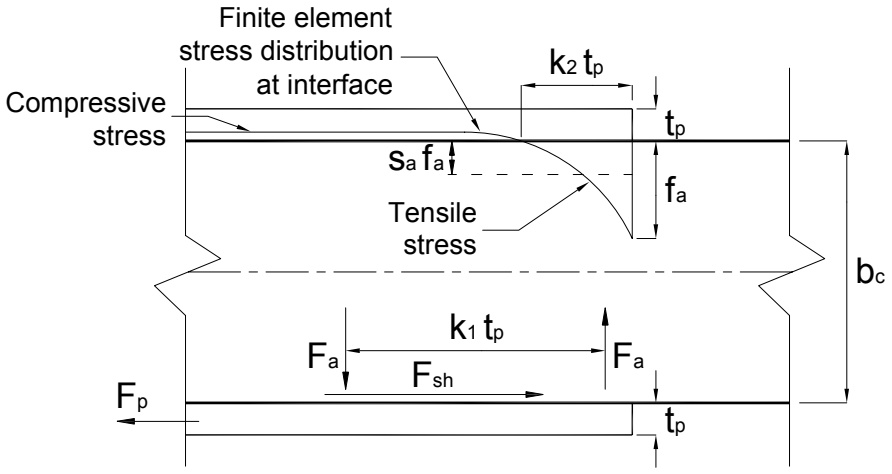

Figure 2.15. Axial force transmission model on a side plated beam (view from top of beam)

From the equilibrium of forces acting on the plate

$$F_a = \frac{F_p}{2k_1} \tag{2.25}$$

The distribution of stresses normal to the bonded interface found through finite element analyses is shown adjacent to the upper plate in Figure 2.15. It can be seen that the tensile stresses, that have a peak stress f_a are concentrated over a short distance at the plate end that is proportional to the plate thickness $k_2 t_p$. Defining the shape of the tensile stress distribution as s_a, where the mean tensile stress is $s_a f_a$,

$$F_a = (s_a f_a)(k_2 t_p) h_p \tag{2.26}$$

Substituting Equation 2.25 into Equation 2.26, with $F_p = f_p t_p h_p$, where $f_p = E_{frp} \varepsilon_p$

$$f_a = k_a E_{frp} \varepsilon_p \tag{2.27}$$

Substituting Equations 2.17 and 2.19 into Equation 2.27 gives the maximum normal stress across the interface as

$$f_a = k_a E_{frp} h_{p,cmp} \phi = k_a E_{frp} \frac{M_{cmp}}{(EI)_{cmp}} h_{p,cmp} \tag{2.28}$$

Debonding of the plate is assumed to occur when the principal stress at the plate end reaches the tensile capacity of the concrete. The shear stress τ_{sh} in Figure 2.16 is assumed to tend to zero towards the plate end, and hence disregarded for the principal stress calculation.

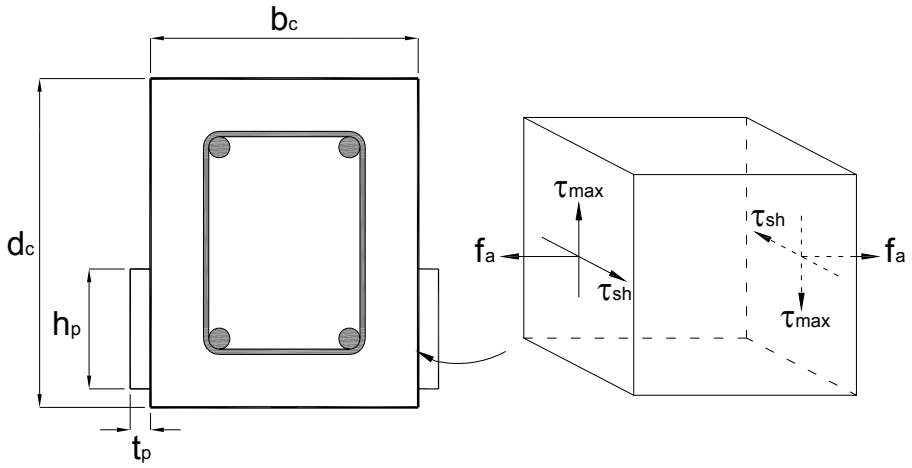

Figure 2.16. Debonding stresses at the ends of side plates

Using Mohr's circle to calculate the principal stress in terms of f_a and $\tau_{\max}$, and equating it to the concrete tensile capacity f_{ct}, an expression for the debonding stress capacity is obtained:

$$f_{ct} = 0.5 f_a + \sqrt{\tau_{\max}{}^2 + (0.5 f_a)^2} \tag{2.29}$$

Equation 2.29 can be written as

$$f_{ct} = 0.5 f_a + k_R \tau_{\max} + 0.5 f_a \tag{2.30}$$

where $k_R = f(\tau_{\max}, f_a)$. Assuming k_R is a constant, Equation 2.30 can be written as

$$f_{ct} = f_a + k_R \tau_{\max} \tag{2.31}$$

Substituting Equations 2.24 and 2.28 and $I_p = t_p h_p^3/12$ into Equation 2.31 gives

$$k_A + k_B\left(\frac{t_p}{h_{p,cmp}}\right) = \frac{f_{ct}(EI)_{cmp}}{M_{cmp}E_{frp}h_{p,cmp}} \tag{2.32}$$

which can be written as

$$k_A + k_B X = Y \tag{2.33}$$

where

$$X = \frac{t_p}{h_{p,cmp}} \tag{2.34}$$

$$Y = \frac{f_{ct}(EI)_{cmp}}{M_{cmp}E_{frp}h_{p,cmp}} = \frac{f_{ct}}{E_{frp}\varepsilon_p} \tag{2.35}$$

The constants k_A and k_B in Equation 2.33 were determined experimentally from tests carried out by Oehlers and Nguyen on six beams in four-point bending, strengthened with short adhesively bonded side plates on both sides of different widths and thicknesses located in the constant moment region. The measured debonding moments for plates on each side of the beams were taken as M_{cmp} and the specimens' material and geometric properties used for the different variables in 2.34 and 2.35. From Figure 2.17 k_A is given by the Y intercept as 0.0185 and k_B is given by the slope of the linear tendency line as 0.185

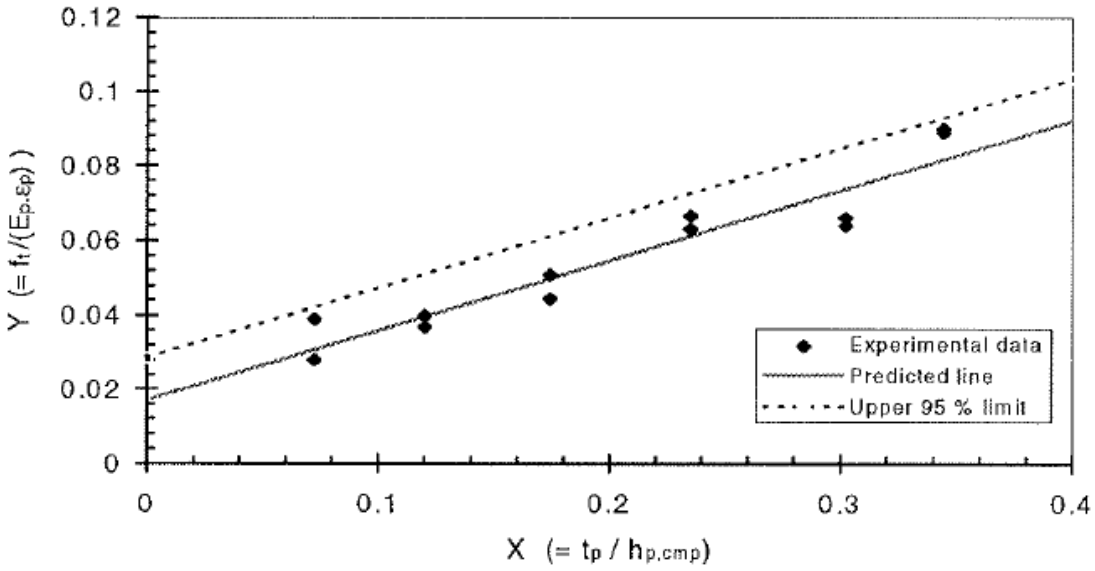

Figure 2.17. Experimental calibration of the mathematical model (Oehlers and Nguyen, 2000)

Substituting k_A and k_B into Equation 2.32 an expression for the plate end debonding moment capacity of the side plated retrofitted beam is obtained

$$M_{cmp} = \frac{f_{ct}(EI)_{cmp}}{E_{frp}(0.0185h_{p,cmp} + 0.185t_p)} \tag{2.36}$$

Up to this point a summary of the derivation of Oehlers and Nguyen's PE debonding model for EB side plates has been given in this Section, with the aim of understanding how the model works. Next, the considerations made to use this model for PE debonding of NSM strips are discussed.

As opposed to EB side plates, NSM plates are bonded to the concrete on both sides as shown in Figure 2.18, hence an approximation to NSM PE debonding

behavior could be made by doubling the debonding moment capacity to reflect the greater bonded area of the NSM technique.

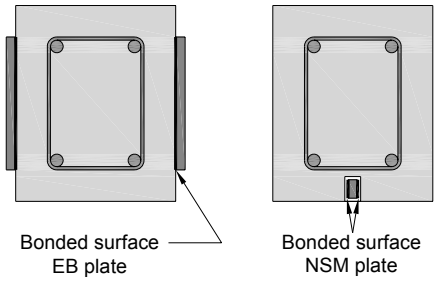

Figure 2.18. Bonded surfaces of EB side plates and NSM plates

Care must be taken when using this approach for NSM plates, as the model was calibrated experimentally for plates whose centroid was in the tensile region of the beam and at a distance from the centroid of the composite section between 0.09 and 0.43 times the effective depth of the concrete section. Typically for the applications considered in this document a NSM plate will be in the tensile region of the beam, but as plates are much narrower and closer to the extreme tension fiber of the beam, their centroid will be outside the range of distances from the centroid of the composite section for which the model was calibrated.

This approach of accounting for the double bonded area of NSM plates may be considered only as a first rough approximation to NSM behavior, as in addition to the issues mentioned above, the fact that NSM plates are surrounded by thick concrete rather than being only glued to the outer sides of a beam can also mean a different stress distribution at the plate ends.

2.5.3.2. Hassan and Rizkalla

Hassan and Rizkalla (2003) proposed a model based on a combined shear-bending model introduced by Malek et al. (1998) for EB plates, but accounting for the double bonded area of NSM plates and the continuous reduction in flexural stiffness of a concrete section in bending. A summary of the derivation and use of the model is presented in this Section.

Using mechanics principles, and considering as a starting point the equilibrium of an infinitesimal section of NSM plate subject to axial tension as shown in Figure 2.19, an expression that can be used to establish the debonding capacity of the strengthened section is developed. Debonding of the plate is considered to occur due to only shear stress τ in the axial direction, and in deriving its value the stress in the concrete adjacent to the adhesive layer, σ_c in Figure 2.19, is taken into account, which introduces axial stress resulting from bending of the beam.

The derivation of σ_c is conditioned by the load configuration, and hence the final debonding stress capacity expression is specific for a certain load condition. For the case of a simply supported beam subjected to a single concentrated load the final expression for the axial shear stress on the plate to concrete interface is

$$\tau = \frac{t_s}{2}\left[\frac{nPl_o y_{eff}}{2I_{eff}}\omega e^{-\omega x} + \frac{nPy_{eff}}{2I_{eff}}\right] \tag{2.36}$$

where

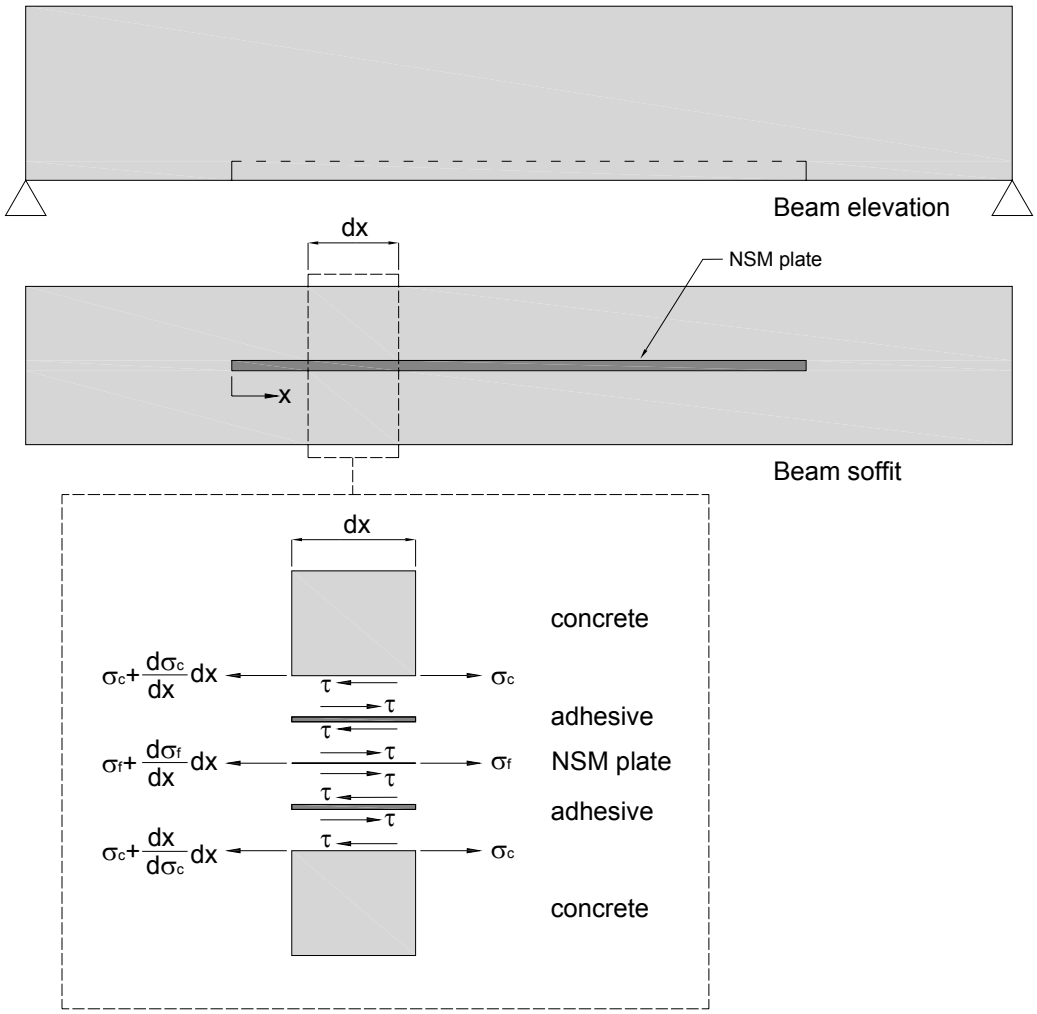

Figure 2.19. NSM plate debonding model

$$\omega^2 = \frac{2G_a}{t_a t_s E_{frp}} \tag{2.37}$$

$$n = \frac{E_{frp}}{E_c} \tag{2.38}$$

G_a is the shear modulus of the adhesive, t_a is the thickness of the adhesive layer, t_s is the thickness of the FRP strip, E_{frp} and E_c are the modulus of elasticity of the FRP

strip and the concrete respectively, P is the applied concentrated load, e is the base of the natural algorithm, y_{eff} is the distance from the strip to the neutral axis of the section, l_o is the distance from a beam support to the nearest plate end, x is the distance measured from the plate end as shown in Figure 2.19 and I_{eff} is the expression developed by Branson and Trost (1982)

$$I_{eff} = \left(\frac{M_{cr}}{M_a}\right)^3 I_{g(transformed)} + \left(1 - \left(\frac{M_{cr}}{M_a}\right)^3\right) I_{cr(transformed)} \qquad (2.39)$$

where M_{cr} and M_a are the cracking and applied moments respectively, and I_g and I_{cr} are the gross and cracked moments of inertia of the transformed strengthened section respectively. By including I_{eff} in the model the gradual decrease in flexural stiffness of the concrete section due to flexural cracking is taken into account.

For the case of a simply supported beam subjected to two concentrated loads the axial shear stress on the plate to concrete interface becomes

$$\tau = \frac{t_s}{2}\left[\frac{nPy_{eff}}{I_{eff}} + \frac{nPy_{eff}\, l_o}{I_{eff}}\,\omega e^{-\omega x}\right] \qquad (2.40)$$

Equations 2.36 and 2.40 are a function of x, the distance measured from the plate end, and hence they can be used to calculate the interface shear stress at any point in the plate for a given section and load condition, however τ will always be

greatest at *x*=0, meaning that the plate end is the most critical point and hence debonding of the plates would always be expected to initiate here.

Having quantified the shear stress on the plate to concrete interface, a failure criteria based on the concrete capacity is introduced, as the shear strength of the FRP and the adhesive is typically well above that of concrete. Knowing the compressive and tensile strength of concrete, the Mohr-Coulomb line can be represented as shown in Figure 2.20

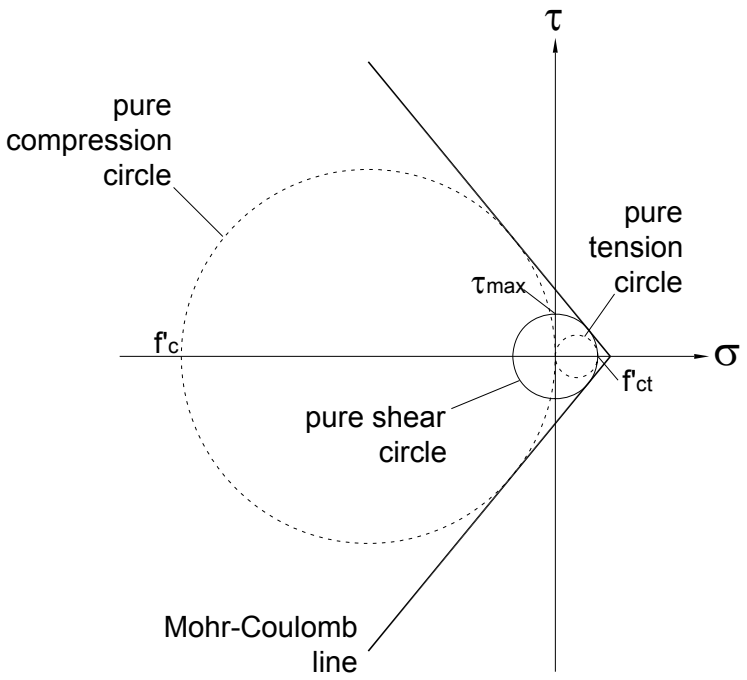

Figure 2.20. Mohr-Coulomb failure criterion

All circles tangential to the Mohr-Coulomb line represent a critical stress combination, and the maximum critical shear stress for the pure shear circle is given by

$$\tau_{\max} = \frac{f'_c \ f_{ct}}{f'_c + f_{ct}} \tag{2.41}$$

where f'_c and f_{ct} are the compressive and tensile strengths of concrete, respectively.

The retrofitted beam will then fail at a load P for which the shear stress given by Equations 2.36 or 2.40 equals $\tau_{\max}$ given by Equation 2.41.

The following section presents all available experimental results on strengthening with NSM plates, and compares them with results obtained using the proposed theoretical models in order to evaluate their adequacy.

2.6. Existing Experimental Results and Evaluation of Theoretical Models

With the aim of evaluating the accuracy with which the models presented in Section 2.5 can predict the debonding resistance of a section to the different failure modes, all experimental results available in the literature of tests carried out on reinforced concrete beams strengthened with near-surface mounted FRP strips were checked against theoretical predictions.

The theoretical prediction of the beams' IC debonding capacity P_{IC} (axial force on the plate) obtained using the unified model developed by Seracino et al. (2006), was translated to an ultimate applied force on the beam through a non-linear layered sectional analysis of the beam section. Equation 2.9 was first used to calculate the predicted ultimate axial force on the plate, after which using linear elastic theory the corresponding strain in the plate was calculated as $\varepsilon_{IC}=P_{IC}/(EA)_{frp}$, where $(EA)_{frp}$ is the axial rigidity of the FRP plate. Assuming a linear strain distribution over the cross

section as shown in Figure 2.21, the strain in the concrete and steel reinforcing is determined to achieve longitudinal equilibrium maintaining ε_{IC} at the FRP plate level, using the appropriate material properties for each layer (the tensile strength of concrete was ignored). In other words, the section analysis was done assuming the flexural capacity of the strengthened sectional is governed by IC debonding of the NSM FRP strip.

Through an iterative process the neutral axis depth is found based on equilibrium of forces, and finally the applied moment on the section is calculated as the sum of moments about the neutral axis arising from the forces on the different layers that make up the beam section. Considering the load configuration of the beam, the moment at the critical section can easily be transformed into applied load for comparison with reported experimental results.

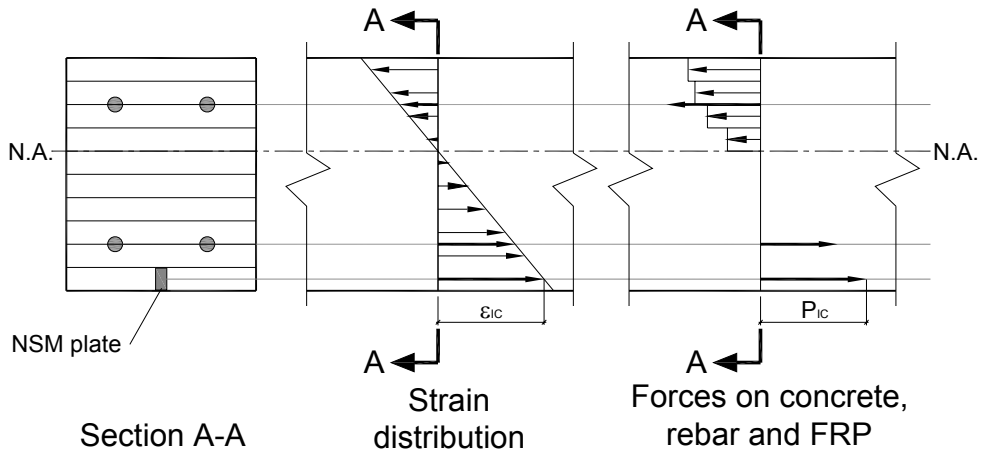

Figure 2.21. Strain and force distributions for layered sectional analysis

For specimens strengthened with FRP strips in more than one groove, the interface debonding failure plane that defines the terms $\varphi_f=d_f/b_f$ and L_{per} in Equation 2.9, was calculated both as one that covers individual NSM strips, as shown in Figure 2.22 a), and as a single failure plane encompassing all the strips such that failure occurs as a group, as illustrated in Figures 2.22 b) and c). This was done with the aim of identifying what the most appropriate approach would be, given that Seracino et al.'s model was not specific as to how φ_f should be defined. The area of FRP used in Equation 2.9 was the total area of the number of FRP strips surrounded by the chosen failure plane. Once the IC debonding strain in the FRP is calculated assuming either one of the failure planes, the subsequent section analysis is carried out using the total area of FRP strengthening.

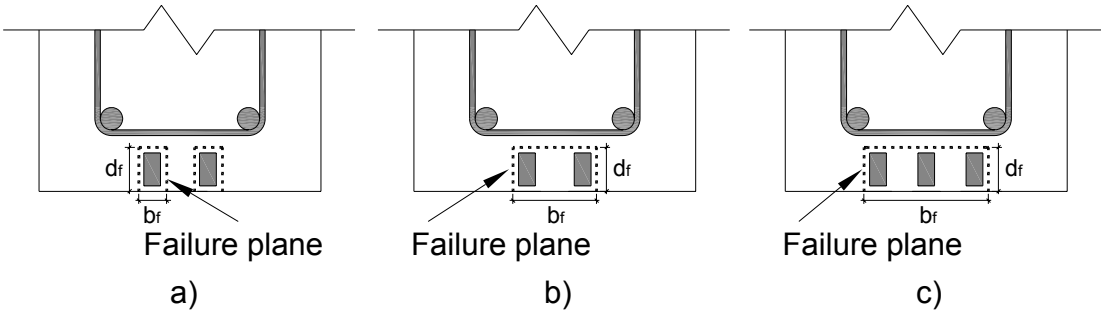

Figure 2.22. IC debonding assumed failure planes for multiple strips

The theoretical predictions for CDC debonding capacity of the different specimens were made using the method given in Section 2.5.2. By plotting Equations 2.10 and 2.12 for a shear span of the specimen, the CDC debonding load is given by the intersection of the curves of the two equations. In calculating

Equation 2.12, P_{IC} and L_{crit} from Equations 2.9 and 2.5 respectively, of the unified IC debonding model presented in Section 2.5.1, were used. The differences in P_{IC} and L_{crit} induced by the different assumed failure planes discussed before showed to produce negligible differences in the CDC debonding capacities of the specimens.

The PE debonding capacity of the specimens was calculated theoretically using the Oehlers and Nguyen method given in Section 2.5.3.1. The specimen's PE debonding moment capacity was calculated by direct application of Equation 2.36, and then multiplying that value by 2 to account for the double bonded area of NSM strips.

The model developed by Hassan and Rizkalla presented in Section 2.5.3.2 was also used to calculate failure loads for the different specimens. Through this method the interfacial shear stress was calculated for different applied loads, using either Equation 2.36 or Equation 2.40 depending on the load configuration of the specimen, and then compared with the failure criteria given by Equation 2.41; the load for which the interface shear stress equaled the failure criteria indicated the plate end debonding load. In Equations 2.36 and 2.40, x was always taken as zero, because this value maximizes the calculated shear stress. An iterative process of calculating the interface shear stress for different load levels is necessary as Equations 2.36 and 2.40 are a function of the effective moment of inertia of the transformed section I_{eff}, which decreases as the applied moment increases. Hassan and Rizkalla's model was not labeled by the authors as a PE debonding model, as it allows the calculation of interfacial shear stresses at any point along an FRP plate; however as mentioned before when using the model the highest shear stress for a

given cross section is always found to take place at the plate end, where x equals zero. In the following sections the experimental programs most relevant to NSM strengthening available in the literature are summarized, and their results used to assess the adequacy of the existing debonding analytical models.

2.6.1. Hassan and Rizkalla

Hassan and Rizkalla (2003) tested nine 2.5 m span reinforced concrete T beams of cross-section and reinforcement as shown in Figure 2.23, eight of which were strengthened with a single 1.2x25 mm NSM CFRP strip of varying length bonded into a 5x25 mm groove in the tension concrete cover, while one was tested without FRP reinforcement for reference. The beams' cross-section and reinforcement were designed to induce flexural failure at midspan and to avoid concrete crushing failure at low applied loads.

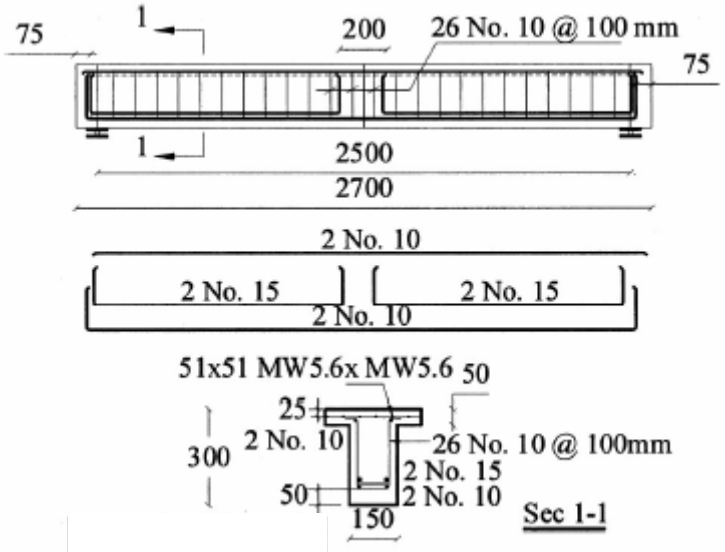

Figure 2.23. Typical specimen details (Hassan and Rizkalla, 2003)

Table 2.1. Hassan and Rizkalla test results

Beam	Strengthened length (mm)	Failure load (kN)	Failure strain in FRP (%)	Failure mechanism
B8	2400	80	1.31	FRP rupture
B7	2100	80	1.29	FRP rupture
B6	1900	75	1.28	FRP rupture
B5	1700	79	1.27	FRP rupture
B4	1500	74	1.18	Debonding at both ends of the strip and at midspan. Final debonding controlled by plate end debonding
B3	1000	60	0.71	Debonding at both ends of the strip and at midspan. Final debonding controlled by plate end debonding
B2	500	54	0.17	Plate end debonding
B1	300	53	0.049	Plate end debonding
B0	Reference	52	-	Steel yielding followed by concrete crushing

Table 2.1 shows the strengthened length, the experimental ultimate failure loads and strains in the FRP, and the failure mechanism described by the authors for each specimen. It must be noted here and in subsequent tables that measured ultimate strain is not necessarily the maximum, as it can vary depending on the gauge location relative to concrete cracks. Beams with short strengthened lengths, B1 and B2, failed by plate end debonding and had a negligible increment in ultimate capacity compared to the unstrengthened beam. Beams B3 and B4 strengthened with 1000 and 1500 mm long strips respectively, failed at loads 13% and 30% higher, respectively, than the unstrengthened beam, and the strips debonded at the ends although interface debonding cracks at midspan was also observed. On beam B5 strengthened with a 1700 mm long strip the FRP capacity was fully developed as

it failed by FRP rupture. Further increase of the strengthened length on beams B6 through B8 showed to have little effect on the ultimate capacity of the strengthened section as it would be expected, since the failure of these beams would be governed by rupture of the FRP plate.

Table 2.2 shows experimental failure loads and theoretical debonding loads calculated using the different models identified in Section 2.6. The shaded values indicate the lowest calculated failure load (without considering the theoretical loads of Hassan and Rizkalla's model) and hence the predicted debonding mechanism for each specimen.

Table 2.2. Hassan and Rizkalla test results analysis

Beam	Theoretical prediction					Experimental results	
	IC		CDC	PE	Hassan & Rizkalla model (kN)	Failure load (kN)	Failure strain in FRP (%)
	Failure load (kN)	Failure strain (%)	Failure load (kN)	Failure load (kN)			
B8	66.08	1.62	116.00	812.40	FRP rupture	80.00	1.31
B7	66.08	1.62	116.00	203.10	FRP rupture	80.00	1.29
B6	66.08	1.62	116.00	135.40	FRP rupture	75.00	1.28
B5	66.08	1.62	116.00	101.55	70.00	79.00	1.27
B4	66.08	1.62	114.00	81.24	55.00	74.00	1.18
B3	66.08	1.62	110.00	54.16	37.50	60.00	0.71
B2	66.08	1.62	110.00	40.62	27.50	54.00	0.17
B1	61.70	1.42	110.00	36.93	25.00	53.00	0.05

It can be seen that, except in the case of beam B4, the failure mechanisms predicted agreed with experimental observations, and the failure loads were always underestimated, although by a greater amount for the shorter bonded lengths of beams B1 and B2. It must be taken into account when using the unified IC

debonding model that it is based on IC debonding of pull-push tests, which as mentioned before, provide a lower bound of the IC debonding on beams. Regarding the theoretical results for beam B4, it must be noted that although the final debonding of the CFRP strip took place at the plate ends, debonding was also observed experimentally at flexural cracks for bonded length 1000 mm and 1500 mm, which indicates that IC debonding was also likely to occur in beams B4 ad B3, hence making it difficult to discern theoretically what the debonding mechanism would be for these beams.

Hassan and Rizkalla's model was developed as part of the same research from which these experimental results derived. The theoretical shear stresses calculated by Hassan and Rizkalla using Equation 2.36 for different applied loads are shown in Figure 2.24.

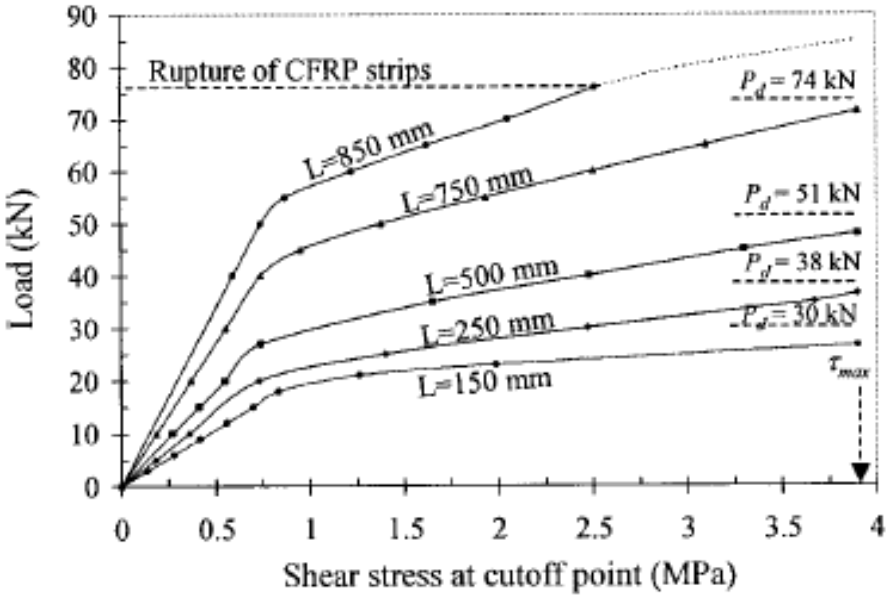

Figure 2.24. Theoretical shear stresses on plate-to-concrete interface (Hassan and RIzkalla, 2003)

It can be seen from the authors' analysis that for strengthened lengths 1700 mm and higher (L in Figure 2.24 represents the strip length measured from midspan to a strip end) the strips theoretically exceed their rupture load before reaching the predicted debonding plate-to-concrete interface shear stress τ_{max}, and hence the predicted failure was rupture of the FRP, which agrees with the experimental results. For strengthened lengths 1500 mm and below (beams B4 through B1), the debonding loads are the ordinates of the curves corresponding to shear stress τ_{max} in Figure 2.24. Compared to experimentally measured debonding loads, shown as P_d in Figure 2.24, which are not the experimental ultimate loads from Tables 2.1 and 2.2 at which the strips detached from the beam, but the loads at which signs of debonding were first recorded, the model predictions showed to be in good agreement with the experimental results, having errors of less than 10%.

The same analysis done by Hassan and Rizkalla was carried out and the results are illustrated in Figure 2.25. Using the same theoretical FRP rupture load and debonding shear calculated by Hassan and Rizkalla, Figure 2.25 shows that FRP rupture was predicted for beams B8 through B6 but not for B5, and that compared to experimentally measured debonding loads (P_d in Figure 2.24), these predictions are up to 26% lower. The reasons for these differences are unclear, as the model was applied according to the authors' description and their same material properties were used. The one variable that is thought could have caused the difference in the results is the assumed value of *x*, which for the reasons explained in Section 2.6 was taken as zero in the current analysis. If a higher value of *x* was assumed, the predicted debonding load for a given specimen would be higher.

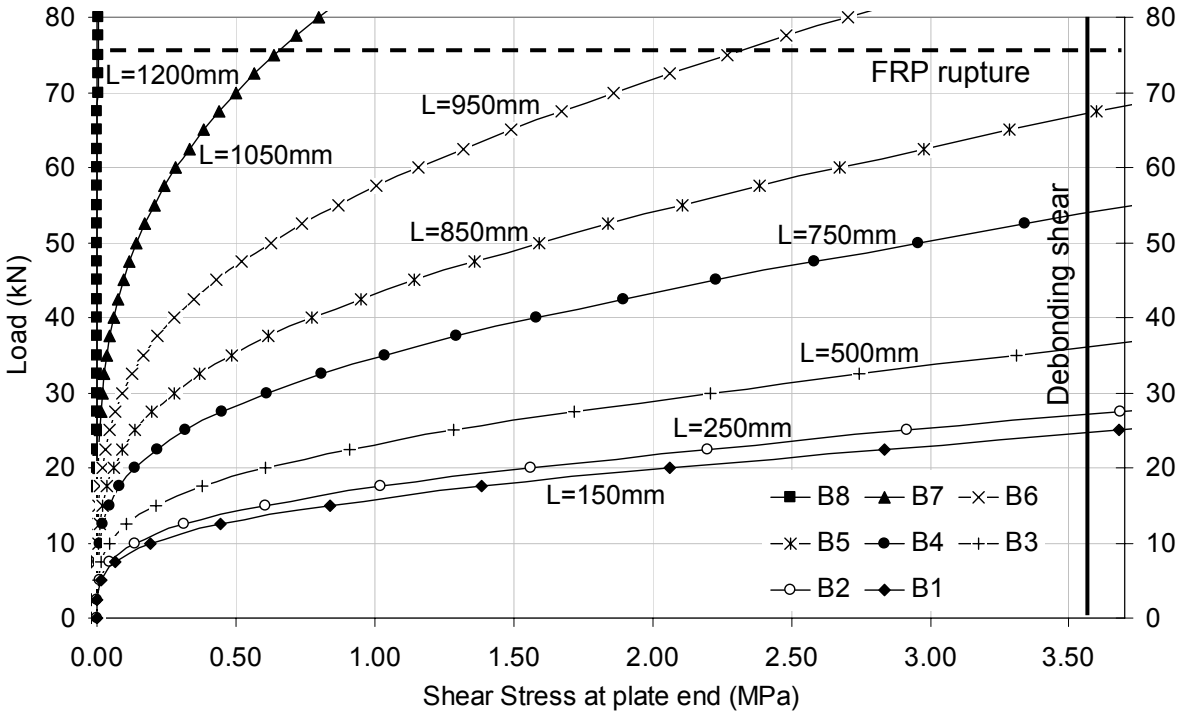

Figure 2.25. Theoretical shear stresses on plate-to-concrete interface from Hassan and Rizkalla's model

2.6.2. El-Hacha and Rizkalla

El-Hacha and Rizkalla (2004) tested eight 2.5 m span reinforced concrete T beams of cross-section and reinforcement as shown in Figure 2.26. Different types of EB and NSM strengthening were applied to seven of the specimens, out of which two were strengthened using NSM CFRP strips (beams B2 and B3) and one strengthened using NSM GFRP strips (beam B4), and hence only these results were analyzed here. Test variables between these beams were the strips dimensions and strengths, although the FRP reinforcement was designed to maintain the axial stiffness (EA) of the strips constant, which according to classical beam theory would induce identical load-deflection behavior for all specimens. To achieve this, and due

to the different strengths of the FRP used, different numbers and sizes of strips were required. In the case of beam B4 strengthened with GFRP, five strips were installed in three grooves as shown in Figure 2.26, two bonded together in the outer grooves and one in the middle groove. All FRP reinforcement was terminated 50 mm short of the supports, hence a strengthened length of 2400 mm was constant for all specimens.

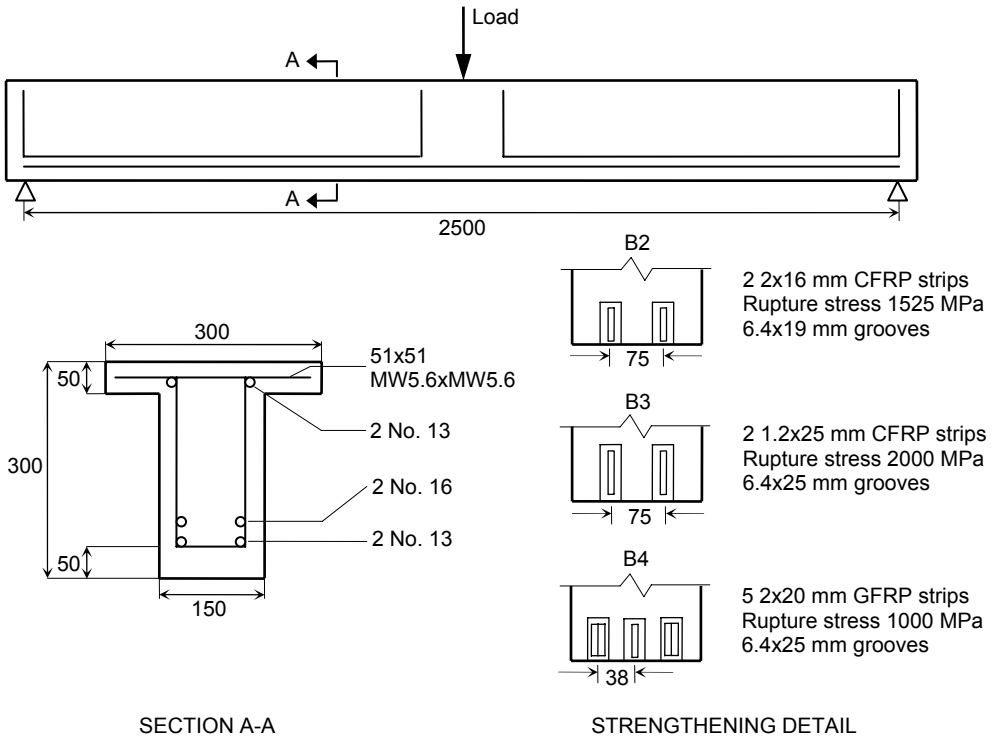

Figure 2.26. El-Hacha and Rizkalla specimen details and test set-up

Table 2.3 shows experimentally measured failure loads and strains in the FRP, as well as the failure mechanisms described by the authors and observed in photographs of the specimens after failure. It can be noted from the nearly equal failure loads that similar strengthening was achieved in the specimens by

maintaining the same axial stiffness in the reinforcement FRP. The FRP rupture strains measured for beams B2 and B3 were consistent with the ultimate rupture strains reported by the manufacturer of 1.08 and 1.33 % respectively. The different failure mechanism of beam B4 was attributed by the authors to a higher ultimate strain capacity of the GFRP of 2.22 % and to a thinner layer of adhesive in the outer grooves, which combined would have induced higher shear stresses in the concrete-epoxy interface.

Table 2.3. El-Hacha and Rizkalla test results

Beam	Strengthened length (mm)	Failure load (kN)	Failure strain in FRP (%)	Failure mechanism
B0	Reference	55.4	-	Steel yielding followed by concrete crushing
B2	2400	99.3	1.34	CFRP rupture with concrete debonding at midspan. Photographs of tested beam suggest IC debonding had started to develop prior to strip rupture.
B3	2400	110.2	1.38	CFRP rupture with concrete debonding at midspan. Photographs of tested beam suggest IC debonding had started to develop prior to strip rupture.
B4	2400	102.7	1.35	IC debonding. Splitting of the concrete at the GFRP-concrete interface initiating at the beam midspan.

Table 2.4 shows experimental failure loads and strains and theoretical debonding loads predicted for each failure mechanism. The theoretical IC debonding loads are presented for failure planes assumed both as a common failure plane which includes all grooves and as individual strip failure planes. It can be noted that the assumption of a common failure plane produced lower failure strains, and hence lower failure

loads, due to a reduced ratio of resisting area to FRP area, in comparison with the single strip failure planes assumption.

The shaded values indicate the lowest calculated debonding force for each specimen and hence the predicted failure mechanism. Note that regardless of the failure plane assumption made, the predicted failure mechanism remains the same. Experimental results showed that signs of IC debonding had started to develop in beams B2 and B3 before rupture of the FRP, and that beam B4 failed by IC debonding, which agrees with the predicted failure mechanism for all three specimens, regardless of the failure plane assumption made. The IC debonding loads and strains calculated using the unified model with individual strip failure planes produced results close to the experimental ones, although the debonding resistance was overestimated for specimen B4.

Table 2.4. El-Hacha and Rizkalla test results analysis

Beam	Theoretical prediction							Experimental results	
	IC				CDC	PE	Hassan & Rizkalla model	Failure load (kN)	Failure strain in FRP (%)
	Common failure plane		Individual strip failure planes						
	Failure load (kN)	Failure strain (%)	Failure load (kN)	Failure strain (%)	Failure load (kN)	Failure load (kN)			
B2	72.51	0.84	93.25	1.34	126.00	1230.57	FRP rupture	99.3	1.34
B3	73.84	0.88	99.23	1.51	120.00	1068.53	FRP rupture	110.2	1.38
B4	73.86	0.88	106.32	1.69	112.00	3327.14	FRP rupture	102.7	1.35

Figure 2.27 shows plate-to-concrete interface shear stresses at the plate ends calculated using Hassan and Rizkalla's model for different applied loads. The failure

criterion given by Equation 2.41 for the specimen's lowest concrete strength reported by the authors gives an interface shear stress of 3.4 MPa, which is why the predicted failure mode given by the model is FRP rupture for all three specimens, as they would clearly exceed any FRP rupture load before reaching the debonding shear stress.

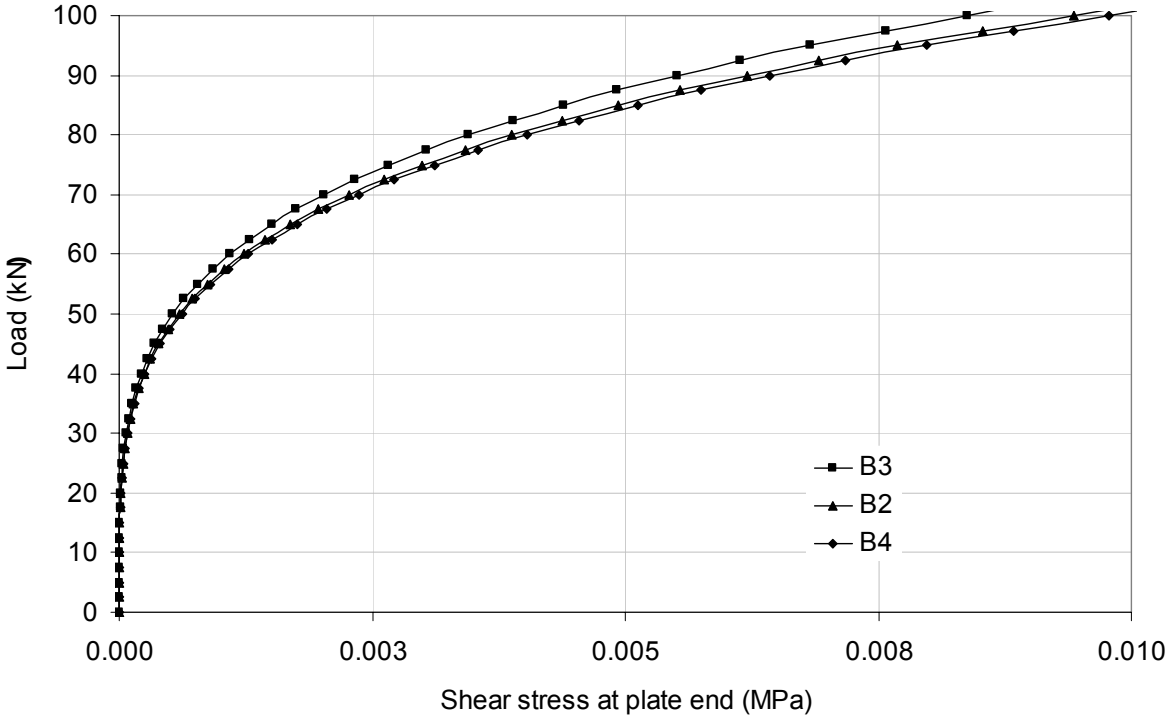

Figure 2.27. Plate-end shear stresses given by Hassan and RIzkalla's model for El-Hacha and Rizkalla (2004) specimens

The equal axial stiffness of the FRP strips used for all three specimens is reflected in the similar theoretical results obtained for the different beams for the three debonding mechanisms, with the exception of the PE debonding load for beam B4, for which equation 2.36 produced a higher debonding moment due to the considerable lower modulus of elasticity of the GFRP used for its strengthening.

As all plates were ended very close to the supports and hence on a low moment region, PE debonding was unlikely on these specimens, as reflected by the high theoretical debonding loads in Table 2.4.

2.6.3. Barros and Fortes

Barros and Fortes (2005) tested eight 1.5 m span rectangular beams of varying cross section and reinforced with 1.45x10 mm CFRP strips bonded into 4x12 mm grooves as shown in Figure 2.28, four of which were tested without CFRP strengthening for reference. The strengthened length of 1.4 m was kept constant.

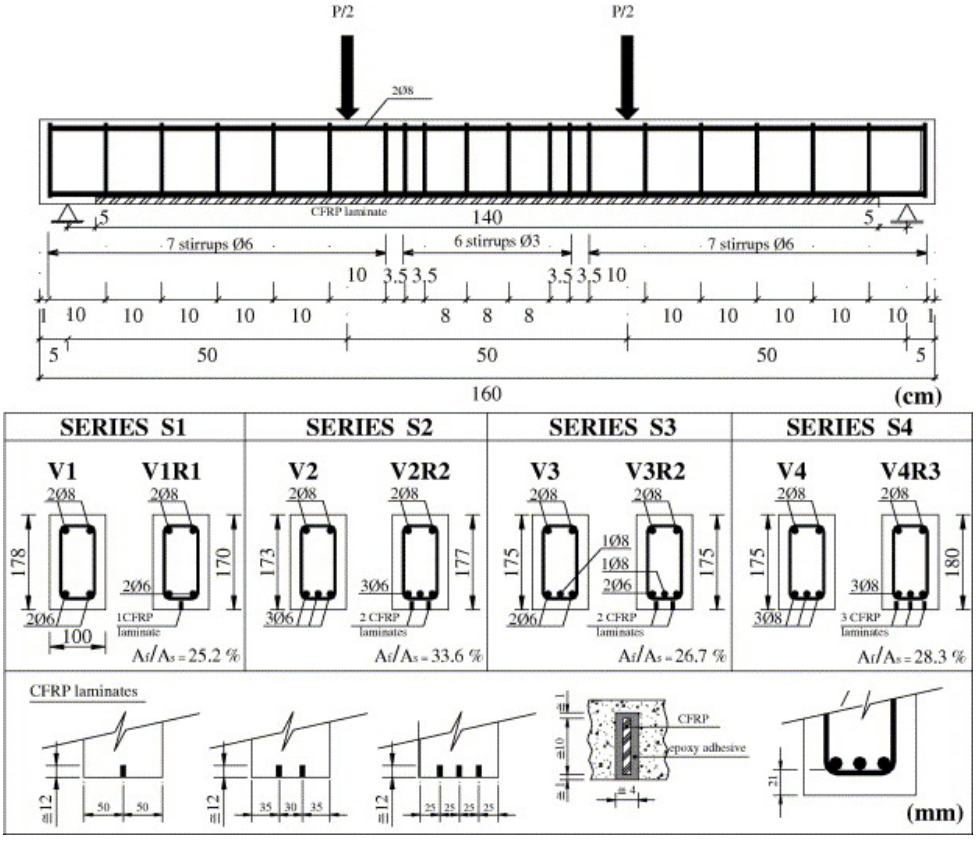

Figure 2.28. Specimen details and test set-up (Barros and Fortes, 2005)

Table 2.5. Barros and Fortes test results

Beam	Strengthened length (mm)	Failure load (kN)	Failure strain in FRP (%)	Failure mechanism
S1	1500	50.3	1.55	The test was stopped at deflection 27mm, at which point flexural cracks had developed, which suggests initiation of IC debonding.
S2	1500	78.5	1.28	Concrete layer detachment along entire strip and large shear cracks suggests CDC debonding.
S3	1500	81.9	1.28	Concrete layer detachment at quarter span and near midspan suggests IC and CDC debonding.
S4	1500	94.9	1.06	Same as for S2.

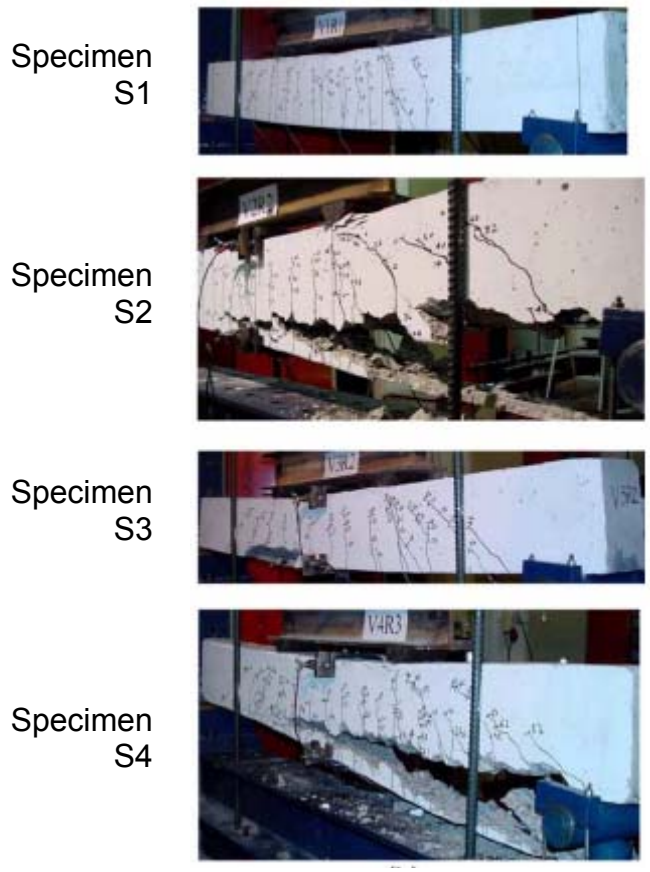

Figure 2.29. Strengthened beams after failure (Barros and Fortes, 2005)

Table 2.5 shows ultimate debonding failure loads and strains in the CFRP strip measured by Barros and Fortes, as well as a description of the failure mechanism obtained mainly from inspection of photographs of the strengthened specimens after failure shown in Figure 2.29, as the description of the debonding mechanism given by the authors was very limited.

Table 2.6 shows experimentally measured failure loads and strains, and theoretical debonding loads calculated using the different models. The shaded values indicate the lowest failure load calculated for each specimen and hence the predicted mode of failure. As for El-Hacha and Rizkalla's results, the IC debonding capacity has been calculated for the two different failure plane assumptions, and also in this case the individual strip failure planes assumption produced higher strains and loads. However the higher debonding loads did not mean a change of the theoretically predicted failure mechanism.

Table 2.6. Barros and Fortes test results analysis

Beam	Theoretical prediction							Experimental results	
	IC				CDC	PE	Hassan & Rizkalla model	Failure load (kN)	Failure strain in FRP (%)
	Common failure plane		Individual strip failure planes						
	Failure load (kN)	Failure strain (%)	Failure load (kN)	Failure strain (%)	Failure load (kN)	Failure load (kN)			
S1	42.81	1.40	42.81	1.40	53.00	122.25	57.50	50.30	1.55
S2	59.69	0.85	74.29	1.40	56.86	193.98	65.00	78.50	1.28
S3	66.85	0.85	78.83	1.40	58.00	217.40	67.50	81.90	1.28
S4	91.56	0.72	93.82	0.78	62.00	302.48	75.00	94.90	1.06

It can be seen from comparison with Table 2.5 that the predicted debonding mechanisms agreed with experimental observations, although there is some uncertainty about the experimental type of debonding, as the description of the failure mechanism provided by the authors was very limited.

It must be noted from the experimental results that as the number of strips increased the failure strain decreased. For IC debonding strength, this behavior is captured when the assumption of a common failure plane is made, but not when individual strip failure planes are assumed. For the later, failure strains remained constant as the dimensions of all grooves were the same. In the case of beam S4, the predicted debonding strain of 1.40% given by the model made achieving equilibrium through the layered analysis impossible, meaning the assumption of IC debonding was not correct, and that instead failure by concrete crushing would control. Hence a solution for the failure load was obtained using a simplified section analysis for the ultimate condition as specified by the ACI 318-05 code, using the equivalent concrete compression block for an ultimate strain of 0.003. From this analysis the strain in the NSM strip at failure was 0.78%, lower than the predicted IC debonding strain as it could be expected.

The underestimation of the CDC failure load may be due to the model used being developed for EB plates, which reach considerably smaller strains before debonding than NSM strips, and hence do not allow for any considerable force in the stirrups to be developed; in this case however, higher strains in the FRP were reached, which could have permitted some strain in the stirrups to develop and hence to contribute to the shear resistance.

Hassan and Rizkalla's model produced good approximations, although the debonding starting at the plate ends failure mechanism assumed by the model was not the failure mechanism observed experimentally.

As the strips were terminated very close to the beam supports in regions of very low moment, PE debonding was unlikely as reflected by the experimental results and the high predicted PE debonding loads.

2.6.4. Teng et al.

Teng et al. (2006) tested five 3.0 m span rectangular reinforced concrete beams, of which four were strengthened with two 2x16 mm CFRP strips bonded into 8x22 mm grooves cut in the tension concrete cover, while one was tested without strengthening for reference. The cross-sectional dimensions, reinforcement details and test set-up are shown in Figure 2.30. The two CFRP strips of each reinforced beam were bonded together with a 1 mm layer of adhesive to allow for the installation of strain gauges in between strips without interfering with the behavior of the strip-to-concrete interface, and hence the two bonded strips were treated as a single strip for analysis purposes. The strengthened length of the beam was the only variable in the tests. In specimens B2900, B1800, B1200 and B500 the strengthened lengths were 2900, 1800, 1200 and 500 mm respectively, located symmetrically about the beams' midspan.

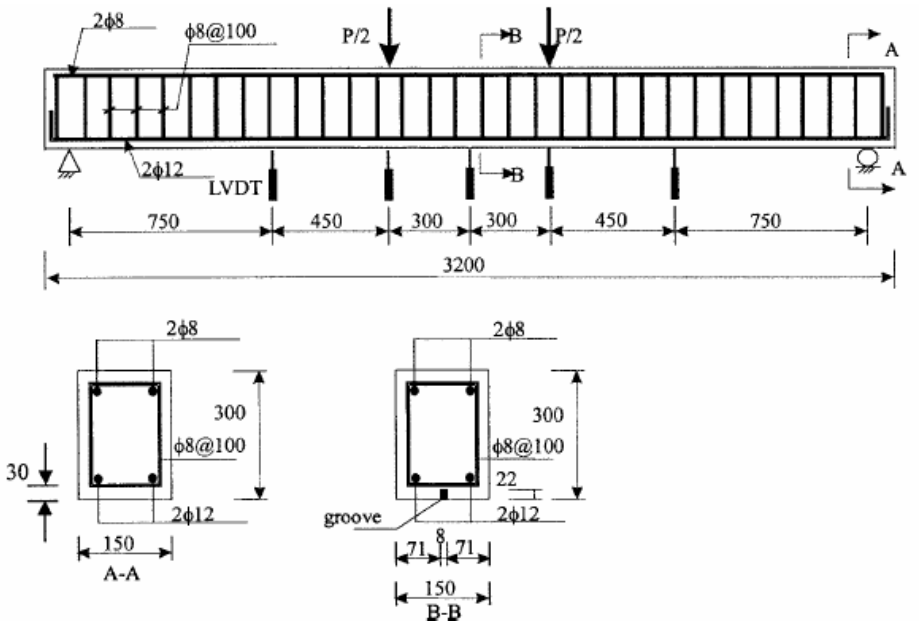

Figure 2.30. Typical specimen details and test set-up (Teng et al., 2006)

Table 2.7 shows measured ultimate debonding failure loads and strains in the CFRP strip, as well as the failure mechanism described by the authors.

Table 2.7. Teng et al. test results

Beam	Strengthened length (mm)	Failure load (kN)	Failure strain in FRP (%)	Failure mechanism
B2900	2900	99.8	0.97	Concrete crushing. IC debonding cracks and interaction with shear-flexural cracks were observed.
B1800	1800	91.7	0.73	Same as for B1200 except that the increased bonded length meant slip took place in between the steel and the concrete prior to failure.
B1200	1200	63.1	0.37	Concrete cover separation starting from the plate end. Initiated as PE cracks that later on joined flexural and shear-flexural cracks.
B500	500	47.8	0.23	Concrete cover separation starting at the plate end.
B0	Reference	48.4	-	Steel yielding followed by concrete crushing

Table 2.8 compares failure loads measured experimentally by Teng et al. (2006), and the theoretical predictions calculated using the different models presented in Section 2.5. The shaded values indicate the lowest failure load calculated for each specimen and hence the predicted mode of failure (without including predictions made using Hassan and Rizkalla's model).

By comparison with Table 2.7 it can be seen that the predicted modes of failure agreed with experimental observations, and that the unified IC debonding model provided a reasonable approximation to the IC debonding capacity, while the failure load for PE debonding was considerably underestimated. It must be noted however, that based on the observed experimental failure mechanism the strip debonding on beams B1800 and B1200 could have also been influenced by CDC debonding, which could have increased the difference between the theoretical PE debonding load and the experimental result.

Table 2.8. Teng et al. test results analysis

Beam	Theoretical prediction					Experimental results	
	IC		CDC	PE	Hassan & Rizkalla model (kN)	Failure load (kN)	Failure strain in FRP (%)
	Failure load (kN)	Failure strain (%)	Failure load (kN)	Failure load (kN)			
B2900	82.73	0.8303	94.00	712.52	230	99.8	0.9707
B1800	82.73	0.8303	84.00	59.38	20	91.7	0.7315
B1200	82.73	0.8303	84.00	39.58	12.5	63.1	0.3670
B500	78.27	0.7266	84.00	29.69	10	47.8	0.2296

The debonding loads calculated using Hassan and Rizkalla's model differ significantly from those measured experimentally for all specimens.

2.6.5. Kotynia

Kotynia (2006) tested five 4.2 m span beams of cross-section and reinforcement as shown in Figure 2.31. Beams A2 and B2 were strengthened with two 1.2x25 mm CFRP strips bonded into two 3.6x28 mm grooves cut in the tension concrete cover, while beams A4 and B4 were strengthened with four 1.2x25 mm CFRP strips bonded into two 6x28 mm grooves; two strips in each groove. Due to the shallower concrete cover of beams B2 and B4, it was necessary to cut the stirrups to install the CFRP on these two specimens. One beam was tested unreinforced for reference. The CFRP strips were terminated 75 mm short of the supports on all strengthened specimens.

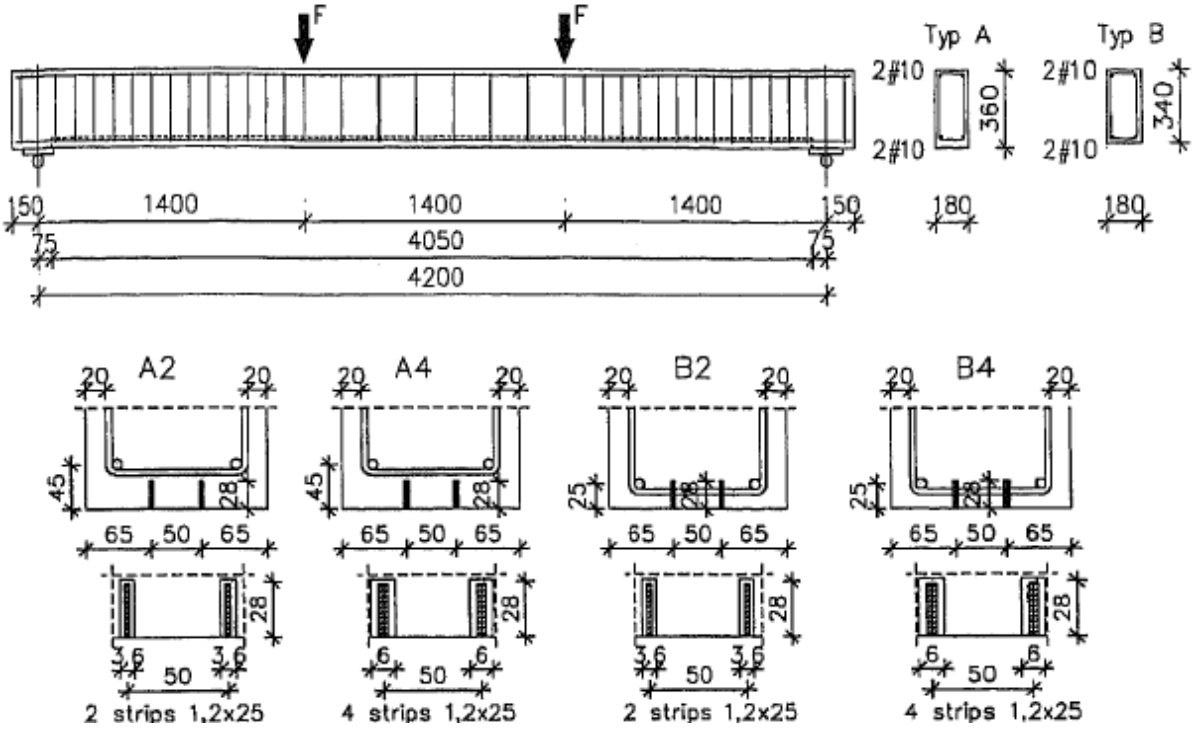

Figure 2.31. Test setup and specimen details (Kotynia, 2006)

Table 2.9 shows ultimate experimental loads and strains, as well as the failure mechanism described by the author. It can be seen that the beams strengthened with 4 FRP strips instead of 2 had a higher ultimate load, and that the variation in cross-section depth between specimens A and B, and the fact that stirrups had to be cut in specimens B had no effect on the failure load, which was attributed by the author to the effective depth of the tension rebar remaining the same in all specimens. The failure mechanism described by the author corresponds mainly to that of IC debonding, although the fact that flexural-shear cracks were observed indicates that the CDC debonding mechanism could have also contributed to the failure of the strengthened section.

Table 2.9. Kotynia test results

Beam	Strengthened length (mm)	Failure load (kN)	Failure strain in FRP (%)	Failure mechanism
A2	4050	96	Not given	Flexural cracks formed followed by cracking along the full length of the grooves. Shear-flexural cracks formed prior to debonding of the FRP along with all surrounding concrete below the rebar level
A4	4050	130	0.91	Same as for A2
B2	4050	96	1.37	Same as for A2
B4	4050	130	Not given	Same as for A2
Bnw	Reference	40.5	-	Steel yielding followed by concrete crushing

Table 2.10 shows ultimate measured loads and strains, and theoretical failure loads calculated using the different models available. Depending on the assumed failure plane, the theoretically predicted debonding mechanism could be IC or CDC

debonding, which is an acceptable outcome considering that signs of both IC and CDC debonding were observed experimentally. Both failure plane assumptions captured the fact that lower strains were achievable when more strips were used, but the individual failure planes assumption produced results closer to the experimental ones.

Table 2.10. Kotynia test results analysis

Beam	Theoretical prediction							Experimental results	
	IC				CDC	PE	Hassan & Rizkalla model	Failure load (kN)	Failure strain in FRP (%)
	Common failure plane		Individual strip failure planes						
	Failure load (kN)	Failure strain (%)	Failure load (kN)	Failure strain (%)	Failure load (kN)	Failure load (kN)			
A2	65.04	0.64	93.62	1.25	92.00	345.81	177.5	96.00	Not given
A4	76.77	0.45	110.22	0.82	94.00	431.86	177.5	130.00	0.91
B2	64.25	0.66	91.86	1.29	91.00	369.34	170.0	96.00	1.37
B4	75.08	0.46	106.96	0.83	92.00	443.91	167.5	130.00	Not given

Due to the FRP strips being terminated near the supports and hence in a low moment region, PE debonding was unlikely in these specimens, as reflected by the high calculated PE debonding loads in Table 2.10.

Hassan and Rizkalla's model over predicted the debonding loads, although by a lesser margin for the beams strengthened with 4 strips.

2.6.6. Barros et al.

Barros et al. (2007) carried out two series of tests, one for flexural strengthening and one for shear strengthening using both EB and NSM CFRP. The specimens for

flexural strengthening were designed to induce the occurrence of flexural failure before shear failure, and to maintain an equal tensile steel reinforcement axial stiffness to FRP axial stiffness ratio on all specimens. For the flexural tests, 24 specimens of dimensions and reinforcement as shown in Figure 2.32 were prepared (2 for each reinforcement configuration), out of which 12 were strengthened with EB strips and wet lay-up sheets, 6 were strengthened with NSM strips and 6 were tested unstrengthened for reference. The results and analyses presented here focus on the NSM flexural strengthened specimens.

Table 2.11 shows ultimate failure loads obtained as the average of two identical beams and the failure mechanisms as observed in Figure 2.33, as the failure mode for all three specimens was described by the authors simply as “yielding of the longitudinal steel reinforcement and delamination of the concrete cover”.

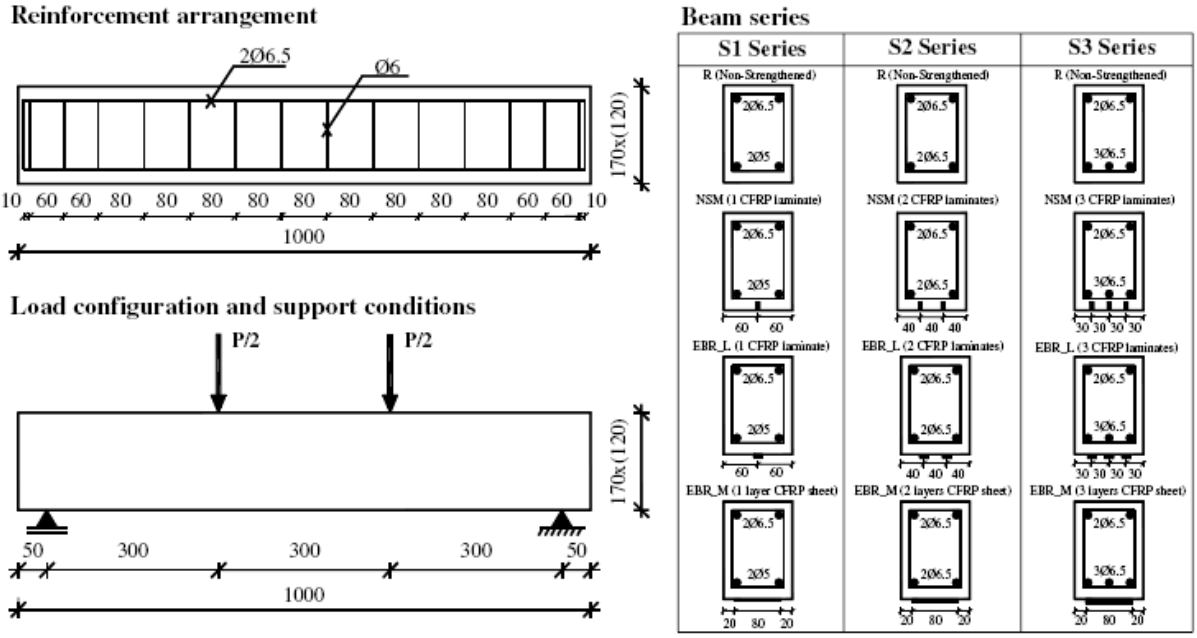

Figure 2.32. Flexural tests specimen details (Barros et. al., 2007)

Table 2.11. Barros et al. test results

Beam	Embedment length (mm)	Failure load (kN)	Failure mechanism
S1	800	79.9	IC debonding induced by flexural-shear cracking
S2	800	93.3	CDC debonding. Shear cracks reached the steel tension reinforcement level where they joined and propagated until reaching the plate end
S3	800	96.6	Same as for S2

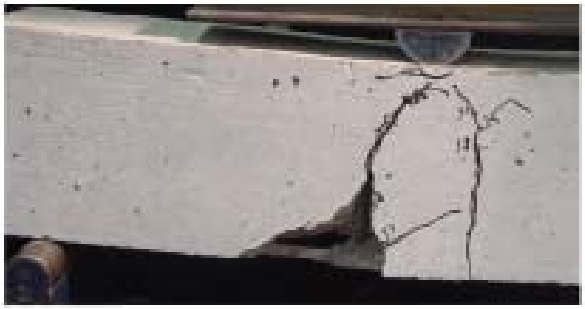

NSM with one laminate

NSM with two or three laminates

Figure 2.33. NSM strengthened specimens after failure (Barros et al., 2007)

Table 2.12 shows ultimate experimental failure loads and theoretical debonding loads calculated using the different models. For all beams the CDC debonding analysis as described in Section 2.5.2 indicated that due to the beams' short shear span relative to their depth, shear cracking was likely to occur beyond the plate end, and hence the CDC debonding resistance would be a function only of the concrete

shear capacity V_c, as illustrated in Figure 2.34, which did not occur experimentally. However, it may be taken into account that the theoretical solution estimated CDC to occur only 15mm beyond the plate end, and that the CDC debonding resistance based only in V_c gave failure loads of 74, 76 and 77kN for beams S1, S2 and S3 respectively, which is reasonable compared with the experimental ultimate load. For these reasons, although the theoretical model predicts CDC debonding not to occur, in Table 2.12 the CDC debonding loads predicted by the model are given, as due to the limited number of experimental results for CDC debonding, this will allow to make a better assessment of the model.

Table 2.12. Barros et al. test results analysis

Beam	Theoretical prediction							Experimental results
	IC				CDC	PE	Hassan & Rizkalla model	Failure load (kN)
	Common failure plane		Individual strip failure planes		Failure load (kN)	Failure load (kN)		
	Failure load (kN)	Failure strain (%)	Failure load (kN)	Failure strain (%)				
S1	63.78	1.52	63.78	1.52	74.00	103.79	67.5	79.9
S2	79.64	0.94	104.76	1.52	76.00	169.14	72.5	93.3
S3	107.62	0.79	148.68	1.52	77.00	237.34	77.5	96.6

Hassan and Rizkalla's model produced good approximations to the debonding loads for all three specimens. It must be considered however, that the failure loads shown in Table 2.12 have been calculated under the assumption of debonding occurring at the plate ends.

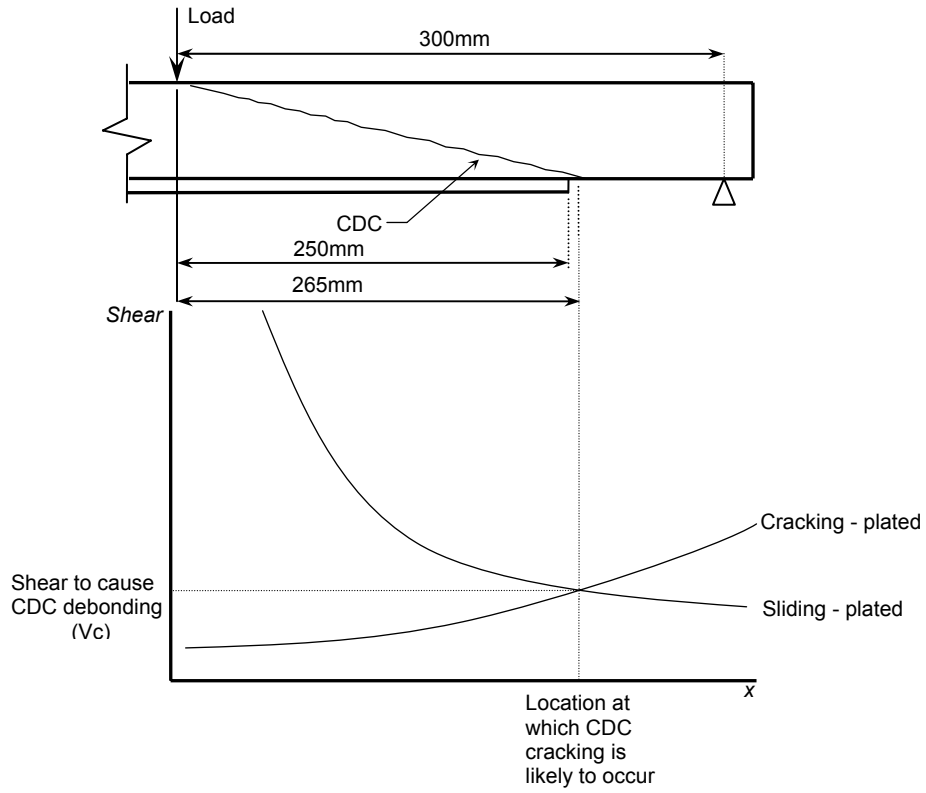

Figure 2.34. Sketch of CDC failure model for Barros et al. specimens

2.6.7. Conclusions

Table 2.13 summarizes all experimental failure loads presented for beams in bending strengthened with NSM FRP strips and their corresponding predicted theoretical failure loads calculated using the different analytical models. The results are grouped by predicted theoretical debonding mechanism, and as measure of the accuracy of the theoretical prediction the ratio of the theoretical prediction over the experimental result is given for each specimen, meaning a ratio lower than zero indicates a conservative prediction of the debonding strength. The average theoretical/experimental result ratio is given for each predicted debonding

mechanism and hence for each debonding model. The right-hand side of Table 2.13 also gives theoretical/experimental ratios for individual specimens and average ratios for each debonding mechanism, for failure loads calculated using Hassan and Rizkalla's model. Table 2.13 also gives standard deviations of the theoretical/experimental ratios for each analytical model, as a measure of the consistency with which the models predict the results.

2.6.7.1. Seracino et al.'s Unified IC Debonding Model

It is evident in Table 2.13 that when applying the unified IC debonding model proposed by Seracino et al., the assumption of individual failure planes produced results much closer to the experimental results than the assumption of a common failure plane. As a general rule, it is suggested that when the spacing between adjacent grooves is greater than 2.5 times the width of the grooves, then the FRP strips will fail individually (Standards Australia, HB305-200X (200X)), which supports the assumption of individual failure planes, as the groove spacing of all the specimens presented here falls within this category. However it must be considered that for one specimen the failure load was overestimated and that the decrease in the maximum debonding strain as the number of strips used increased observed in some experiments, was not captured by the individual failure planes assumption. When the assumption of all strips failing together is made, the contribution to the stiffness of the volume of concrete included in the failure plane is not taken into account, hence it is felt that if this effect is included in the model, the common failure plane approach would produce better results.

Table 2.13. Summary of experimental and theoretical failure loads for NSM FRP strengthened beams in bending

Debonding Mechanism	Author (s)	Specimen	Experimental failure load (kN)	Common failure plane				Individual failure planes				Hassan and Rizkalla's model			
				Theoretical failure load (kN)	Theo/Exp	Average Theo/Exp	Std Dev	Theoretical failure load (kN)	Theo/Exp	Average Theo/Exp	Std Dev	Theoretical failure load (kN)	Theo/Exp	Average Theo/Exp	Std Dev
IC debonding	1	B8	80.00	66.08	0.83	0.76	0.10	66.08	0.83	0.88	0.07	Rupture	-	1.19	0.39
		B7	80.00	66.08	0.83			66.08	0.83			Rupture	-		
		B6	75.00	66.08	0.88			66.08	0.88			Rupture	-		
		B5	79.00	66.08	0.84			66.08	0.84			70.00	0.89		
		B4	74.00	66.08	0.89			66.08	0.89			55.00	0.74		
	2	B2	99.30	72.51	0.73			93.25	0.94			Rupture	-		
		B3	110.20	73.84	0.67			99.23	0.90			Rupture	-		
		B4	102.70	73.86	0.72			106.32	1.04			Rupture	-		
	3	S1	50.30	42.81	0.85			42.81	0.85			55.00	1.09		
	4	B2900	99.80	82.73	0.83			82.73	0.83			Rupture	-		
	5	A2	96.00	65.04	0.68			93.62	0.98			170.00	1.77		
		A4	130.00	76.77	0.59			110.22	0.85			167.50	1.29		
		B2	96.00	64.25	0.67			91.86	0.96			165.00	1.72		
		B4	130.00	75.08	0.58			106.96	0.82			160.00	1.23		
	6	S1	79.90	63.78	0.80			63.78	0.80			65.00	0.81		
				Theo. failure load (kN)		Theo/Exp		Average Theo/Exp		Std Dev					
CDC debonding	3	S2	78.50	56.86		0.72		0.74		0.07		62.50	0.80	0.77	0.02
		S3	81.90	58.00		0.71						62.50	0.76		
		S4	94.90	62.00		0.65						72.50	0.76		
	6	S2	93.30	76.00		0.81						70.00	0.75		
		S3	96.60	77.00		0.80						75.00	0.78		
PE debonding	1	B3	60.00	54.16		0.90		0.71		0.11		37.50	0.63	0.37	0.19
		B2	54.00	40.62		0.75						27.50	0.51		
		B1	53.00	36.93		0.70						25.00	0.47		
	4	B1800	91.70	59.38		0.65						20.00	0.22		
		B1200	63.10	39.58		0.63						12.50	0.20		
		B500	47.80	29.69		0.62						10.00	0.21		

Author (s) key: 1- Hassan and Rizkalla (2003)
2- El-Hacha and Rizkalla (2004)
3- Barros and Fortes (2005)
4- Teng et al. (2006)
5- Kotynia (2006)
6- Barros et al. (2007)

As mentioned before, the overall underestimation of the IC debonding capacity produced by the model is also influenced by the fact that the model was developed based on push-pull tests, which have been proven to be a lower bound to the IC debonding resistance of bonded FRP in beams.

2.6.7.2. CDC Debonding Model

It can be seen in Table 2.13 that the CDC debonding model given in Oehlers and Seracino (2004) produced very consistent results, although the debonding loads were always underestimated. As mentioned before, this may be due to the model used being developed for EB plates, which debond at low strains, hence not allowing for the development of strain in the stirrups. NSM strips on the other hand, debond at higher strains, meaning that significant strain may be developed in the stirrups before debonding of the strip, and hence an increment in the resistance of the strengthened section from the stirrups.

In regards to this effect, Bensen et al. (2005) proposed that the portion of the CDC debonding strength not captured by Oehlers and Seracino's model could be estimated as a fraction of the total strength that can be developed by the stirrups using the expression

$$V_{\exp} = V_c + \Delta V_c + kV_s \tag{2.43}$$

where V_{exp} is the experimental CDC debonding shear, V_c is the shear capacity of the concrete section alone, ΔV_c is the increment in CDC shear debonding due to the

FRP strip (difference between the plated and the unplated CDC debonding shear as described in Section 2.5.2), V_s is the shear strength from the stirrups, and k is the fraction of the stirrup shear strength developed. Based on the application of this analysis to the experimental results of Barros and Fortes' beams S2 through S4, and using the Australian concrete design code AS 3600-2001 to calculate V_c and V_s, the average fraction of stirrup strength that would have been developed at failure was found to be 0.40.

Application of the same analysis to the five specimens failing by CDC debonding in Table 2.13, using ACI 318-05 to calculate V_c and V_s, yielded the results shown in Table 2.14. ΔV_c is given a zero for Barros et al.'s specimens due to the CDC debonding model predicting failure beyond the end of the strip, meaning no shear capacity enhancement would be produced by the FRP, as discussed in Section 2.6.6. It can be seen that a similar average fraction of stirrup shear as that estimated by Bensen et al. was calculated for these five beams.

It can be concluded that, subject to confirmation as more experimental results become available, the increased CDC debonding strength of NSM retrofitted beams due to strain development in the stirrups, could be calculated as a constant fraction of the shear strength of the stirrups. Based on the results of Table 2.14, this fraction could conservatively be taken as 0.3 (the minimum of the five results). It is recommended that to further understand this mechanism, tests are carried out with strain-gauged stirrups, and the amount of longitudinal flexural reinforcement be carefully estimated to ensure critical diagonal cracks reach the tension face of the

beam and hence the NSM FRP, instead of propagating along the steel reinforcement level.

Table 2.14. Estimated fraction of stirrup shear developed in beams failing by CDC debonding

Authors	Specimen	V_{exp} (kN)	V_c (kN)	ΔV_c (kN)	V_s (kN)	k	k average
Barros and Fortes	S2	39.25	17.25	1.50	63.16	0.33	0.43
	S3	40.95	17.03	1.50	62.34	0.36	
	S4	47.45	17.48	1.50	63.99	0.45	
Barros et al.	S2	46.65	21.00	0.00	55.63	0.46	
	S3	48.30	21.00	0.00	55.63	0.49	

2.6.7.3. Oehlers and Nguyen's Modified PE Debonding Model

Few specimens failed by PE debonding, as most experimental programs used simply supported beams with FRP strips that ended very near the supports, making PE debonding unlikely. From the available results it can be seen that, with the exception of Hassan and Rizkalla's specimen B3, which may have failed by a combination of IC and PE debonding, theoretical debonding loads calculated using Oehlers model taking into account the double bonded surface of NSM strips produced failure loads considerably below the experimental ones. This indicates that the approach taken of using an EB debonding model allowing for an increase in the capacity based only on the greater bonded area of the NSM strips is too conservative.

2.6.7.4. Hassan and Rizkalla's Model

Hassan and Rizkalla's model produced adequate results for beams failing by CDC debonding, while for beams failing by IC debonding several of the calculated loads were significantly overestimated. It must be noted that all debonding loads have been calculated using $x = 0$, as this value yields the lowest and hence first to occur debonding load. This implies that according to the model debonding is being predicted to take place at the strip end, which is not what occurs when CDC or IC debonding mechanisms govern.

From analysis of the limited available experimental results for beams failing due to PE debonding, it was observed that the results yielded by Hassan and Rizkalla's model differed considerably from the experimental results.

2.6.7.5. Other Considerations

The influence on the ultimate load capacity of NSM strengthened beams of factors such as the amount of tension steel reinforcement and FRP reinforcement in the cross-section and the distance between adjacent FRP strips when more than one groove are used, were also considered by Barros et al. (2007). Available results indicate that as the amount of either rebar or FRP increases, the achievable strains in the FRP decrease, and hence the strengthening is less efficient, even though higher amounts of strengthening generally lead to higher ultimate loads. It appears that high quantities of reinforcement concentrated near the tension face of the section induce high stress concentrations in the area and the formation of a plane of weakness in between the rebar and the NSM FRP, as photographs of beams after

failure often suggest. It is felt that these are important factors in the ultimate behavior of NSM strengthened beams which are not yet fully understood, however due to the additional complexity of the problem the influence of these variables will not be given any further consideration in this research thesis.

It follows from the analysis in this Chapter that although the available models to predict IC and CDC debonding of beams in bending strengthened with NSM strips still need further development to deliver more accurate results, in general they already yield good conservative approximations and capture the behavior of the debonding mechanisms observed experimentally. The same is not true for the PE debonding models considered, as failure loads calculated using the modified Oehlers model and Hassan and Rizkalla's model produced values considerably below the experimental ones, which indicates that better understanding of this debonding mechanism is still required to enable the formulation of a model that yields a better prediction of the plate-end debonding resistance of NSM strips.

With the aim of better understanding the PE debonding mechanism, the 3D finite element analyses of beams strengthened with NSM FRP strips presented in Chapter 3 were carried out. The main focus was to investigate the complex 3D state of stress near the NSM strips' cut off points, work which to the author's knowledge has not been published before. The outcome of these analyses was expected to give important clues towards the formulation of a rational model to predict the PE debonding resistance of NSM strips in concrete beams.

3. Development and Validation of Finite Element Models

With the aim of gaining a better understanding of the distribution of stresses at the ends of NSM FRP plates that could aid the formulation of an analytical model to predict plate-end debonding, specimens tested by Teng et al. and Hassan and Rizkalla were modeled in 3D using the finite element analysis software ANSYS.

3.1. Modeling

All specimens tested by Teng et al. and specimens B0, B2 and B3 tested by Hassan and Rizkalla were modeled. Figure 3.1 shows details of the Teng et al. specimens modeled and Figure 3.2 shows details of the Hassan and Rizkalla specimens modeled.

Both the geometry and the materials comprising the specimens were modeled accurately, including FRP strips, epoxy adhesive, longitudinal steel reinforcement and concrete. The ANSYS library of elements has one 8-noded hexahedral isoparametric element “Solid 65”, specifically developed to model reinforced concrete and brittle materials, which was used to model the concrete and the epoxy adhesive, and a compatible element (same number of nodes, degrees of freedom and shape functions) “Solid 45”, that allows for the modeling of orthotropic materials, which was used to model the FRP strips.

The “Solid 65” element allows for the modeling of the nonlinear behavior of concrete based on a constitutive model developed by Williams and Warnke (1975), which is a function of the principal stress state. Cracking of the concrete under

tension is modeled through a “smeared” crack analogy and the possibility of crushing in compression is accounted for using a plasticity algorithm. The element behavior is linear elastic until any of the principal stresses at any of the element’s eight integration points exceeds the specified tensile or compressive strengths. Cracked or crushed regions are formed perpendicular to the relevant principal stress direction and stresses are redistributed locally. When cracking occurs, it is modeled through an adjustment of the material properties which introduces a plane of weakness in the element. The amount of shear transfer across a crack can be varied by means of coefficients defined by the user ranging from 1.0 for full shear transfer (a rough crack) to 0.0 for no shear transfer (a perfectly smooth crack). If the material fails at an integration point in uniaxial, biaxial or triaxial compression, it is assumed to have crushed at that point, which is treated as a complete deterioration of the structural integrity of the material, and hence the contribution to the stiffness of the element at that integration point is ignored. Subsequently, second and third mutually orthogonal cracks can develop at each integration point.

The longitudinal steel reinforcement was modeled using a feature of the “Solid 65” concrete elements that simulates reinforcement behavior by modifying their stiffness based on given reinforcement material properties, the bar orientation and a ratio of the volume of reinforcement to the volume of concrete in each reinforced element. The reinforcement is then considered to be “smeared” throughout elements and it is capable of tension, compression, plastic deformation and creep.

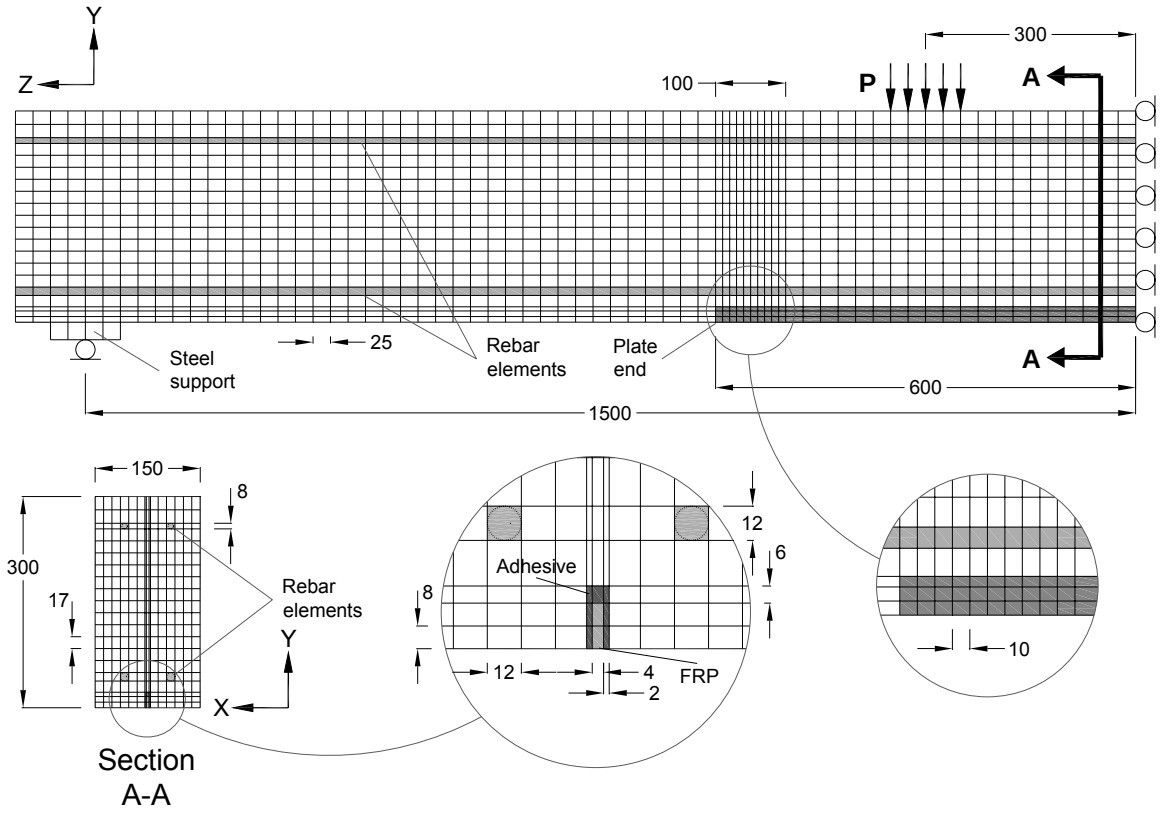

Figure 3.1. Typical finite element model of Teng et al.'s specimens (dimensions in mm)

The "Solid 65" element was also considered appropriate to model the epoxy adhesive layer, as it is capable of simulating the behavior of a brittle material. Crushing of the epoxy adhesive under compression was considered to be of little importance in the behavior of the strengthened beams, and hence the crushing capability was disabled in the adhesive elements. This approach would allow studying stresses at the interface in three dimensions and would not force the interface to behave following a specified bond-slip model. CFRP-adhesive interfaces have accurately been modeled using ANSYS "Solid 65" and "Solid 45" elements for the adhesive and CFRP respectively by Dawood et al. (2007).

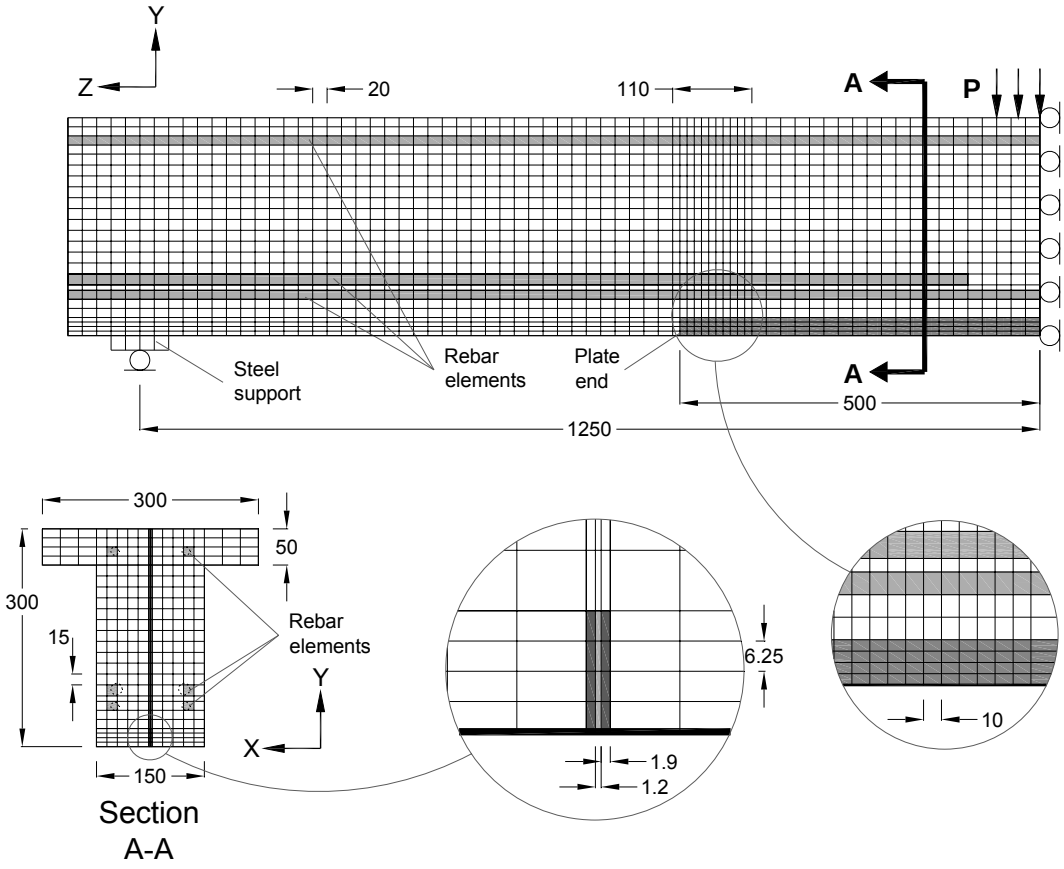

Figure 3.2. Typical finite element model of Hassan and Rizkalla's specimens (dimensions in mm)

Input for the "Solid 65" elements includes the material's modulus of elasticity, Poisson's ratio, the tensile and compressive strengths, as well as coefficients of shear transfer across cracks. The concrete compressive strength and linear elastic reinforcement steel properties in Table 3.1 are the values reported by the authors, as well as the adhesive properties for Teng et al.'s specimens; the adhesive properties used for Hassan and Rizkalla's specimens were the same as those of Teng at al.'s specimens, as the actual ones were unavailable. The calculated moduli of elasticity of concrete are also given in Table 3.1. The assumed coefficients of

shear transfer across open and closed cracks in concrete were 0.6 and 0.85 respectively, and 0.01 and 0.02 for epoxy adhesive, respectively. These values were chosen to reflect the fact that higher stress transfer across a crack can occur in concrete due to aggregate interlock than in epoxy adhesive, and that when cracks are closed higher shear transfer can be expected to occur.

In addition to linear elastic properties, the stress-strain curve of the steel reinforcement was also specified. Typical mild steel stress-strain curves as shown in Figure 3.3 were assigned.

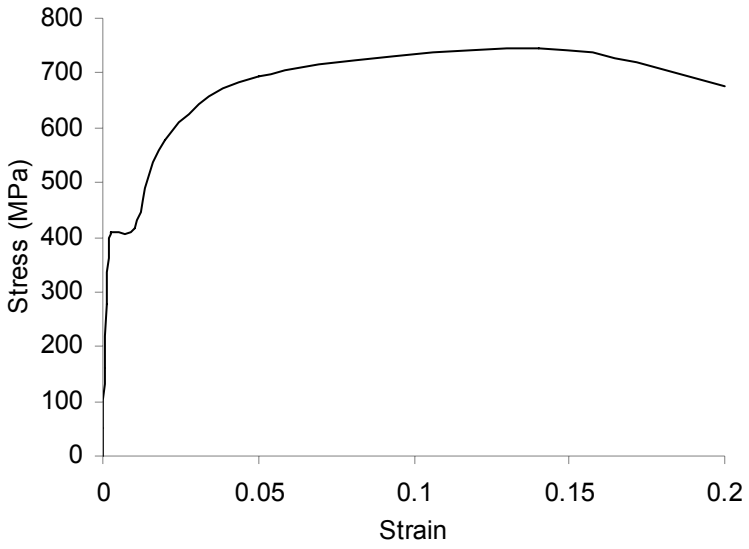

Figure 3.3. Stress-strain curve assumed for steel reinforcement

The “Solid 45” elements allow for plasticity, creep, swelling, stress stiffening, large deflection and large strain behavior, and were given the appropriate FRP orthotropic material properties. The moduli of elasticity reported by the authors given in Table 3.1 were used as the moduli of elasticity in the direction of the fibers,

designated E_Z as it corresponds to the Z axis in Figure 3.4. From these values, and assuming typical Young's moduli for the matrix (E_m) and the fibers (E_f) as shown in Table 3.1, the fiber fraction V_f was calculated from $E_Z=E_fV_f+E_m(1-V_f)$, and subsequently the matrix fraction determined as $V_m=1-V_f$. The E_m and E_f values in Table 3.1 were chosen to obtain typical V_f values between 0.4 and 0.7. From this the Young's modulus perpendicular to the fibers E_X and E_Y (which are equal) were calculated from $(1/E_Y$ or $1/E_X)=(V_f/E_f)+(V_m/E_m)$. ν_{XY} was assumed a typical value of 0.3, while ν_{YZ} and ν_{XZ} were calculated proportionally to the Young's modulus ratio E_Y/E_Z for each specimen set. The shear moduli in the three orthogonal directions were calculated from $G=(E/2(1+\nu))$ using the appropriate Young's moduli and Poisson's ratios.

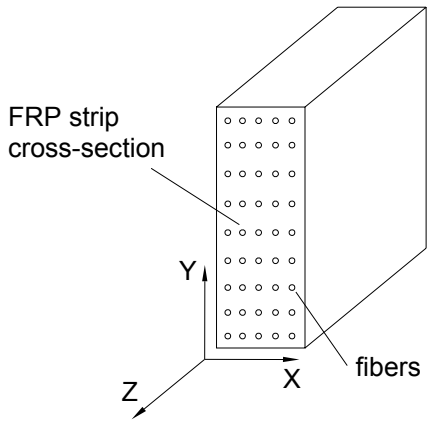

Figure 3.4. FRP material properties reference axes

Taking advantage of symmetry only half beams were modeled using the appropriate degree of freedom restraints. For all specimens a finer mesh was produced around the FRP plate end as this was the main area of interest, while a coarser mesh was used elsewhere to help reduce computational time. However, the

level of detail with which the FRP and adhesive were modeled meant the transition to a coarser mesh was limited by the need to maintain acceptable aspect ratios and to use hexahedral elements throughout. The cross-sectional mesh was kept constant throughout the beams to facilitate the modeling of specimens strengthened with FRP strips of different lengths.

Table 3.1. Material properties used in finite element modeling

Specimen set		Teng et al.	Hassan and Rizkalla
Concrete	f'_c	35	57
	f_{ct}	3.13	4.00
	E_c	28000	30000
	υ	0.3	0.3
Steel reinforcement	f_y	532	400
	E_s	210000	200000
	υ	0.3	0.3
FRP	f_u	2068	2000
	E_Z	151000	160000
	E_f	220000*	230000*
	E_m	3000*	3000*
	E_X	9165.9	9433.6
	E_Y	9165.9	9433.6
	υ_{XY}	0.3	0.3
	υ_{XZ}	0.018	0.018
	υ_{YZ}	0.018	0.018
	G_{XY}	58076.9	61538.5
	G_{XZ}	4501.9	4633.4
	G_{YZ}	4501.9	4633.4
Adhesive	f_t	42.6	42.6*
	E_a	2620	2620*
	υ	0.3	0.3

All units MPa

To avoid undesirable high stress concentrations on concrete elements, metal plates were added at the beams supports and the loads were applied as pressures on several elements rather than concentrated loads at nodes.

As nonlinear behavior was being modeled for the concrete and adhesive, an iterative solution was necessary, as well as an incremental application of the load to avoid convergence problems. The models were not calibrated to match experimental results, only the most appropriate criteria to obtain results as accurate and reliable as possible within the capabilities of the software were used.

3.2. Results

Figures 3.5 and 3.6 show the experimental and finite element analysis load-deflection response of the modeled specimens. In general it can be seen that first cracking of the concrete and the initiation of yielding of the steel were modeled accurately, except in Teng et al. specimens B1800 and B2900, where yield of the steel occurred experimentally at higher loads. Within the specimens corresponding to a same experimental program, the only differences in the finite element models are the length of the FRP strip and for the reference specimens, the absence of FRP. Then it can be seen that the finite element models were able to capture the strengthening effect of the FRP strips, and were sensitive to change in the length of the FRP, as specimens with longer strips showed decreased deflections for a given load level.

The ultimate detachment of the FRP strips, indicated in Teng et al.'s specimens by the descending branches in the load-deflection response, was not captured by

the finite element models, in which the stiffness of the beams keeps steadily decreasing due to crack propagation in the concrete and adhesive, but never drops suddenly to a negative stiffness as recorded experimentally. This also explains the considerably different load-deflection response obtained for Hassan and Rizkalla's specimen B2, which experimentally behaved essentially as an unstrengthened beam, meaning complete debonding of the FRP occurred at a very low load. Similar results were obtained by Barbosa and Ribeiro (1998) when modeling 3D FRP-strengthened beams in ANSYS. Due to this, a limiting criterion of strain in the concrete of 0.003 was set to define the maximum loads of the finite element results as shown in Figures 3.5 and 3.6.

As can be expected, this behavior at ultimate load is very complex and difficult to model in a highly heterogeneous material as concrete. Nonetheless, the aim of the finite element analysis in this investigation is not to obtain a model that can necessarily accurately predict ultimate capacities of strengthened beams, but to serve as a tool to help understand the distribution of stresses near the ends of near-surface mounted FRP strips, and possibly yield clues on the plate-end debonding mechanism that can aid the formulation of an analytical model. Bearing the above in mind, the results obtained were deemed appropriate and reliable enough to study the stress distribution near the strips' cut off points.

Based on the theoretical debonding models assessed in the literature review, and with the aid of the finite element analyses, an analytical model to predict plate-end debonding of near-surface mounted FRP strips in concrete flexural members was formulated, the derivation of which is the subject of the following Chapter.

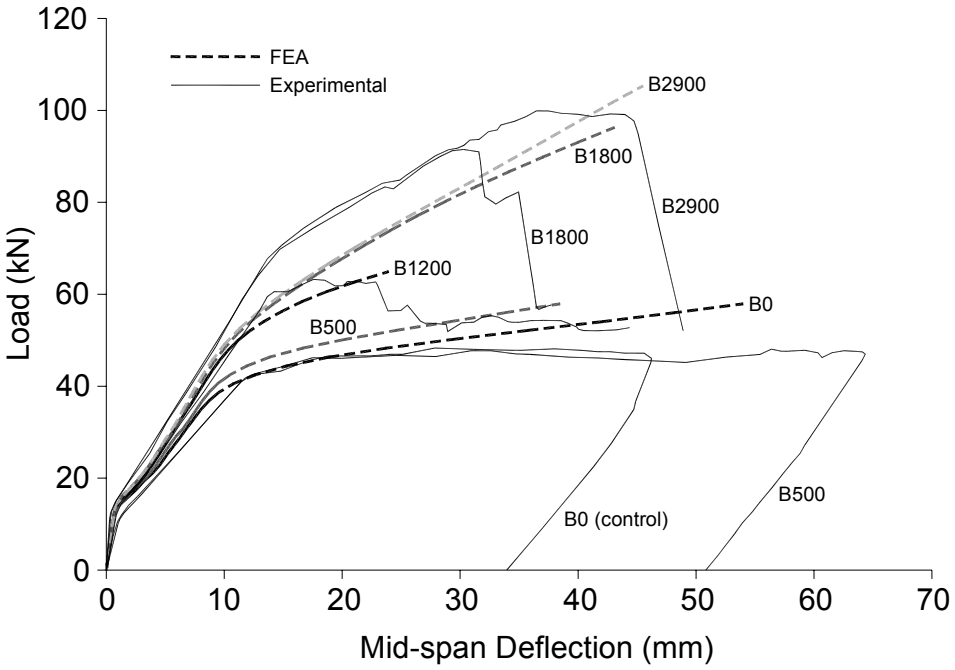

Figure 3.5. Load-deflection response for Teng et al.'s specimens

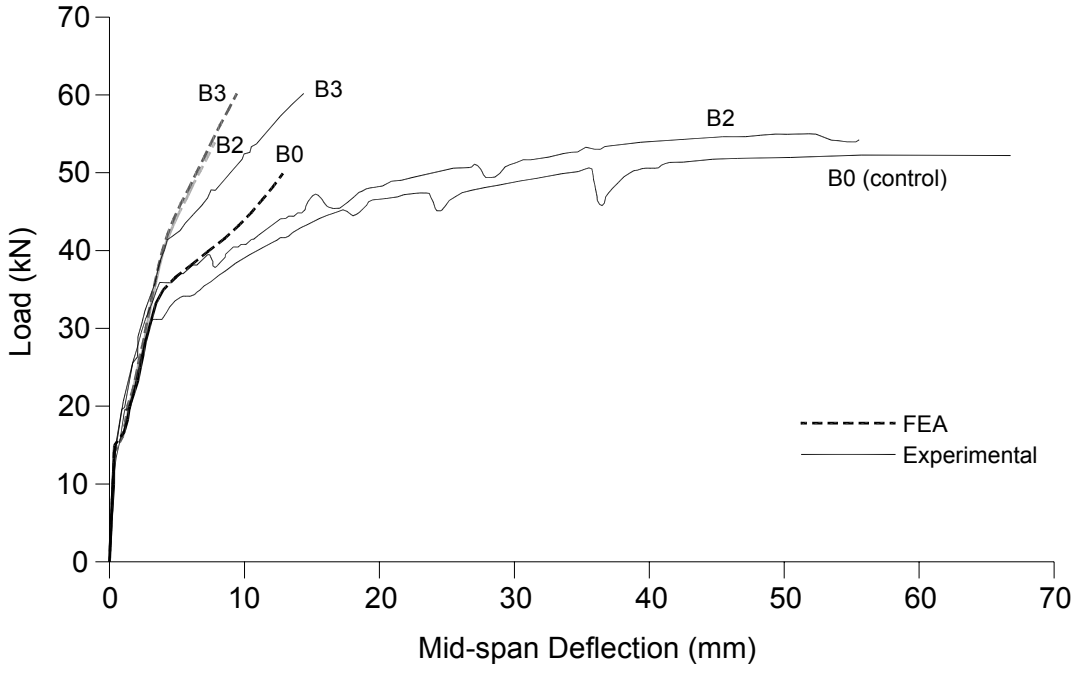

Figure 3.6. Load-deflection response for modeled Hassan and Rizkalla's specimens

4. Development and Assessment of Proposed Model

Based on the literature review presented in Chapter 2 and using the finite element models described in Chapter 3, an analytical model for the PE debonding resistance of a NSM strengthened section was developed.

The PE debonding resistance is considered to be a function of the stresses that develop near the ends of a NSM strip and of the strength of the concrete, given that debonding failures in properly bonded FRP invariably occur in the concrete adjacent to the adhesive layer. Hence the stresses in the concrete near the cut-off points of the strip need to be quantified and related to a failure criterion to establish the limit of the debonding resistance.

On an NSM strengthened concrete flexural element, from mechanics six different stresses can develop at a point in the concrete adjacent to the adhesive layer near the ends of a strip, as shown in Figure 4.1.

Considering that for PE debonding to take place high moments must exist at the strip ends, concrete can be expected to be cracked as shown in Figure 4.1. Hence, the magnitude of normal stress σ_{ZZ} can be expected to be small, and for this reason σ_{ZZ} will be disregarded in the model formulation.

Figure 4.1 also shows the shear stress distribution for a section in bending. This shear stress corresponds to τ_{YZ}, which can then be expected to be small, considering NSM strips are very close to the tension face of the section, where the shear stress approaches zero. Further, due also to the strip being located very close

to the tension face of the beam, the magnitude of normal stress σ_{YY} can be expected to be negligible.

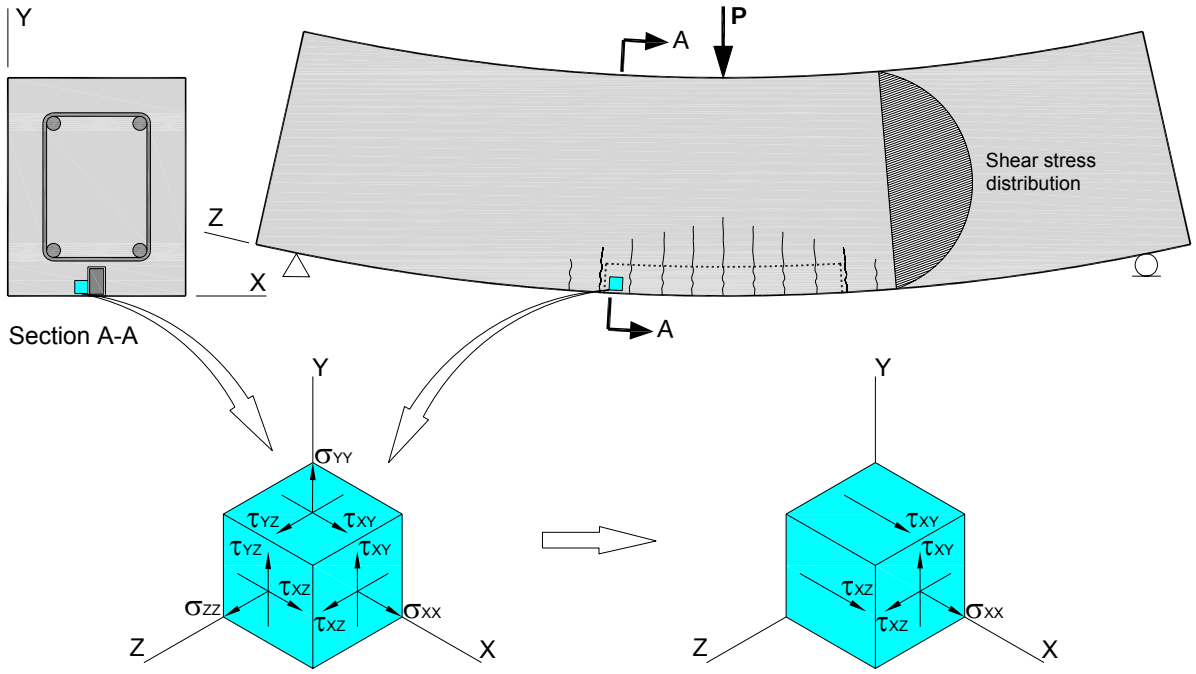

Figure 4.1. Stresses in concrete adjacent to the adhesive layer near the strip ends of an NSM strip considered in the proposed model formulation

Using finite element analyses, the magnitudes of stresses τ_{XZ}, τ_{XY} and σ_{XX} at the strip ends were compared up to the load at which the shorter plates debonded experimentally, both for Hassan and Rizkalla and Teng et al.'s specimens, as shown in Figure 4.2. It can be seen that the relative magnitude of none of the three stresses is consistently small enough for any of them to be neglected. Note that in Figure 4.2 the change of sign of the stress is only relevant for σ_{XX}, as a positive value indicates tensile stress, while a negative one indicates a compressive stress.

These considerations leave three stresses, τ_{XZ}, τ_{XY} and σ_{XX} to be included in the modeling of the PE debonding mechanism. The individual stresses must then be quantified before combining them, and finally compared with a failure criterion.

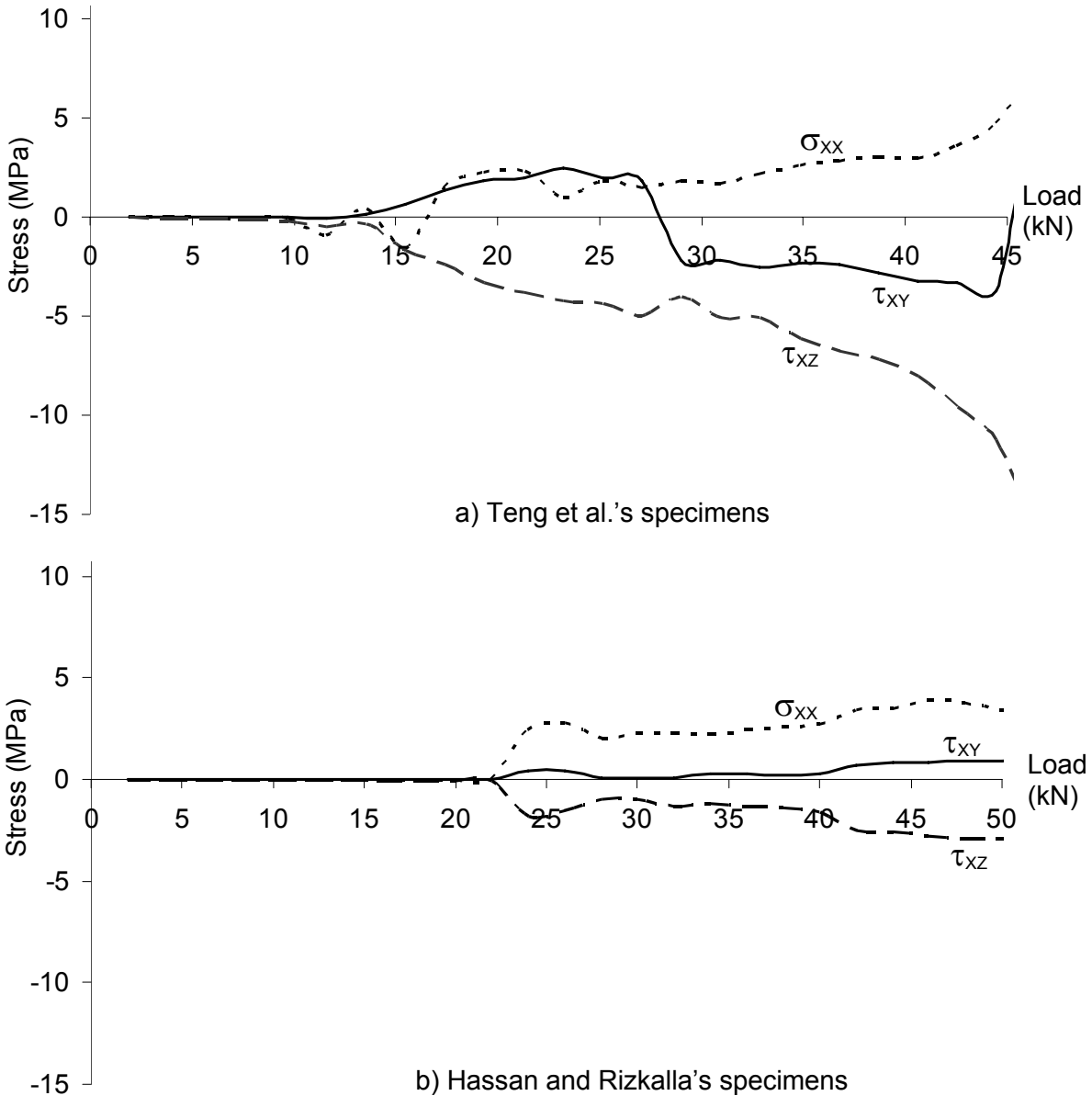

Figure 4.2. Typical relative magnitude of strip-end stresses for different load levels

4.1. Transverse Shear Stress τ_{XY}

In Oehlers and Nguyen's PE debonding model for EB side plates presented in Section 2.5.3.1, the transverse shear stress τ_{XY} was assumed to arise from bending of the plate and ultimately resisted by a circular area near the plate ends as shown in Figure 2.13. Finite element analyses showed this stress to have a similar circular distribution towards the strip ends as that assumed by Oehlers and Nguyen as seen in Figure 4.3, where stresses of similar magnitude but different orientations (indicated by different colors) are present on the adhesive-to-concrete interface near the strip ends, hence confirming their assumption as a reasonable one.

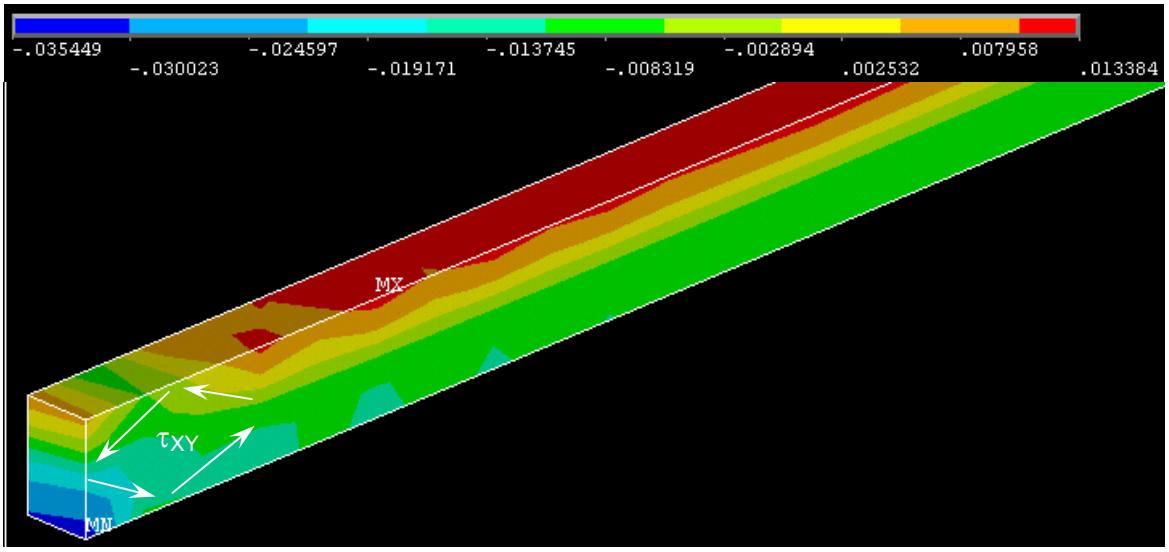

Figure 4.3. Typical distribution of shear stress τ_{XY} from finite element analyses

The derivation of an expression for this stress was then based in Oehlers and Nguyen's PE debonding model for side plates, with the appropriate modifications to suit a section strengthened with an NSM strip.

Assuming linear elastic behavior, and considering the NSM strip is bonded to the concrete so the curvature in the concrete section, the strip and the composite section are the same

$$\phi = \frac{M_c}{(EI)_{RC}} = \frac{M_s}{(EI)_{frp}} = \frac{M_{cs}}{(EI)_{cmp}} \tag{4.1}$$

where M_c, M_s and M_{cs} are the moments in the concrete section, the strip and the composite section respectively, calculated at the of the strip, and $(EI)_{RC}$, $(EI)_{frp}$ and $(EI)_{cmp}$ are the flexural rigidities of the concrete section, the strip and the composite section respectively, the moment to cause debonding of a strip can be expressed as

$$M_s = M_{cs} \frac{(EI)_{frp}}{(EI)_{cmp}} \tag{4.2}$$

Assuming that although initially the moment on the strip M_s is transmitted over the area $h_s x h_s$ in Figure 4.4 (a), premature debonding is likely to occur at the corners of the strip, and hence M_s will eventually be transmitted on the circular area of diameter h_s as shown in Figure 4.4 (b).

From Figure 4.5, the shear stress τ_h at a distance h from the center of the transmission zone varies linearly (from similar triangles) according to

$$\tau_h = \frac{h}{(h_s/2)}\tau_{\max} = \frac{2h\tau_{\max}}{h_s} \tag{4.3}$$

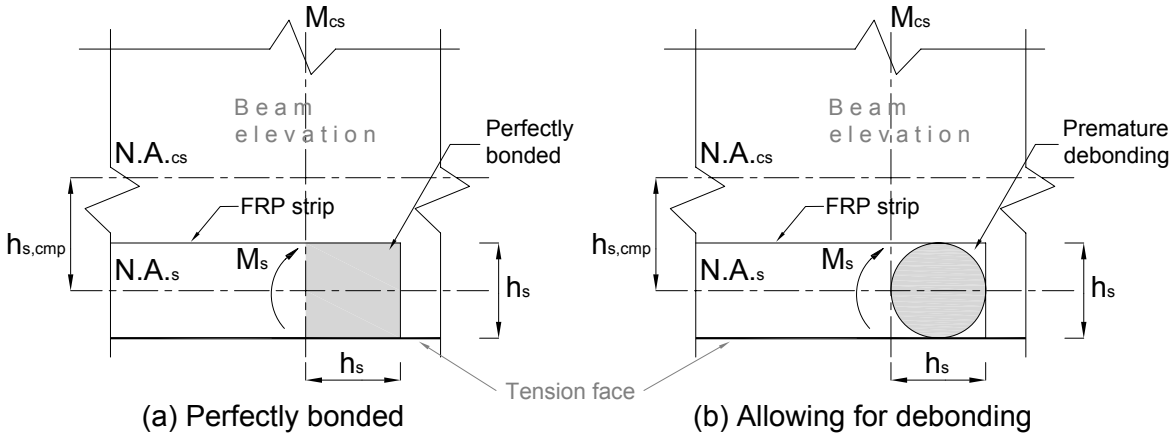

Figure 4.4. Strip bending moment transmission on an NSM strip

The differential increment in moment due to τ_h is then given by

$$dM = 2(2\pi h dh)(\tau_h h) = 4\pi h^2 \tau_h dh \tag{4.4}$$

Substituting τ_h from Equation 4.3

$$dM = \frac{8\pi h^3 \tau_{\max} dh}{h_s} \tag{4.5}$$

Integrating over the circular stress transmission area

$$M_s = \int_0^{h_s/2} \frac{8\pi h^3 \tau_{\max}}{h_s} dh = \frac{\pi \tau_{\max} {h_s}^3}{8} \tag{4.6}$$

and substituting for M_s in Equation 4.2 yields the expression for maximum shear in the plate to concrete interface induced by the plate bending

$$\tau_{XY} = \tau_{\max} = \frac{8M_{cs}(EI)_{frp}}{\pi h_s^{\,3}(EI)_{cmp}} \tag{4.7}$$

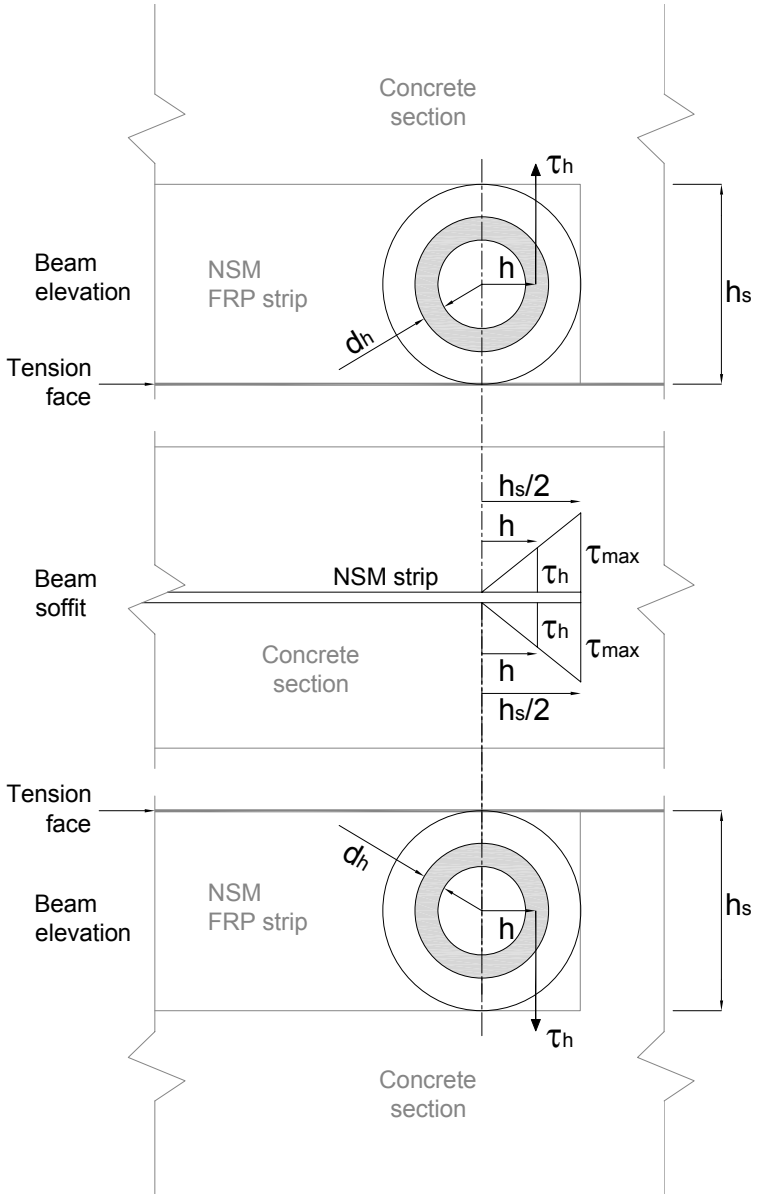

Figure 4.5. Distribution of bond stress resisting M_s

Similar to Hassan and Rizkalla's model, to better reflect the gradual decrease in flexural stiffness of the concrete section, the effective moment of inertia given by Equation 2.39, reproduced here as Equation 4.8, is introduced as the moment of inertia of the composite section.

$$I_{eff} = \left(\frac{M_{cr}}{M_{cs}}\right)^3 I_{g(transformed)} + \left(1 - \left(\frac{M_{cr}}{M_{cs}}\right)^3\right) I_{cr(transformed)} \tag{4.8}$$

In this expression developed by Branson and Trost (1982), M_{cs} and M_{cr} are the applied moment and the cracking moment of the transformed section respectively, and I_g and I_{cr} are the gross and cracked moments of inertia of the transformed strengthened section respectively.

Substituting Equation 4.8 into Equation 4.7 yields the final expression for the magnitude of shear stress τ_{XY}

$$\tau_{XY} = \frac{8M_{cs}(EI)_{frp}}{\pi h_s^{\,3}(EI_{eff})_{cmp}} \tag{4.9}$$

4.2. Longitudinal Shear Stress τ_{XZ}

To obtain an expression for τ_{XZ}, the force induced in the strip by axial strain is first quantified, and then an expression for the corresponding stress in the bonded interface is derived. Due to the derivation of the force induced in the strip by axial strain used in Oehlers and Nguyen's PE debonding model being mechanics-based,

a similar approach was taken to quantify the axial force in the FRP strip, while the derivation of the corresponding interfacial stress was developed for the specific case of NSM strips, with the aid of the finite element models presented in Chapter 3.

One of the observations used for the derivation of an expression for the interfacial stress is illustrated in Figure 4.6, where typical τ_{XZ} shear stress distribution on the concrete to adhesive interface along the length of an NSM strip before and after cracking of the concrete section is shown. Considering that the high stresses towards the left end of the graphs are a consequence of the dof restrains used to take advantage of beam symmetry, it can be seen that, although the stress distribution after cracking is irregular due to discontinuities induced by cracking of the concrete elements, the tendency in the stress variations, with peaks at the strip end (right end of the graphs), and rapidly decreasing towards zero, remain similar.

As before, assuming linear elastic behavior, and considering the NSM strip is bonded to the concrete so the curvature in the concrete section, the strip and the composite section are the same

$$\phi = \frac{M_c}{(EI)_{RC}} = \frac{M_s}{(EI)_{frp}} = \frac{M_{cs}}{(EI)_{cmp}} \tag{4.10}$$

and

$$M_s = M_{cmp} \frac{(EI)_{frp}}{(EI)_{cmp}} \tag{4.11}$$

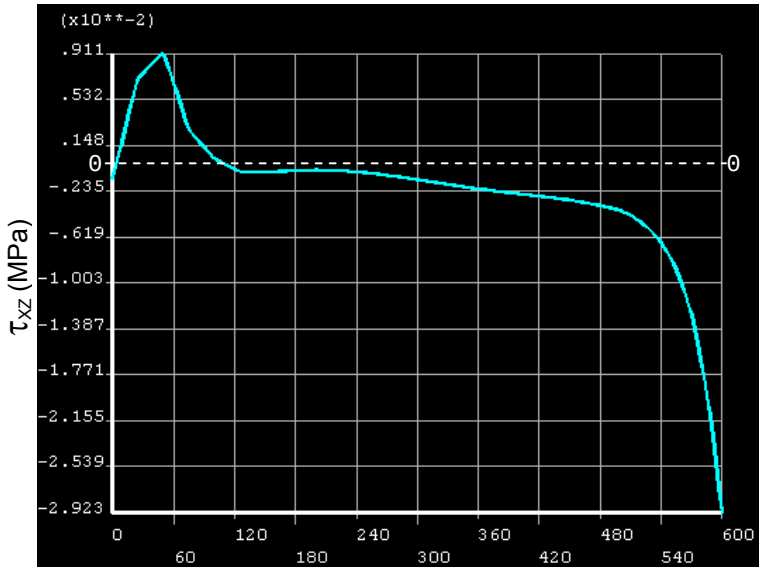

a) Before cracking

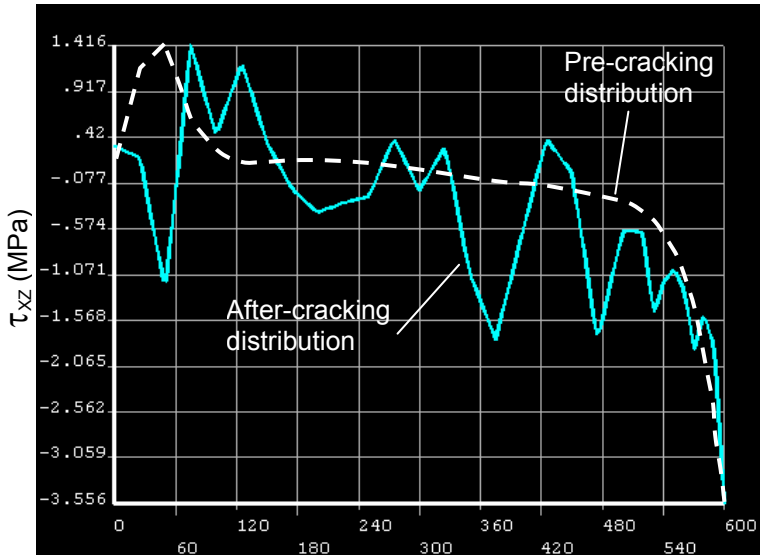

b) After cracking

Figure 4.6. Typical τ_{XZ} distribution along the NSM strip before and after cracking of the concrete section

From Figure 4.7, the strain at the centroid of a plate ε_s is given by

$$\varepsilon_s = h_{s,cmp}\phi \tag{4.12}$$

where $h_{s,cmp}$ is the distance from the centroid of the composite section to the centroid of the FRP strip.

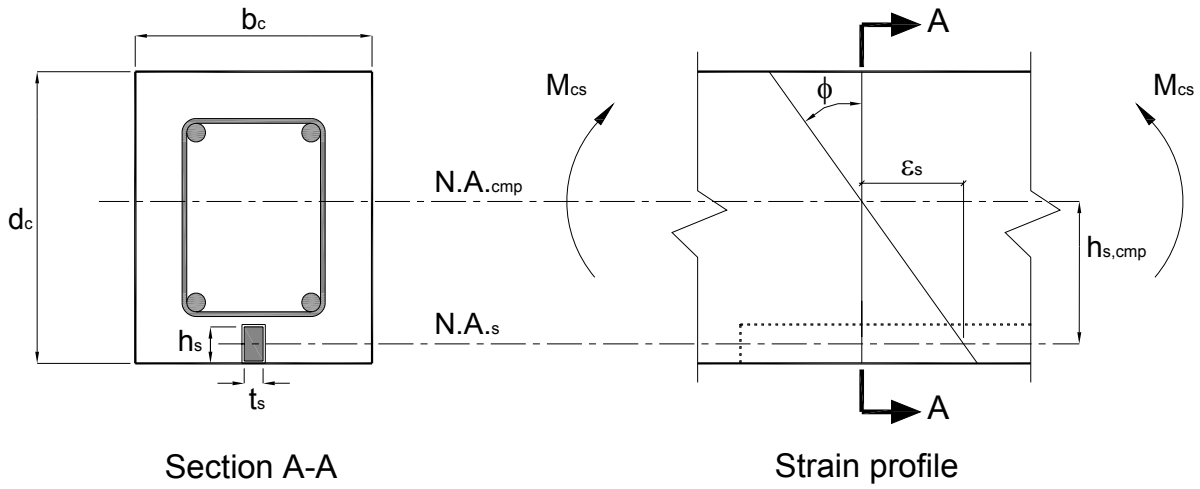

Figure 4.7. Strain distribution on an NSM strip strengthened beam

The axial force induced in the strip due to bending F_s can then be expressed as

$$F_s = A_{frp} E_{frp} \varepsilon_s = (EA)_{frp} h_{s,cmp} \phi \tag{4.13}$$

where A_{frp} and E_{frp} are the cross sectional area and the elastic modulus of the FRP strip, respectively. Substituting Φ from Equation 4.10 gives

$$F_s = \frac{(EA)_{frp} h_{s,cmp} M_{cs}}{(EI)_{cmp}} \tag{4.14}$$

Now that the force in the plate due to axial strain has been quantified, the corresponding average stress in the bonded interface near the strip ends can be calculated by dividing the force by the area of the strip resisting most of the force

$$A_r = 2h_s l_r \tag{4.15}$$

where h_s is the strip height, l_r is the resisting length or length over which most of the shear stress is transmitted, and the 2 takes into account the fact that the strip is bonded to the concrete on both sides, as shown in Figure 4.8.

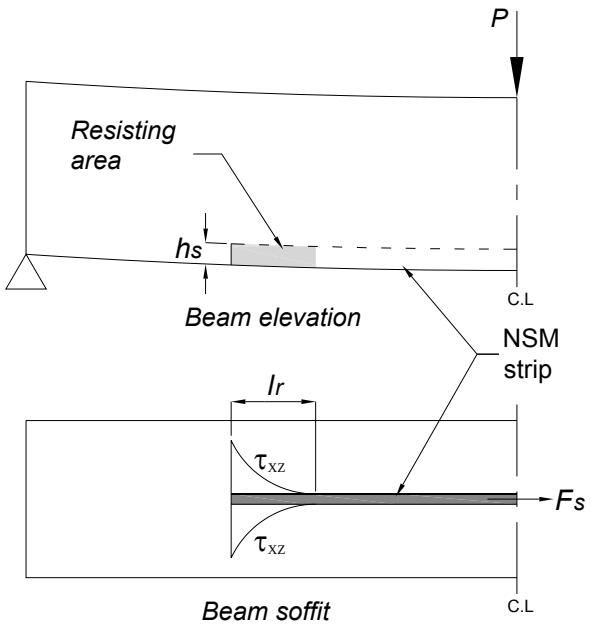

Figure 4.8. Interfacial area resisting the axial force F_s in the NSM strip

Dividing Equation 4.14 by Equation 4.15, the expression for the stress in the bonded interface is obtained

$$\tau_{XZ} = \frac{(EA)_{frp}\, h_{s,cmp} M_{cs}}{(EI)_{cmp}\, 2h_s l_r} \tag{4.16}$$

As for shear stress τ_{XY}, to better reflect the gradual decrease in flexural stiffness of the concrete section, the effective moment of inertia given by Equation 4.8, is introduced as the moment of inertia of the composite section.

$$\tau_{XZ} = \frac{(EA)_{frp}\, h_{s,cmp} M_{cmp}}{(EI_{eff})_{cmp}\, 2h_s l_r} \tag{4.17}$$

As no analytical method exists to estimate l_r, finite element results were initially used to estimate this length. For Hassan and Rizkalla's and Teng et al.'s specimens (the only two sets of beams in which PE debonding occurred experimentally), the lengths of l_r were estimated as 50 mm and 150 mm respectively, as shown in Figure 4.9. Although Figure 4.9 presents stress distributions at loads prior to cracking of the concrete section, as shown before this distribution remains similar after cracking. Further, the length l_r observed in the finite element results, remains constant for the different specimens of a same experimental program, except for those with strips terminating very close to the supports, meaning that in beams likely to fail by PE debonding, l_r is independent of the length of the FRP strip. Subsequently, a parametric study was carried out to identify the parameters affecting the variation of l_r.

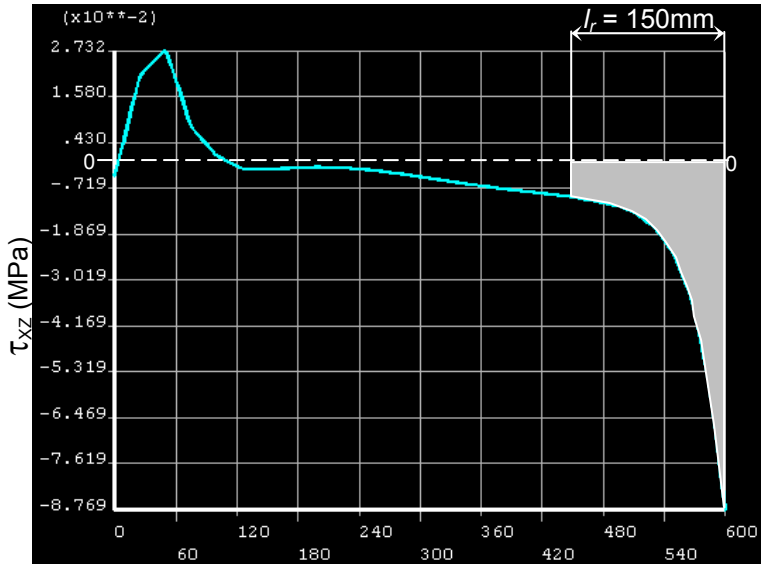

a) Teng et al.'s specimens

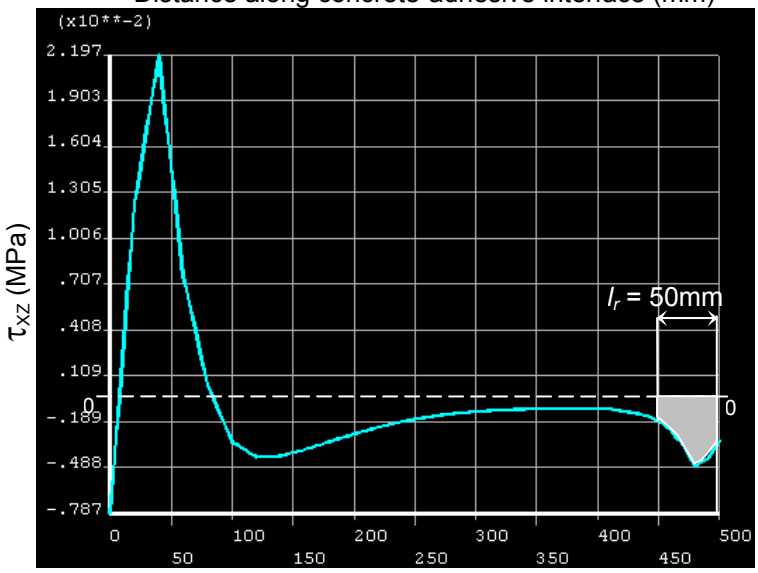

a) Hassan and Rizkalla's specimens

Figure 4.9. Length of l_r estimated from finite element analyses

The variables investigated were the strength of the concrete, the modulus of elasticity of the FRP strip E_{frp}, the height of the strip h_s, the thickness of the strip t_s, the location of the neutral axis of the composite section and the width of the concrete section. Concrete compressive cylinder strengths between 35 and 60 MPa were considered, while FRP strip heights ranged between 10 and 25 mm, both ranges

based on the bounds of what has been used experimentally. The modulus of elasticity of the FRP varied between 170000 MPa, corresponding a higher bound of what was used experimentally in the reviewed literature, and 128500 MPa, corresponding to the equivalent modulus of elasticity of two 2 x 16 mm CFRP strips with a modulus of elasticity of 160000 MPa each, bonded together with a 1 mm thick layer of epoxy adhesive with a modulus of elasticity of 2500 MPa; arrangement which corresponds to that used by Teng et al. (2006) and described in Chapter 2. The thicknesses of the FRP strip were varied between 1.2 and 10 mm, which represent the bounds of commercially available laminates. Rectangular concrete cross-sections were always used, changes in the location of the neutral axis induced by incrementing the depth of the section between 300 and 600mm, while maintaining a section breadth of 150 mm. The concrete section widths considered ranged between 150 and 100mm, while maintaining constant groove dimensions.

Changes in the strength of the concrete, the width of the concrete section, the modulus of elasticity and the height of the FRP strip did not produce any change in l_r. Increasing the distance from the strip to the neutral axis of the section caused the peak of the shear stress τ_{XZ} to occur slightly behind the strip end, but without altering the length of l_r, as shown in Figure 4.10. This displaced location of the peak stress can also be observed in Figure 4.9b, where the shift of the neutral axis is caused by the use of a T-section.

However, change in the thickness of the strip resulted in a strong variation in l_r as shown in the second column of Table 4.1. Although the reason for this is unclear, it is worth noting that the interfacial stress distribution found by Oehlers and Nguyen

(2000) through finite element analyses shown in Figure 2.15, was also deemed to be a function of the FRP plate thickness.

Figure 4.11 shows the variation of l_r as a function of t_s, for which the best fitting tendency line corresponds to the exponential curve shown, with $R^2 = 0.941$. Solving the best fit curve equation for x, which represents l_r

$$l_r = 69.93\ln(1.9731t_s) \tag{4.18}$$

Using Equation 4.18 causes some loss of accuracy when estimating l_r, particularly for thinner strips, as can be seen in the third column of Table 4.1. Rounding the coefficients of Equation 4.18 for ease of use, l_r can be written as

$$l_r = 70\ln(2t_s) \tag{4.19}$$

which causes a small loss of accuracy in comparison with the results obtained using Equation 4.18, as shown in the last column of Table 4.1.

Substituting Equation 4.19 in Equation 4.17 yields an expression to quantify shear stress τ_{XZ} in terms of applied moment and material and geometric properties of the strengthened section

$$\tau_{XZ} = \frac{(EA)_{frp}\, h_{s,cmp} M_{cs}}{140(EI_{eff})_{cmp}\, h_s \ln(2t_s)} \tag{4.20}$$

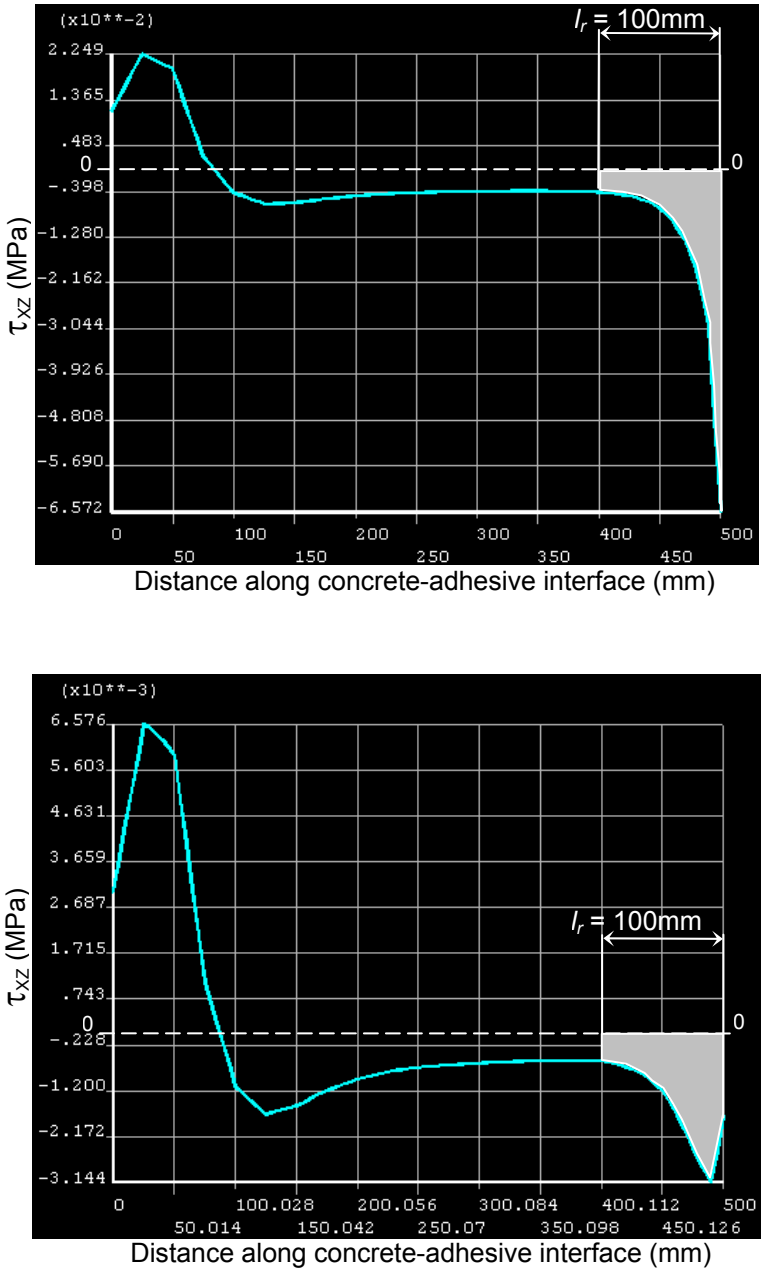

a) Original stress distribution

b) Stress distribution for an increased distance to the neutral axis

Figure 4.10. Effect of change in the location of the section's neutral axis on the τ_{XZ} distribution

Table 4.1. Variation of l_r with change in strip thickness t_s

t_s (mm)	l_r (mm)		
	FE result	Equation 4.18	Equation 4.19
1.2	50	60	61
2	100	96	97
3	150	124	125
4	150	144	146
6	165	173	174
8	185	193	194
10	200	209	210

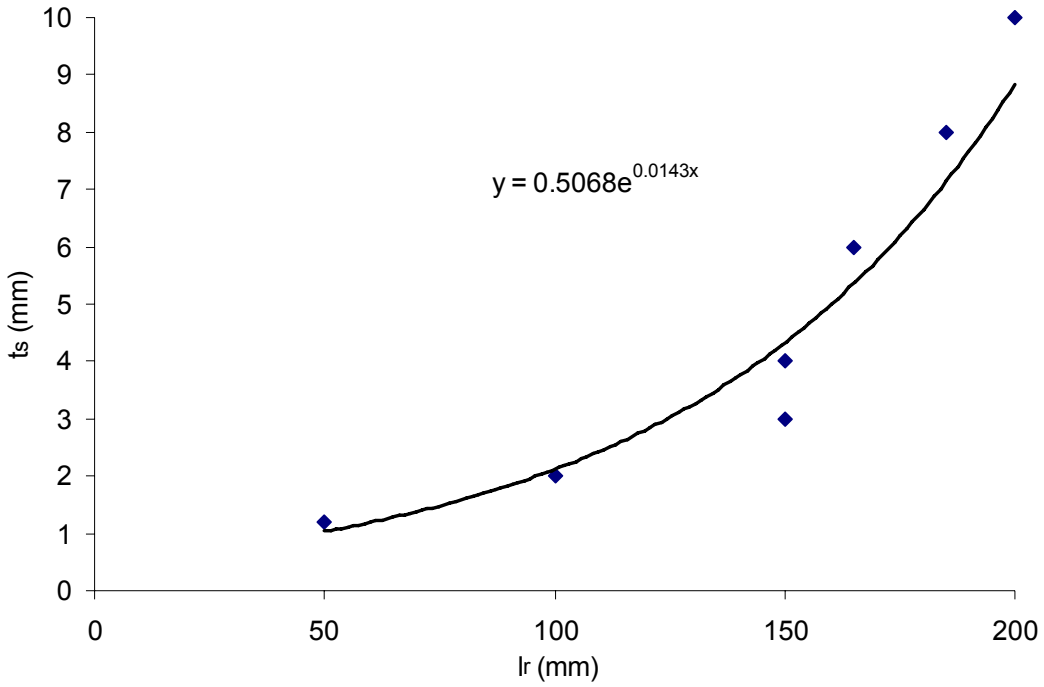

Figure 4.11. Variation of l_r with change in strip thickness t_s

4.3. Normal Stress σ_{XX}

Study of the magnitude of σ_{XX} at the adhesive-to-concrete interface near the strip ends from finite element analyses for both sets of modeled beams, showed that although its value is very irregular right after cracking, it eventually remains tensile,

increasing gradually until reaching approximately the tensile strength of the concrete at a load level around which the shorter strips started to debond experimentally, as shown in Figure 4.12. Conceptually, this tensile stress can be interpreted as the FRP strip "pulling" on the concrete through the adhesive, as it tries to remain straight when the concrete section bends under flexure, as illustrated in Figure 4.13.

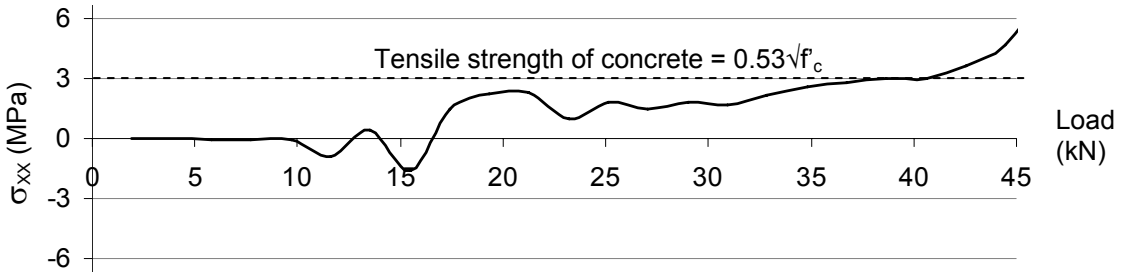

a) Typical results for Teng's specimens (f'_c= 35 MPa)

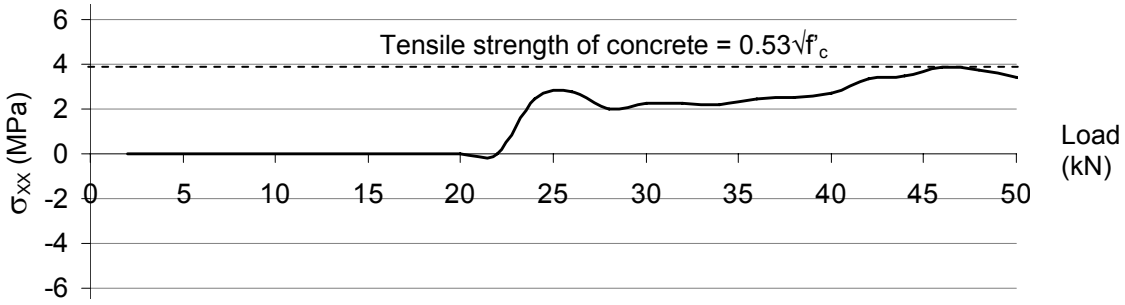

b) Typical results for Hassan and Rizkalla's specimens (f'_c= 57 MPa)

Figure 4.12. Magnitude of σ_{XX} at the strip end for different load levels

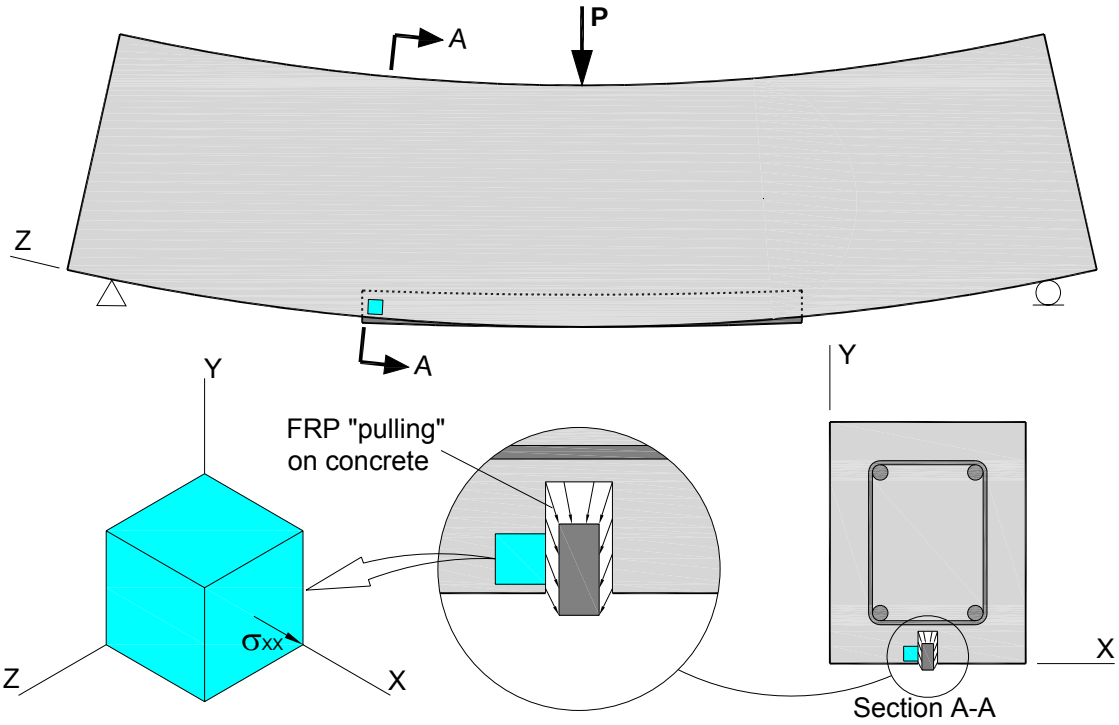

Figure 4.13. Conceptual interpretation of tensile stress σ_{XX}

From this observation, and considering that being a tensile normal stress in concrete the highest value σ_{XX} can attain is the tensile strength of the concrete, it was decided to make σ_{XX} equal to the tensile strength of the concrete f_{ct} at debonding given by

$$\sigma_{XX} = f_{ct} = 0.53\sqrt{f'_c} \qquad \text{[MPa]} \qquad (4.21)$$

4.4. Resultant Stress

To enable the use of a simple and practical failure criterion, the principal stresses corresponding to the three quantified stresses (τ_{XZ}, τ_{XY} and σ_{XX}) are calculated. In general, the principal stresses of a given state of stress are the roots of

$$\sigma^3 - I_1\sigma^2 + I_2\sigma - I_3 = 0 \tag{4.22}$$

where

$$I_1 = \sigma_{XX} + \sigma_{YY} + \sigma_{ZZ} \tag{4.23}$$

$$I_2 = \sigma_{XX}\sigma_{YY} + \sigma_{XX}\sigma_{ZZ} + \sigma_{YY}\sigma_{ZZ} - \tau_{XY}^2 - \tau_{XZ}^2 - \tau_{YZ}^2 \tag{4.24}$$

$$I_3 = \begin{vmatrix} \sigma_{XX} & \tau_{XY} & \tau_{XZ} \\ \tau_{XY} & \sigma_{YY} & \tau_{YZ} \\ \tau_{XZ} & \tau_{YZ} & \sigma_{ZZ} \end{vmatrix} \tag{4.25}$$

However, because σ_{YY}, σ_{ZZ} and τ_{YZ} are considered negligible in the modeling of the PE debonding mechanism, as discussed at the beginning of the Chapter, Equations 4.23 to 4.25 simplify to

$$I_1 = \sigma_{XX} \tag{4.26}$$

$$I_2 = -\tau_{XY}^2 - \tau_{XZ}^2 \tag{4.27}$$

$$I_3 = \begin{vmatrix} \sigma_{XX} & \tau_{XY} & \tau_{XZ} \\ \tau_{XY} & 0 & 0 \\ \tau_{XZ} & 0 & 0 \end{vmatrix} = 0 \tag{4.28}$$

Substituting the results of Equations 4.26 through 4.28 into Equation 4.22, and obtaining the roots of the resulting equation yields principal stresses σ_1, σ_2 and σ_3. Due to the fact that some stresses are zero, regardless of the values of τ_{XZ}, τ_{XY} and σ_{XX}, σ_2 will always result to be zero, while σ_1 will be a tensile stress and σ_3 a compressive stresses of greater magnitude than σ_1.

For this resulting plane state of stress, as shown in Figure 4.14, the corresponding maximum shear stress calculated using Mohr's circle is given by Equation 4.29. At τ_{max} (point A in Figure 4.14 a)), the corresponding normal stress is compressive, as illustrated in Figures 4.14 a) and b).

$$\tau_{max} = \frac{|\sigma_1| + |\sigma_3|}{2} \tag{4.29}$$

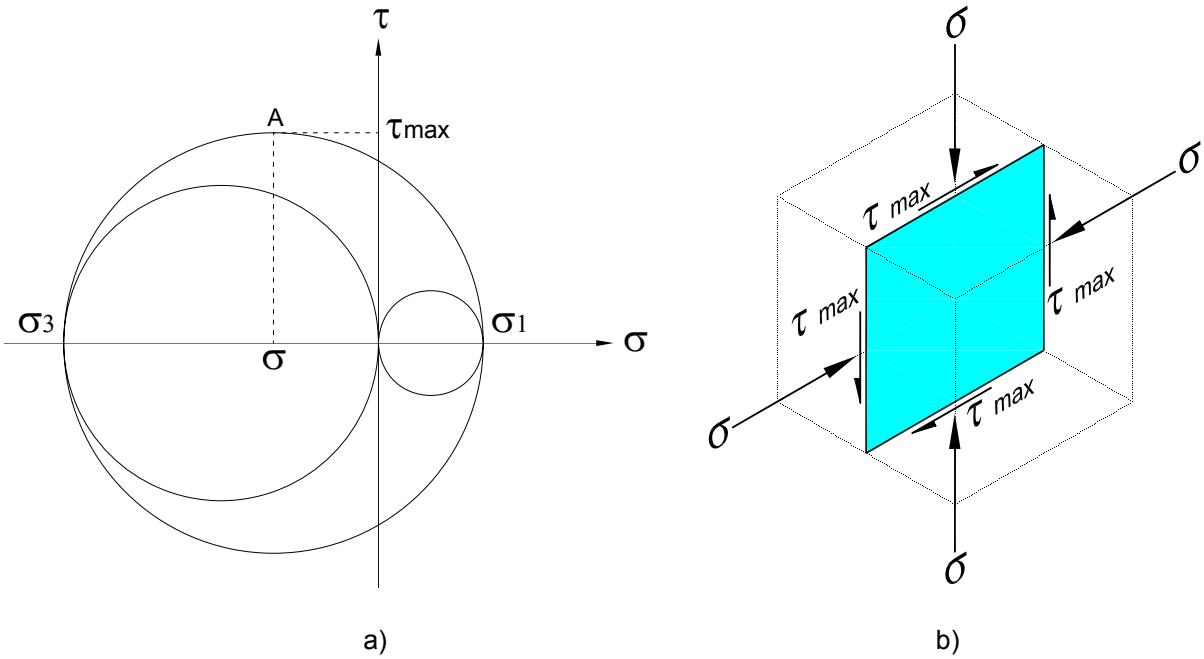

a) b)

Figure 4.14. a) Mohr's circle representation for the resulting plane state of stress, b) state of stress at τ_{max} (point A in Figure 4.14 a))

The shear stress given by Equation 4.29 is then the resultant stress due to applied load which has to be resisted by the concrete. A failure criterion must now be introduced to set the limit of concrete's resistance which will define the PE

debonding load of the strengthened section. Two failure criteria were considered, the Mohr-Coulomb failure criterion for pure shear states of stress, and a failure criterion developed by Mattock and Hawkins (1972) for transfer of shear across a crack. Both failure criteria and their application to the proposed PE debonding model are discussed in the next Section.

4.5. Failure Criteria

4.5.1. Mohr-Coulomb Failure Criterion

The Mohr-Coulomb failure criterion yields the shear resistance of concrete on a pure shear state of stress. As illustrated in Figure 4.14, all circles tangential to the Mohr-Coulomb line represent a critical stress combination, and the maximum critical shear stress for the pure shear circle is given by

$$\tau_{\max} = \frac{f'_c \, f_{ct}}{f'_c + f_{ct}} \tag{4.30}$$

An NSM strengthened section will then be predicted to fail by PE debonding of the FRP strip, at the load at which the shear stress given by Equation 4.29 reaches the stress given by Equation 4.30. This failure criterion can be expected to yield a lower bound to the PE debonding resistance, as it does not take into account the beneficial contribution of the normal compressive stress (σ in Figure 4.15) to the shear strength of the concrete.

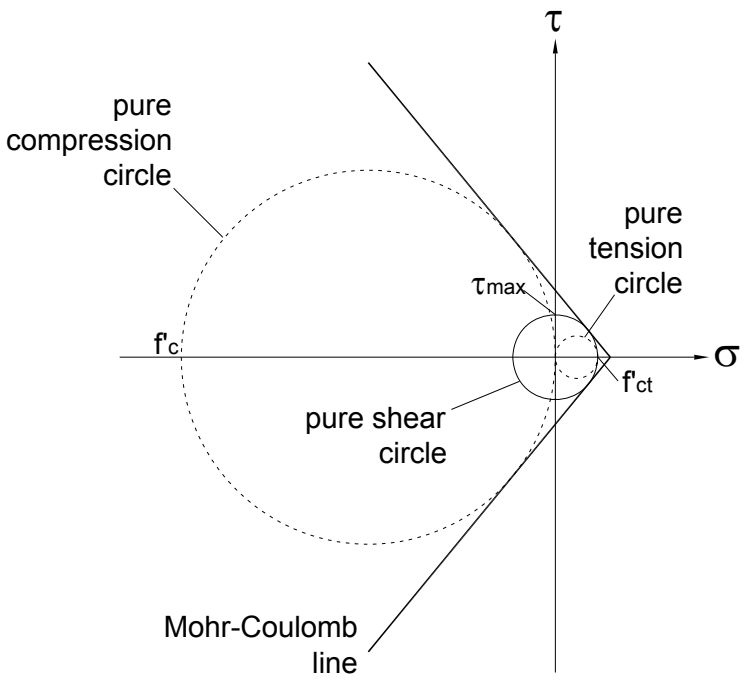

Figure 4.15. Mohr-Coulomb failure criterion

4.5.2. Mattock and Hawkins Failure Criterion

Mattock and Hawkins (1972) developed an equation to determine the shear strength of a cracked shear plane in reinforced concrete. Through experiments of the type shown in Figure 4.16, the amount of shear transfer across the crack was found to be a function of aggregate interlock, dowel action of the reinforcement crossing the crack, and the applied force normal to the crack. The equation defining the shear strength of the cracked shear plane was proposed to be

$$\tau_{\max} = 0.66 f_{ct} + 0.8(pf_{yr} + \sigma_{nf}) \tag{4.31}$$

where the first term corresponds to the lower bound of the fraction of the shear strength that was experimentally found to be attributable to aggregate interlock, pf_{yr} is the axial strength of the reinforcement per unit area, σ_{nf} is the applied stress transverse to the shear plane, and the coefficient 0.8 corresponds to the slope of the best fitting tendency line for the experimental data used to derive the equation, as illustrated in Figure 4.17. The line 0-B-C in Figure 4.17 represents the shear strength of the cracked plane given by Equation 4.31, while line 0-A represents the portion of the strength corresponding to combined reinforcement dowel action and applied stress normal to the shear plane.

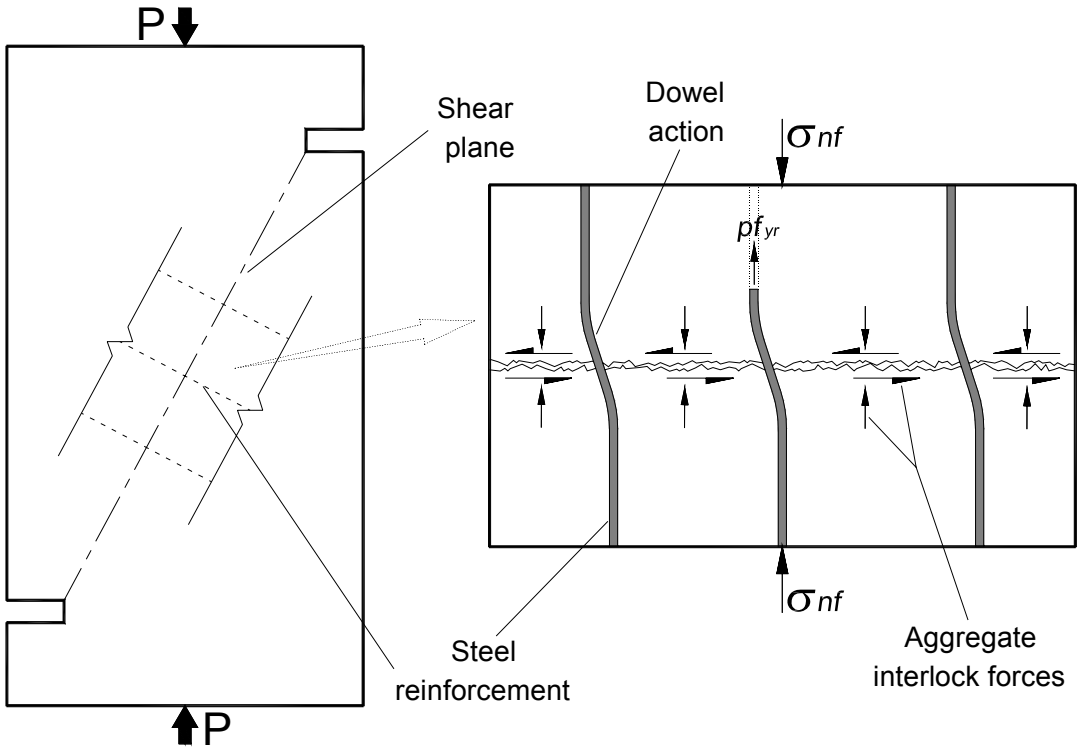

Figure 4.16. Mattock and Hawkins' experiments sketch and mechanism considered for the strength of a cracked shear plane

Equation 4.31 is valid when both

$$pf_{yr} + \sigma_{nf} \geq 0.66 f_{ct} \tag{4.32}$$

and

$$\tau_{\max} \leq 0.3 f_c \tag{4.33}$$

Equation 4.32 accounts for the fact that, as illustrated in Figure 4.17, experimentally the component of the shear strength due to aggregate interlock, only had the magnitude given by Equation 4.31 ($0.66f_{ct}$) when the combined stresses pf_{yr} and σ_{nf} were greater than $0.66f_{ct}$. Below this value, it was estimated that the aggregate interlock strength component decreased as indicated by the dashed curve in Figure 4.17. This effect can be expected in tests of the type carried out by Mattock and Hawkins, as interface interlock cannot occur when the restraint across the crack is removed. The upper limit to the shear strength of the plane given by Equation 4.33 was based in the observation that when large stresses normal to the shear plane exist, the mode of failure changes, as the shear stress reaches the intrinsic strength of the concrete.

As has been described before, PE debonding occurs due to cracking in the concrete adjacent to the adhesive layer, and hence steel reinforcement is not involved in the failure mechanism. Taking this into account, for purposes of the analytical model here proposed, the terms corresponding to dowel action of the steel

reinforcement are taken out of the failure criterion, and σ_{nf} is taken as σ, which can be calculated from σ_1 and σ_3 using Mohr's circle as shown in Figure 4.14. Equation 4.31 then becomes

$$\tau_{\max} = 0.66 f_{ct} + 0.8\sigma \tag{4.34}$$

when both

$$\sigma \geq 0.66 f_{ct} \tag{4.35}$$

and

$$\tau_{\max} \leq 0.3 f'_c \tag{4.36}$$

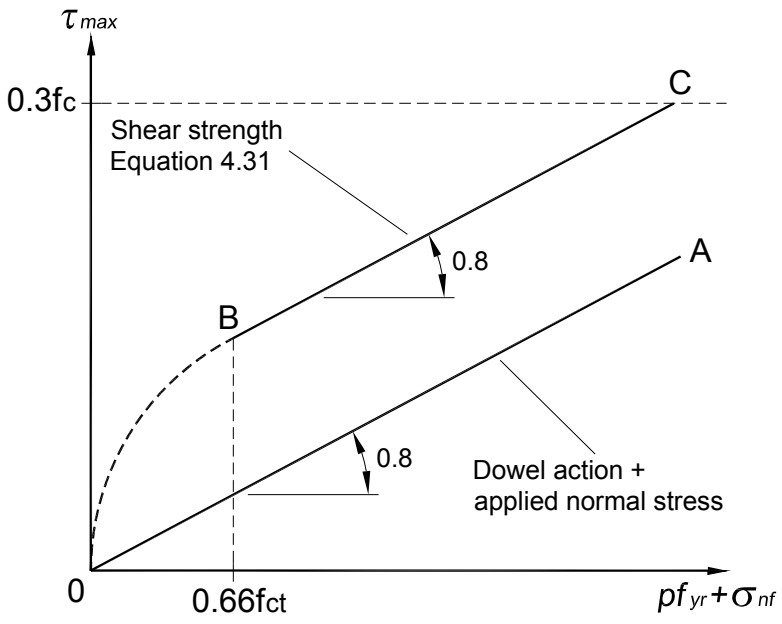

Figure 4.17. Mattock and Hawkins failure criterion

As opposed to the Mohr-Coulomb failure criterion, which is a function of concrete strength only, Equation 4.34 is dependent on the stresses calculated to obtain the maximum applied shear stress given by Equation 4.29. This would suggest the need for an iterative process to find a failure load, as the failure criterion would increase as the applied load increases. However, due to the mathematical process used to calculate principal stresses σ_1 and σ_3, at any load level the difference between $|\sigma_1|$ and $|\sigma_3|$ remains constant, hence σ, which from Mohr's circle is given by

$$\sigma = |\sigma_3| - \tau_{\max} \tag{4.37}$$

where τ_{max} is given by Equation 4.29, also remains constant, as can be observed substituting Equation 4.29 in Equation 4.37 and simplifying to obtain

$$\sigma = \frac{|\sigma_3| - |\sigma_1|}{2} \tag{4.38}$$

Further, it was observed that the difference $|\sigma_1| - |\sigma_3|$ is always equal to the tensile strength of the concrete f_{ct}. Therefore, Equation 4.38 can be written as

$$\sigma = \frac{f_{ct}}{2} \tag{4.39}$$

Substituting Equation 4.39 in Equation 4.34, Mattock and Hawkins' failure criterion for purposes of PE debonding, provided that Equations 4.35 and 4.36 are satisfied, can be written as a function of f_{ct} only

$$\tau_{\max} = 1.06 f_{ct} \quad (4.40)$$

Assuming this failure criterion, an NSM strengthened flexural member will fail by PE debonding at the load at which the applied shear given by Equation 4.29, reaches the concrete shear strength given by Equation 4.40. This failure criterion is expected to yield higher debonding loads than those obtained using the Mohr-Coulomb failure criterion, as it accounts for the contribution to the shear strength of the compressive stress that occurs at τ_{max}, as shown in Figure 4.14.

In the following Section, the proposed analytical model presented in this Chapter is assessed against all available relevant experimental data, considering the outcomes obtained using both the Mohr-Coulomb, and Mattock and Hawkins' failure criteria. For clarity, Appendix A presents an example of the use of the proposed model to calculate one of the failure loads presented in Section 4.6.

4.6. Assessment of the Proposed Model

Table 4.2 shows theoretical debonding loads calculated using the existing analytical models presented in Chapter 2, as well as the proposed model considering both the Mohr-Coulomb failure criterion and Mattock and Hawkins' failure criterion. As in Table 2.13, the results are grouped by predicted theoretical debonding mechanism, and it can be seen that with the exception of Hassan and Rizkalla's specimen B3, which will be discussed later, this classification is not altered when the proposed model is considered, as the debonding loads calculated with the

Table 4.2. Summary of theoretical failure loads including the proposed model

Theoretical debonding mechanism	Author (s)	Specimen	Theoretical failure load (kN)				
			Unified IC model		Hassan and Rizkalla's model	Proposed model	
			Common failure plane	Individual failure planes		Mohr-Coulomb	Mattock & Hawkins
IC debonding	1	B8	66.08	66.08	Rupture	1086.32	1280.15
		B7	66.08	66.08	Rupture	271.75	320.24
		B6	66.08	66.08	Rupture	181.31	213.89
		B5	66.08	66.08	70.00	136.05	160.32
		B4	66.08	66.08	55.00	108.79	128.09
	2	B2	72.51	93.25	Rupture	913.58	1055.08
		B3	73.84	99.23	Rupture	1330.00	1558.97
		B4	73.86	106.32	Rupture	995.46	1168.68
	3	S1	42.81	42.81	55.00	201.50	235.12
	4	B2900	82.73	82.73	Rupture	844.84	1008.48
	5	A2	65.04	93.62	170.00	359.92	412.68
		A4	76.77	110.22	167.50	379.68	439.24
		B2	64.25	91.86	165.00	362.62	419.51
		B4	75.08	106.96	160.00	373.35	436.40
	6	S1	63.78	63.78	65.00	193.40	217.11
CDC debonding			CDC model				
	3	S2	56.86		62.50	174.87	202.62
		S3	58.00		62.50	191.12	223.41
		S4	62.00		72.50	182.37	212.60
	6	S2	76.00		70.00	168.64	188.00
		S3	77.00		75.00	159.47	178.25
PE debonding			Modified PE model				
	1	B3	54.16		37.50	72.00	85.56
		B2	40.62		27.50	53.39	64.08
		B1	36.93		25.00	49.42	58.25
	4	B1800	59.38		20.00	70.52	84.15
		B1200	39.58		12.50	47.01	56.10
		B500	29.69		10.00	35.26	42.07

Author (s) key: 1- Hassan and Rizkalla (2003)
2- El-Hacha and Rizkalla (2004)
3- Barros and Fortes (2005)
4- Teng et al. (2006)
5- Kotynia (2006)
6- Barros et al. (2007)

proposed model are always greater than the theoretical IC and CDC debonding loads.

Table 4.3 shows experimental debonding loads for all beams considered to have failed theoretically by PE debonding in Chapter 2. Debonding loads predicted using Oehlers and Nguyen's modified PE debonding model, Hassan and Rizkalla's model, and the proposed model with both the Mohr-Coulomb and Mattock and Hawkins' failure criteria, are also shown for each specimen. As an indication of the accuracy of the theoretical prediction of individual specimens, ratios of the theoretical debonding load to the experimental debonding load are given, along with an average for all specimens. Finally, as a measure of the consistency of each model's predictions, the standard deviation of the individual theoretical/experimental ratios is also given.

Table 4.3. Performance of PE debonding models

Specimen	Experimental Debonding (kN)	Modified Oehlers and Nguyen				Hassan and Rizkalla				Proposed model with Mohr-Coulomb failure criterion				Proposed model with Mattock and Hawkins failure criterion			
		Debonding Load (kN)	Theo/Exp	Average Theo/Exp	Std Dev	Debonding Load (kN)	Theo/Exp	Average Theo/Exp	Std Dev	Debonding Load (kN)	Theo/Exp	Average* Theo/Exp	Std Dev*	Debonding Load (kN)	Theo/Exp	Average* Theo/Exp	Std Dev*
B3	60.00	54.16	0.90			37.50	0.63			72.00	1.20			85.56	1.43		
B2	54.00	40.62	0.75			27.50	0.51			53.39	0.99			64.08	1.19		
B1	53.00	36.93	0.70	0.71	0.11	25.00	0.47	0.37	0.18	49.42	0.93	0.84	0.12	58.25	1.10	0.99	0.14
B1800	91.70	59.38	0.65			20.00	0.22			70.52	0.77			84.15	0.92		
B1200	63.10	39.58	0.63			12.50	0.20			47.01	0.75			56.10	0.89		
B500	47.80	29.69	0.62			10.00	0.21			35.26	0.74			42.07	0.88		

*Does not include specimen B3

It can be seen that the average theoretical/experimental ratios of the proposed model are considerably improved in comparison to the existing models, while maintaining acceptable scatter. Using the Mohr-Coulomb failure criterion results in a moderate underestimation of the failure loads, while as expected Mattock and Hawkins' failure criterion produces higher debonding loads on average more accurate, but that overestimate the debonding resistances of all Hassan and Rizkalla's specimens. Specimen B3 was not included in the average theoretical/experimental values or in the standard deviations for the proposed model due to the predicted debonding loads being larger than its corresponding IC debonding load, meaning that according to the proposed model, specimen B3 would not be classified as failing by PE debonding.

The variation of the theoretically predicted debonding mechanism of specimen B3 depending on which model is used, is likely to be a reflection of the beam having failed by a combination of IC and PE debonding, as described by the authors of the experiment. The IC debonding load of the beam was estimated to be 66 kN in Section 2.6.1, not far below the PE debonding load predicted by the proposed model using the Mohr-Coulomb failure criterion, which suggests the likelihood of IC debonding occurring just before PE debonding.

For both Hassan and Rizkalla's and Teng et al.'s specimens, Equation 4.35 is not satisfied, meaning that Mattock and Hawkins' failure criterion, as given by Equation 4.34 or 4.40 is not valid. As discussed in Section 4.4.2 and illustrated in Figure 4.17, Mattock and Hawkins found experimentally that for stresses normal to the shear plane lower than $0.66f_{ct}$, the portion of the shear strength corresponding to

aggregate interlock decreased as indicated by the dashed curve 0-B in Figure 4.17. As this curve is not defined, conservatively a linearly decreasing line between 0 and B can be assumed for the aggregate interlock fraction of the shear strength. This approach results in a shear strength τ_{max} lower than that yielded by the Mohr-Coulomb failure criterion, which is considered to be contradictory, as the Mohr-Coulomb failure criterion is a reliable estimate of concrete's shear strength when subjected to pure shear, and hence a concrete shear strength model that accounts for a certain degree of transverse restraint across the crack would be expected to yield higher capacities. Further, in Mattock and Hawkins's experiments, it could be expected that the removal of dowel action and applied stress normal to the shear plane results in the loss of aggregate interlock, as the two sides of the concrete specimen could freely displace, allowing the faces of the shear plane to move relative to each other. However in the case of debonding of an NSM strip, the failure planes are confined from both sides, as illustrated in Figure 4.18, and hence a certain degree of aggregate interlock can be expected to remain up to failure. Therefore, although one of the conditions for the use of Mattock and Hawkins' failure criterion is violated, the concrete shear strength given by Equation 4.40 was used to calculate the debonding loads in Table 4.3, which should be regarded as an approximation of an upper bound of the PE debonding strength calculated with the proposed model.

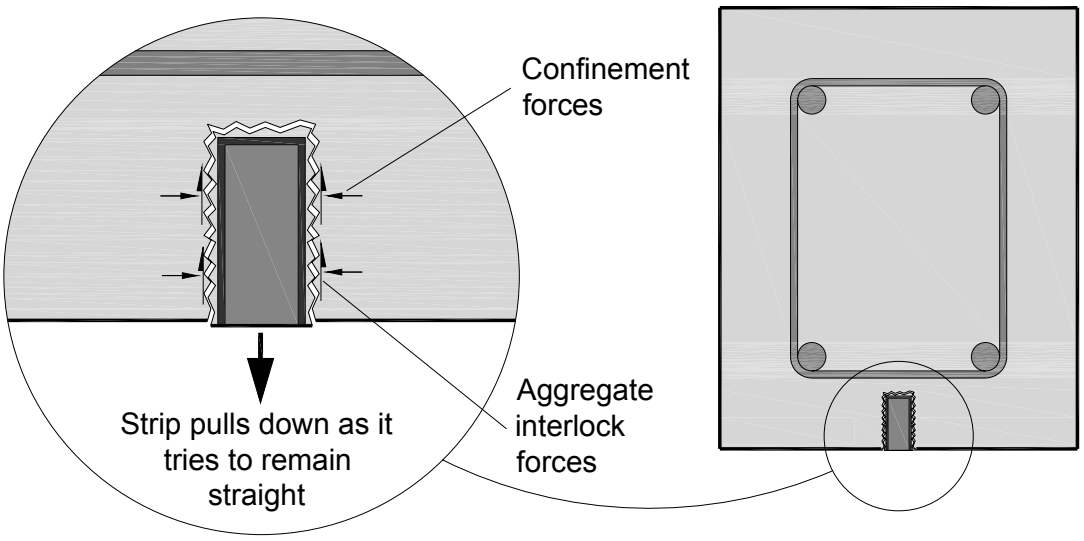

Figure 4.18. Confinement and aggregate interlock forces on NSM strip

In conclusion, based on the available experimental results, the proposed model developed on a rational approach to the PE debonding mechanism, predicts more accurate results than the previous models, which considerably underestimate the PE debonding capacity of flexural members strengthened with NSM FRP strips. It is recommended that the Mohr-Coulomb failure criterion be used to establish a limit to the shear strength of the concrete, as it yields conservative yet adequately accurate results. Care must be taken when assessing the PE debonding strength of elements retrofitted with NSM strips of intermediate length such as Hassan and Rizkalla's specimen B3, as interaction with IC debonding may occur, making it difficult to establish what the expected failure mechanism is.

5. Conclusions

5.1. Summary

In this research thesis the existing theoretical debonding models for NSM strengthening with FRP strips were identified through a comprehensive literature review, and then their performance evaluated against all relevant experimental results found in the literature. This analysis showed that for IC and CDC debonding there are models that yield either good results or consistently underestimate the debonding strength, meaning that although they may still require further development to improve accuracy, they capture the essential behavior of the debonding mechanism.

However for PE debonding the existing models significantly underestimate the failure loads, which provided the motivation for this research focusing on better understanding the PE debonding mechanism and formulating an analytical model for this type of failure. Using accurate 3D finite element analyses, the stress distribution near the ends of NSM strips was studied for different beams tested as part of experimental programs carried out by other researchers. This, together with some of the findings of the literature review, allowed the formulation of a rational PE debonding model which, when assessed against the currently available experimental results, showed to perform better than the existing models.

5.2. Conclusions

From the results obtained in this research thesis the following conclusions can be drawn:

1. Seracino et al.'s unified IC debonding model yields in general good results for NSM retrofitted beams with FRP strips. The accuracy of the model changes depending on whether a common failure plane or individual failure planes are assumed for beams strengthened with strips installed in two or more grooves. The assumption of individual failure planes results in more accurate failure loads than the common failure plane assumption, although the decrease in strain with the increase in number of grooves observed experimentally is not reflected by the results when the individual failure planes assumption is made. As a rule, it has been suggested by other researchers that when the spacing between adjacent grooves is greater than 2.5 times the width of the grooves, the FRP strips will fail individually.
2. The CDC debonding model given in Oehlers and Seracino (2004) consistently underestimates the debonding strength of NSM retrofitted beams. It is possible that the additional debonding strength not being captured by the model is due to the development of strain in the stirrups, which are not taken into account in the model because it was derived for EB plates, which typically debond at low strains, hence not allowing for the development of strength from the stirrups. Subject to confirmation as more experimental results become available, it has been proposed that the additional strength provided by the stirrups can be calculated as a fraction of

the total stirrup strength. Based on the experimental results analyzed in this research thesis, that fraction may be taken as 0.3, although if uncertain, a conservative result is obtained neglecting this fraction strength.

3. The existing theoretical models applicable to PE debonding significantly underestimate the debonding resistance of flexural elements retrofitted with NSM strips.
4. The analytical model proposed in this thesis, based on a 3D state of stress identified as the most critical stress combination near the strip ends, allows the calculation of the PE debonding load of flexural elements strengthened with NSM FRP strips, in terms of material and geometric properties. Assessed against the currently available experimental results, the model yields considerably more accurate debonding loads than the existing models.
5. Based on the proposed analytical model and on the finite element analyses carried out, the thickness of an NSM FRP strip is an important factor on the PE debonding behavior. Thickness changes on commonly used thin laminates (1.2 – 4mm thick), produce particularly large variations in the calculated debonding loads.
6. For the proposed PE debonding mechanism, the Mohr-Coulomb failure criterion gives a good conservative estimate of the shear strength of concrete. Mattock and Hawkins' failure criterion provides an approach that better represents the expected behavior of cracked concrete adjacent to the adhesive layer of an NSM FRP strip, although to be more appropriate for its

application to PE debonding, the concept needs to be further developed taking into account the particular conditions of this debonding mechanism.

7. FRP-strengthened reinforced concrete elements can be adequately modeled in 3D with the finite element analysis software ANSYS, using the “Solid 65” element to model concrete and epoxy adhesive and the “Solid 45” element to model FRP. The load-deflection behavior of the member is accurately predicted by the program up to yielding of the longitudinal rebar, after which the detachment of the FRP is not captured, as the program is capable of modeling progressive deterioration of the concrete, but not sudden complete loss of the material integrity.

5.3. Future Research

A number of aspects arose over the course of this research that although were not further investigated due to the scope of this thesis, are considered to be worth additional attention due to the importance they may have in the continued development of a theoretical basis for the application of NSM strengthening:

1. Although Seracino et al.’s IC debonding model produces more accurate results when assuming separate failure planes than when assuming a common failure plane, the common failure plane assumption reflected better the debonding mechanism, as suggested by the decrease in maximum strain in the FRP as the number of strips increased. If for this last assumption, the contribution to the stiffness of the cracked concrete in between the strips is taken into account, it is expected that more accurate results could be

obtained. Incorporating this effect to the model would improve its performance, as results would not only be accurate but also consistent with the debonding mechanism.

2. For CDC debonding on NSM strengthened elements, the amount of strength that is developed in the stirrups is considered to be important to investigate, as this can be the key to an accurate CDC debonding model.
3. The parametric analysis described in Chapter 4 to identify the cause of the variation in l_r clearly indicated that it is only the thickness of the FRP strip what affects this length. However it is not yet understood why, and hence it is considered that further study of this behavior may prove useful to improve the debonding models for NSM FRP.
4. The amount of longitudinal steel reinforcement has shown to be influential in the debonding mechanism of beams strengthened in flexure under certain conditions. This is a factor that is not yet fully understood, and it's considered to be worth of further attention, so interaction between FRP and steel reinforcement can be accounted for and designed against if necessary.
5. Due to the FRP strains achievable in NSM strips, interaction between the IC and the PE debonding mechanisms can occur. Quantifying when interaction is likely to occur is considered to be worth further study, as it is an influential factor towards obtaining consistently accurate predictions.
6. Developing a practical, straightforward failure criterion based on Mattock and Hawkins' approach, for confined unreinforced concrete, can help improve the PE debonding predictions obtained with the proposed model, and potentially

be useful for other applications as well. Such work, to the author's knowledge, has not been published before.

6. References

ACI Committee 318, “Building Code Requirements for Structural Concrete (ACI 318-05) and Commentary (318R-05)”, American Concrete Institute, Farmington Hills, MI, pp. 430.

Barbosa, A. and Ribeiro, G., “Analysis of Reinforced Concrete Structures Using ANSYS Nonlinear Concrete Model”, Computational Mechanics New Trends and Applications, Barcelona, Spain, 1998.

Barros, J., Dias, S. and Lima, J., “Efficacy of CFRP-based Techniques for the Flexural and Shear Strengthening of Concrete Beams”, Cement & Concrete Composites, No. 29, 2007, pp. 203-217.

Barros, J. and Fortes, A., “Flexural Strengthening of Concrete Beams with CFRP Laminates Bonded Into Slits”, Cement & Concrete Composites, No. 27, 2005, pp. 471-480.

Beber, A. J., Filho, A. C., and Campagnolo, “CFRP in the Strengthening of Reinforced Concrete Beams”, Proceedings of the International Conference on FRP Composites in Civil Engineering, Hong Kong, China, 2001, pp. 391-398.

Bensen, J., Flett, A. and Badaoui, A., “Debonding of FRP Near Surface Mounted Reinforcement in Reinforced Concrete Beams”, Honors research report, School of Civil and Environmental Engineering, The University of Adelaide, Australia, 2005.

Branson, D. and Trost, H., “Application of the I-effective Method in Calculating Deflections of Partially Prestressed Memebers”, Journal of the Prestressed Concrete Institute, V. 27, No. 5, 1982, pp. 62-77.

Chen, J., Yuan, H. and Teng, J., “Analysis of Debonding Failure Along Softened FRP-to-concrete Interface Between Two Adjacent Cracks”, Proceedings of International Symposium on Bond Behaviour of FRP in Structures, Hong Kong, China, 2005, pp. 103-111.

Chin, J., Nguyen, T. and Aouadi, K., “Effects of Environmental Exposure on Fiber-reinforced Plastic (FRP) Materials Used in Construction”, Journal of Composites Technology & Research, V. 19, No. 4, 1997, pp. 205-213.

Dawood, M., Guddati, M. and Rizkalla, S., “Bond Behavior of a CFRP Strengthening System for Steel Structures”, Proceedings of Asia-Pacific Conference on FRP in Structures, Hong Kong, China, 2007.

De Lorenzis, L. and Teng, J., “Near-Surface Mounted FRP Reinforcement: An Emerging Technique for Strengthening Structures”, Composites Part B: Engineering, V. 38, No. 2, 2007, pp. 119-143.

El-Hacha, R. and Rizkalla, S., “Near-Surface-Mounted Fiber-Reinforced Polymer Reinforcements for Flexural Strengthening of Concrete Structures”, ACI Structural Journal, V. 101, No. 5, 2004, pp. 716-726.

Hassan, T., “Flexural Performance and Bond Characteristics of FRP Strengthening Techniques for Concrete Structures”, Doctoral Thesis, Department of Civil and Geological Engineering, The University of Manitoba, 2002, p. 284.

Hassan, T. and Rizkalla, S., “Investigation of Bond in Concrete Structures Strengthened with Near Surface Mounted Carbon Fiber Reinforced Polymer Strips”, Journal of Composites for Construction, V. 7, No. 3, 2003, pp. 248-257.

Kotynia, R., “Analysis of Reinforced Concrete Beams Strengthened With Near Surface Mounted FRP Reinforcement”, Polish Academy of Sciences Archives of Civil Engineering, V. 52, Issue 2, 2006, pp. 305-317.

Malek, A., Saadatmanesh, H. and Ehsani, M., “Prediction of Failure Load of RC Beams Strengthened with FRP Plate Due to Stress Concentration at the Plate End”, ACI Structural Journal, V. 95, No. 1, 1998, pp. 142-152.

Mattock, A. and Hawkins, N., “Shear Transfer in Reinforced Concrete – Recent Research”, PCI Journal, V. 17, No. 2, 1972, pp. 55-75.

Mohamed Ali, M., Oehlers, D. and Seracino, R., “Vertical Shear Interaction Model Between External FRP Transverse Plates and Internal Steel Stirrups”, Engineering Structures, V. 27, No. 6, 2006, pp. 920-937.

Nguyen, N. and Oehlers, D., “A Mathematical Model for Flexural Peeling of Side-Plated Glued Beams”, Research Report No. R143, School of Civil and Environmental Engineering, The University of Adelaide, Australia, 1997.

Oehlers, D. and Bradford M., “Composite Steel and Concrete Structural Members”, Elsevier, Oxford, UK, 1995.

Oehlers, D. and Moran, J., “Premature Failure of Externally Plated Reinforced Concrete Beams”, ASCE Journal of Structural Engineering, V. 116, No. 4, 1990, pp. 978-993.

Oehlers, D. and Nguyen, N., “Retrofitting by Adhesive Bonding Steel Plates to the Sides of RC Beams”, Structural Engineering and Mechanics, V. 9, No. 5, 2000, pp. 491-503.

Oehlers, D. and Seracino, R., “Design of FRP and Steel Plated RC Structures”. Elsevier, Oxford, UK, 2004.

Seracino, R., Saifulnaz, M. and Oehlers, D., “Generic Debonding Resistance of EB and NSM Plate-to-Concrete Joints”, Journal of Composites for Construction, V. 11, No. 1, 2007, pp 62-70.

Standards Australia, “AS 3600-2001: Concrete Structures”, Third Edition, 2001.

Standards Australia, “HB305-200X (200X) RC Structures Retrofitted with FRP and Metal Plates: Beams and Slabs”, SAI Global Ltd, Sydney, Australia. (in press)

Täljsten, B., Carolin, A. and Nordin, H., “Concrete Structures Strengthened with Near Surface Mounted Reinforcement of CFRP”, Advances in Structural Engineering, V. 6, No. 3, 2003, pp. 201-213.

Teng, J., Chen, J. and Smith, S., “Debonding Failures in FRP-strengthened RC Beams: Failure Modes, Existing Research and Future Challenges”, Proceedings of the International Workshop on Composites in Construction, Capri, Italy, 2001, pp. 139-148.

Teng, J., Chen, J., Smith, S. and Lam, L., “Behaviour and Strength of FRP-strengthened RC Structures: A state-of-the-art Review”, Proceedings of the Institution of Civil Engineers: Structures and Buildings, V. 156, No. 1, 2003, pp. 51-62.

Teng, J., De Lorenzis, L., Wang, B., Rong, L., Wong, T. and Lam, L., “Debonding Failures of RC Beams Strengthened with Near Surface Mounted CFRP Strips”, ASCE Journal of Composites for Construction, V. 10, No. 2, 2006, pp. 91-105.

Smith, S. and Teng, J., “FRP-strengthened RC Beams. I: Review of Debonding Strength Models”, Engineering Structures, V. 24, No. 4, 2002, pp. 385-395.

Smith, S. and Teng, J., “Shear-bending Interaction in Debonding Failures of FRP-plated RC Beams”, Advances in Structural Engineering, V. 6, No. 3, 2003, pp. 183-199.

Willam, K. and Warnke, E., "Constitutive Model for the Triaxial Behavior of Concrete", Proceedings of the International Association for Bridge and Structural Engineering, V. 19, Bergamo, Italy, 1975, pp. 174.

Yuan, H., Teng, J., Seracino, R., Wu, Z. and Yao, J., “Full-range Behavior of FRP-to-concrete Bonded Joints”, Engineering Structures, V. 26, No. 5, 2004, pp. 553-565.

Zhang, J.-P., “Diagonal Cracking and Shear Strength of Reinforced Concrete Beams”, Magazine of Concrete Research, V. 49, No. 178, 1997, pp. 55-65.

Appendices

Appendix A: Sample Calculation of Debonding Load Using the Proposed Model

To summarize and clarify how debonding loads are calculated using the proposed analytical model described in Chapter 4, a sample calculation is presented here. Specimen B1 tested by Hassan and Rizkalla (2003) will be used as example. Figure 2.23 is reproduced here as Figure A.1 for convenience.

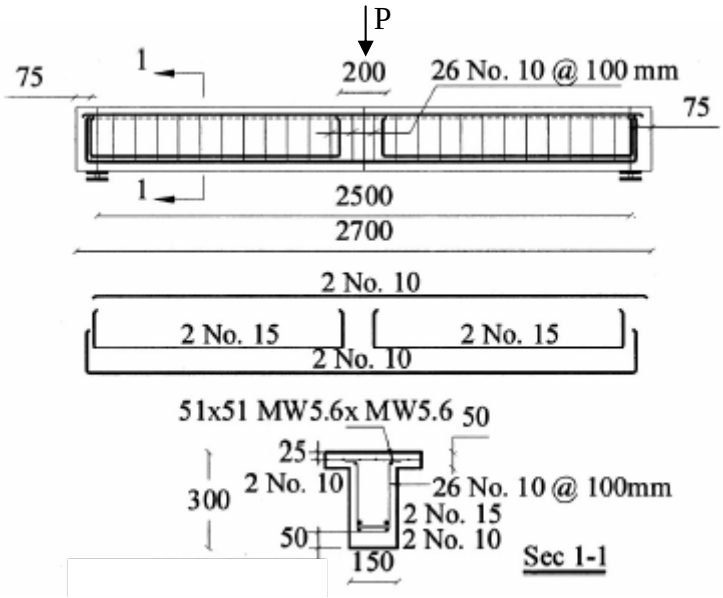

Figure A.1. Typical specimen details (Hassan and Rizkalla, 2003)

Specimen B1 is strengthened with a single 1.2 x 25 mm CFRP strip, 300 mm long. The following material and geometric properties of the strengthened beam are necessary to perform the calculation:

Elastic modulus of FRP strip, E_{frp} = 160000 MPa

Moment of inertia of FRP strip, I = 1562.5 mm^4

Depth of the FRP strip, h_s = 25 mm

Elastic modulus of concrete, E_c = 30000 MPa

Cross-section area of FRP strip, A = 5 mm^2

Depth of centroid of the composite section from the beam top = 132.8 mm

Depth of centriod of the FRP strip from the beam top = 287.5 mm

Thickness of FRP strip, t_s = 1.2 mm

Concrete cylinder compressive strength, f'_c = 48 MPa

As the effective moment of inertia I_{eff} is used in the model, an iterative process as shown in Table A.1 is required, as I_{eff} is a function of the applied load. For each applied load, the corresponding moment at the plate end M_{cs} is calculated, as well as I_{eff} and stresses τ_{XY}, τ_{XZ} and σ_{XX}, using Equations 4.8, 4.9, 420 and 4.21 respectively. In order to calculate I_{eff}, the cracking moment of the concrete section M_{cr}, the gross moment of inertia of the transformed strengthened section I_g and the cracked moment of inertia of the transformed strengthened section I_{cr} must be known.

$$I_{eff} = \left(\frac{M_{cr}}{M_{cs}}\right)^3 I_{g(transformed)} + \left(1 - \left(\frac{M_{cr}}{M_{cs}}\right)^3\right) I_{cr(transformed)} \qquad \text{(Equation 4.8)}$$

$$\tau_{XY} = \frac{8 M_{cs} (EI)_{frp}}{\pi h_s^{\,3} (EI_{eff})_{cmp}} \qquad \text{(Equation 4.9)}$$

Table A.1. Sample calculation of PE debonding load using the proposed model

P	M_{cs}	I_{eff}	τ_{XY}	τ_{XZ}	σ_{XX}	I_1	I_2	I_3	σ_1	σ_2	σ_3	τ_{max}	Mohr-Coulomb τ_{max}	Mattock and Hawkins τ_{max}
10000	5500000	3.82×10^8	0.020	0.117	3.672	3.672	-0.014	0	0.004	0	-3.676	1.84	3.41	3.89
20000	11000000	1.13×10^8	0.132	0.785	3.672	3.672	-0.633	0	0.165	0	-3.837	2.00	3.41	3.89
30000	16500000	86348547	0.260	1.544	3.672	3.672	-2.452	0	0.577	0	-4.249	2.41	3.41	3.89
40000	22000000	79785035	0.374	2.228	3.672	3.672	-5.106	0	1.076	0	-4.748	2.91	3.41	3.89
49400	27181000	77535073	0.476	2.833	3.672	3.672	-8.253	0	1.573	0	-5.245	3.41	3.41	3.89
58250	32037500	76546369	0.568	3.382	3.672	3.672	-11.764	0	2.054	0	-5.726	3.89	3.41	3.89

All units N and mm

$$\tau_{XZ} = \frac{(EA)_{frp}\, h_{s,cmp} M_{cs}}{140(EI_{eff})_{cmp}\, h_s \ln(2t_s)} \qquad \text{(Equation 4.20)}$$

$$\sigma_{XX} = f_{ct} = 0.53\sqrt{f'_c} \qquad \text{[MPa]} \qquad \text{(Equation 4.21)}$$

Also for each applied load, using the calculated stresses the coefficients I_1, I_2 and I_3 are worked out using Equations 4.26, 4.27 and 4.28.

$$I_1 = \sigma_{XX} \qquad \text{(Equation 4.26)}$$

$$I_2 = -\tau_{XY}^2 - \tau_{XZ}^2 \qquad \text{(Equation 4.27)}$$

$$I_3 = \begin{vmatrix} \sigma_{XX} & \tau_{XY} & \tau_{XZ} \\ \tau_{XY} & 0 & 0 \\ \tau_{XZ} & 0 & 0 \end{vmatrix} = 0 \qquad \text{(Equation 4.28)}$$

Principal stresses σ_1, σ_2 and σ_3 are calculated as the roots of Equation 4.22, using the outcome of Equations 4.26 through 4.28 as coefficients. σ_2 will always be zero, while σ_1 will be a tensile stress (positive value) and σ_3 a compressive stress (negative value).

$$\sigma^3 - I_1\sigma^2 + I_2\sigma - I_3 = 0 \qquad \text{(Equation 4.22)}$$

The corresponding maximum shear stress can now be calculated using Equation 4.29. This is the maximum shear stress in the concrete adjacent to the adhesive layer near the strip end, resulting from the applied loads.

$$\tau_{\max} = \frac{|\sigma_1| + |\sigma_3|}{2} \qquad \text{(Equation 4.29)}$$

Finally, the value yielded by Equation 4.29 is compared with a failure criterion to determine the debonding load. The FRP strip will be predicted to fail by PE debonding at the load at which the maximum applied shear stress given by Equation 4.29 reaches the concrete shear strength from Equation 4.30 if the Mohr-Coulomb failure criterion is used, or the shear strength given by Equation 4.40 if Mattock and Hawkins' failure criterion is used.

$$\tau_{\max} = \frac{f'_c \, f_{ct}}{f'_c + f_{ct}} \qquad \text{(Equation 4.30)}$$

$$\tau_{\max} = 1.06 f_{ct} \qquad \text{(Equation 4.40)}$$

As shown in Table A.1, for Hassan and Rizkalla's specimen B1 the predicted debonding load is 49.40 kN when using the Mohr-Coulomb failure criterion, and 58.25 kN when using Mattock and Hawkins' failure criterion. These loads are compared to the experimental failure load of 53 kN presented in Table 2.2.